Memristive Effects in Ionic Nanopores

Author:
Thijs Rudolf ter Rele

Supervisor:
Prof. René van Roij

Daily Supervisor:
Willem Boon

Abstract

In the past 15 years much attention has been given to memristors, a type of passive electric circuit element that combines resistance with memory, characterised by a pinched hysteresis loop in the current-voltage diagram, when a periodic voltage is applied over the memristor. Ionic nanopores that connect aqueous electrolytes exhibit memristive behaviour and can be used as an actual realisation of a volatile memristor. In this thesis a general model for the conductivity and the hysteresis behaviour of memristors is developed from first principles. This model is applied to ionic nanopores, with consideration of the effect of changing the pore geometry and the frequency of the applied periodic voltage. To test the accuracy of the model, it is compared to finite-element calculations on cone-shaped and hourglass-shaped ionic nanopores. The analytic model is successful in predicting the number of crossings present in the hysteresis loops of pores with varying geometry, produced via finite-element calculations, and it revealed the role capacitive elements play in maintaining zero-crossing behaviour in memristors. We strongly encourage further experimental research into the memristive behaviour of nanopores.

Acknowledgements

I would like to thank my supervisor René van Roij, for suggesting this project to me in the first place and for the advice and suggestions he made during the master thesis project. His enthusiasm for the subject and for the results I generated, greatly encouraged my own enthusiasm for the project and ensured that it was a pleasure to work on it. I also want to give thanks to the members of the Soft-Matter theory group, for asking many questions that substantially helped the research progression. I would like to especially express my gratitude to Willem Boon for giving good advice and guiding the project into the right direction: without him this project would have looked very different. I would also like to thank Tim Kamsma for his help with setting up the COMSOL calculations and his advice on plotting results.

I am very thankful for the people in the study group, Casper, Franca, Iris, Justus, Lucas, Olaf and Salma, who helped me through the master program, motivated me to keep on working on my thesis and who offered some necessary distractions when getting coffee. Finally, I want to thank all the teachers, support staff and other students who helped me during the entire physics study program. You have made it a great joy to study physics and I am still glad that I switched to studying it five years ago.

Contents

1   Introduction

In this thesis we develop an analytic model to describe the hysteresis behaviour of volatile memristors. This model will be applied and tested on a nanofluidic nanopore system, as this system has uses for mimicking the behaviour of neurons. To perform this investigation it is necessary to discuss both memristive systems and nanofluidic transport.

1.1   Interest in Memristors

A *memristor* is a basic passive circuit element, first proposed in 1971 by Leon Chua and characterised by a relation between charge q and the magnetic flux ϕ. For this element he coined the name memristor, a portmanteau of the words *memory* and *resistor*, as it is an element whose resistance depends its past state: it has a memory component [1]. In 1976 Chua extended the concept of the memristor to a broader model of memristive systems [2]. These systems can be defined by a *pinched hysteresis loop* in the current-voltage-diagram: if a periodic voltage $V(t)$ is applied over the memristor, the resulting current-voltage Lissajous figure will be pinched in the origin.
The papers by Chua from 1971 [1] and 1976 [2] were largely mathematical and did not describe how to develop a physical memristor. In the next thirty years very little attention was given to memristor research [3]. However, systems with memristive hysteresis behaviour had been studied before and after Chua published his papers. Systems such as discharge tubes, studied in 1948 [4], and systems containing thin oxide films, as described in 1967 [5], can be analysed to show that they possess the *pinched hysteresis loop* hallmark of memristors and we can therefore, according to the definition given by Chua, denote these systems as memristors. Their pinched hysteresis behaviour, however, requires active circuit components and thus a power supply to maintain their particular resistance [6]. They are therefore examples of volatile memristors; a volatile memristor returns to a fixed memristance if power over the device is turned off [7]. This is different from a "genuine" memristor, which is a passive circuit element that does not require a power supply. Because a true, non-volatile memristor seemed unachievable, little research was performed on memristors and memristive behaviour; this applied to both volatile and non-volatile memristors.
This changed in 2008, when scientists at Hewlett-Packard published a paper in which they reported on a memristor with non-volatile memory [8]. The scientists claimed that they had developed a two-terminal memristor of less than 50 nm diameter from titanium dioxide [9]. The realisation of the first non-volatile memristor sparked the interest of both industry and academia into memristor-research, as memristors now appeared to be experimentally feasible. The research into memristors increased immensely as a result of the publication of this paper [3].

The interest and enthusiasm for memristors stems from their various promising applications. Most interest has gone to the use of memristors as memory storage devices. Memristors can be used as digital memory, as they can store at least one bit of information. For a non-volatile memristor this one-bit memory can be achieved by setting its resistance to either R_{on} or R_{off} using a current- or voltage-pulse, as the resistance of a memristor depends on the voltage applied over it in the past [3]. However, this one-bit memory is not all that different from what is currently used in memory devices. The promising part of the digital memory application lies in a storage method that is a potential replacement of flash memory, called resistive random access memory (ReRAM). Flash memory is a commonly used method for memory storage, which does not require a power supply to store data. The ReRAM method, which uses memristors, has the potential advantage of smaller reading and writing times over currently used memory systems [10]. Furthermore, the continuous resistance of a memristor leads to opportunities for the development of multistate memory cells [11].

Another interesting application of memristors lies in neuromorphic computing. Neuromorphic computing is the construction and use of computing systems that mimic the architecture present in the neural system, which has the promise of lower power consumption than standard computing systems. Memristors can play a part in constructing these systems [12].

In this thesis we will mostly consider volatile memristors, since the systems considered in this project are volatile. In the past most attention has been given to the possible applications of non-volatile memristors, as the non-volatility property is very useful for memory storage purposes. However, volatile memristor have applications in various other fields as well. These include hardware security applications and their use in devices to access digital memory [13]. Volatile memristors can also be used for neuromorphic computing, even though non-volatile memristors are more often considered for computing purposes. Memristive devices are being considered to act as energy- and space-efficient system representations for both synapses and neurons in neuromorphic systems [14]. They also have a purpose in so-called Complementary Metal-Oxide Semiconductor (CMOS) neural processing systems, in which the characteristic retention rate of certain volatile memristors is used [15]. Memristive and nanoionic devices have specifically been mentioned as candidates for the development of neuromorphic computing architectures [16].

Volatile memristors can also be used in modelling the action potential in a neuron, described through the *Hodgkin-Huxley model* [17], which is a mathematical model that gives a description of the signalling through neurons using an equivalent circuit [18]. The classical Hodgkin-Huxley circuit contains two time varying resistors, but the model is actually wrong in the sense that these should in fact be two memristors, that possess a time-invariant resistance [7]. These two memristors come in the form of a sodium-ion channel and a potassium-ion channel, that are distributed over the entire length of an axon of a neuron. These channels exhibit memristive properties, in that their current-voltage Lissajous figures are pinched [19]. In the past few years there has been research into nanofluidic systems, with the specific goal of reproducing the memristive effects present in the Hodgkin-Huxley model [20].

An important example of volatile memristive systems are the aforementioned sodium- and potassium-nanopores. The conductive properties of these sodium-ion and potassium-ion channels come from the transport of Na^+- and K^--ions through a pore of about 0.2 nm in radius [21]. In this thesis we will investigate the memristive properties of micro- and nanopore systems with a much larger radius of the order of 100 nm.

1.2   Nanofluidic Systems

The past few decades has shown an increase in interest in micro- and nanofluidic devices, where attention is given to the transport of fluid and its solutes [22, 23]. Micro- and nanofluidic systems differ from systems at the macroscale in that the flow in these systems is basically laminar and easy to manipulate. A microfluidic channel system is characterised by a channel dimension of 100 nm to 1 μm, whereas nanofluidic system in turn is characterised by channel features of less than 100 nm, through which or past which a fluid flows [24]. In nanofluidic systems the interactions between individual molecules and of individual molecules with surfaces become non-negligible, however, it is still possible to describe the main transport phenomena through these systems with theories based on continuum and mean-field approaches [23]. In fact, the results from this continuum approach are surprisingly similar to the results from molecular dynamic simulations, except for the few layers of molecules closest to the channel wall [25]. From molecular dynamics simulations we find that this continuum description of water starts to fail at a cross over length scale of $l_c \approx 1$ nm [26]. Below this dimension the notion of viscosity of water is no longer valid and *Navier-Stokes* (NS)

hydrodynamics therefore no longer as well [27, 28], but for most nanofluidic applications involving larger dimensions the NS approach can be safely used to study fluid mechanics.

An important feature of microfluidic and, even more so, nanofluidic systems is the high *surface-to-volume ratio* [28], which leads to the interactions between fluid and wall becoming important, resulting in various mechanical and electrochemical phenomena in classical fluids [23]. An example of a mechanical phenomenon is the effect of friction between wall and fluid, which is often expressed through the no slip condition, that entails that at the wall the fluid velocity is set at zero. Another feature of channel surfaces is that almost all materials carry some surface charge, leading to electrochemical interactions [23]. As a result, electrostatic forces repel co-ions carrying the same charge-type as the wall and attract counter-ions; these ions are almost always present in water.

In this thesis we will investigate the transport of solvent, salt and charge through micro- and nanofluidic channels, connecting two reservoirs each filled with a liquid electrolyte. These types of channels, which can be called micropores or nanopores, have many applications, such as DNA-translocation [29, 30], electro-osmotic fluid pumping [31, 32] and energy extraction in the form of osmotic-energy, extracted from the mixing of salt and fresh water [33–35]. These nanofluidic channels can also be used for desalinisation [36] and for nanofiltration purposes [37]. The devices that are used for these purposes can all be characterised as channels with charged walls, connecting two electrolyte reservoirs with different conditions.

Our main interest lies in the electric current in nanopores, caused by transport of charged particles, which has been observed to possess some interesting properties. Examples of these properties in conical nanopores are diodic behaviour [38, 39] and non-linear pressure dependence of the current [40, 41]. These current rectification effects are a result of salt accumulation and depletion in the channel.

An interesting feature related to the current rectifying behaviour of the pores, that has not been investigated extensively, are the memristive properties of ionic channels. These memristive properties can be observed by applying a periodic potential over the nanopore [42–44]. The memristive effects in these nanopores are of interest, because ion-channel memristors are essential for generating the action potential in neurons as described by the Hodgkin–Huxley model, which we mentioned before [7]. This research project will largely focus on memristive effects in ionic nanopores, where attention will be given to symmetric and asymmetric channel geometries with respect to exchanging the inlet and outlet. We will study how altering the geometry of a conical channel alters the memristive properties of the channel. We hope to develop a general analytic model for determining the type of memristor, taking into account the conductivity and capacitance of the channel.

In this project we perform our research using two main techniques. The first technique is developing a general analytic model for the hysteresis behaviour of memristors. Secondly, we study the memristive behaviour of ionic nanopores using numerical finite-element calculations of the Poisson-Nernst-Planck-Stokes equations, that describe diffusive, advective and Ohmic transport of water, co-ions and counter-ions. We then apply the general model on the nanopore system and inspect how well the finite-element results agree with the developed analytic model. We will give special attention to how changing the geometry, and more specifically the symmetry, of the channel changes its hysteresis loop behaviour, by inspecting the number of crossings it possesses and the area enclosed by the loop. Through comparison of the results from the two techniques we can test the analytic model.

2 Theory

In this section a theoretical basis is given for how memristive systems are described mathematically. We also introduce some important concepts and equations concerning nanofluidic transport phenomena.

2.1 Memristors

From classical circuit theory we know that there are three basic passive circuit elements: the resistor, the capacitor and the inductor. Each of them is associated with a certain relation between the variables charge, voltage, current and flux. The coupling by these elements occurs through the following differential relations

$$\text{Resistor: } dV = RdI \tag{2.1}$$
$$\text{Capacitor: } dq = CdV \tag{2.2}$$
$$\text{Inductor: } d\phi = LdI \tag{2.3}$$

with V, I, q and ϕ denoting voltage, current, charge and flux, respectively. The factors R, C and L denote the resistance, capacitance and inductance of their respective elements [3]. Besides these relations, current and charge, and voltage and flux are also related as follows

$$dq = Idt; \ d\phi = Vdt, \tag{2.4}$$

with current and voltage defined by time (t) derivatives of the charge and flux, respectively. These five relations couple all of the aforementioned variables to each other, except for one set of variables: charge q and flux ϕ. In 1971 Leon Chua used a symmetry argument to argue for the existence of a fourth basic circuit element, besides the three classically known elements. He called this element, which is characterised by a relation between charge q and magnetic flux ϕ, a memristor [1]. The differential relation of this element is

$$d\phi = Mdq, \tag{2.5}$$

with M the memristance of the memristor [3]. One can check that the dimensionality of M is equal to resistance R, so its unit is Ohm.

The properties of a memristor are exhibited, if one applies periodic potential difference $V(t)$ over the device. In general, a memristor behaves like a non-linear resistor if the frequency of the applied periodic voltage goes to zero, since the system has enough time to adjust to the applied potential difference. It behaves as a linear resistor in the limit that this frequency goes to infinity, as the system has too little time to adjust and has an approximately constant resistance [11].

At intermediate frequencies, however, we find that as a result of the non-linear memory effect, its current-voltage curve (IV-curve) is characterised by a pinched hysteresis loop with the pinch at the origin of the IV-plot [6]. In a 2013 review paper Chua even states "If it is pinched, it is a memristor", as a pinched loop in the current-voltage diagram, also called IV-curve, indicates that the studied element is a memristor [6]. In Fig. 1 we find some examples of such a pinched hysteresis loop. This loop can also cross itself at different points in the loop and still be a memristor, but only the pinch at the origin is indicative for a memristor.

Memristors can be classed in a broader group of physical systems or devices that resemble the memristor, but cannot be modelled as memristors. The memristor is only a specific case in a general class of dynamic systems, which are called memristive systems. Memristive systems, first

introduced as a concept by Chua in 1976, are defined by

$$\frac{\partial \boldsymbol{x}}{\partial t} = f(\boldsymbol{x}, u, t) \tag{2.6}$$

$$y = g(\boldsymbol{x}, u, t)u, \tag{2.7}$$

where u and y denote the input and output of the system, respectively, and the n-dimensional vector $\boldsymbol{x}$ denotes the state of the system [2]. The function $g(\boldsymbol{x}, u, t)$ is a generalised scalar response function and $f(\boldsymbol{x}, u, t)$ a continuous n-dimensional vector function [11]. An important characteristic of memristive systems can easily be identified from Eq. (2.7), namely that if the input u is zero, the corresponding output y is zero as well. This zero-crossing property can be seen in Lissajous figures of these systems, as the curves in these figures pass through the origin: they are pinched [2].

In this thesis we will mostly encounter voltage-controlled memristive systems, with a current as output. These are defined by the relation

$$\frac{\partial \boldsymbol{x}}{\partial t} = f(\boldsymbol{x}, V, t) \tag{2.8}$$

$$I(t) = G(\boldsymbol{x}, V, t)V(t), \tag{2.9}$$

with I and V the current and voltage across the system, respectively, and $G(\boldsymbol{x}, u, t)$ the memductance of the system, which stands for memory conductance, the inverse of the memristance [11]. If the memductance only depends on the flux over the memristor the system is called current-controlled *ideal memristor*. For this ideal memristor the relation in Eq. (2.9) reduces to

$$\frac{\partial \phi}{\partial t} = V(t) \tag{2.10}$$

$$I(t) = G[\phi]V(t), \tag{2.11}$$

with memductance $G(\phi) = \frac{dq(\phi)}{d\phi}$ [6]. In this case the current through the memristor is

$$I(t) = G\left[\int_{-\infty}^{t} dt' V(t')\right] V(t'). \tag{2.12}$$

For the sake of convenience we will refer systems described by Eq. (2.9) as a memristor in this thesis, whereas if we are dealing with an ideal memristor, defined by Eq. (2.11), we will explicitly refer to it as such.

2.2 Memristor Types and Symmetry

It is possible to differentiate between type-I memristors, also called self-crossing memristors, and type-II memristors, also called non-crossing memristors [11]. The hysteresis loop of a type-I memristor crosses at the pinch, whereas the hysteresis loops of a type-II memristor only touches itself at the pinch. We can also say that a type-I memristor exhibits a transversal hysteresis loop and and a type-II memristor a non-transversal hysteresis loop, since the type-I memristive loop crosses itself transversely [45]. The two types of IV-curves are illustrated in Fig. 1, from which we can see that the hysteresis loop of a type-I memristor crosses itself once, namely at the pinch, while the hysteresis loop of a type-II memristor does not cross itself.

The type of memristive behaviour is important if one wishes to use memristors for memory purposes. An example is constructing a learning algorithm with nanofluidic devices, similar to the way neurons work. In this system type-I behaviour is preferred above type-II behaviour, because its memory
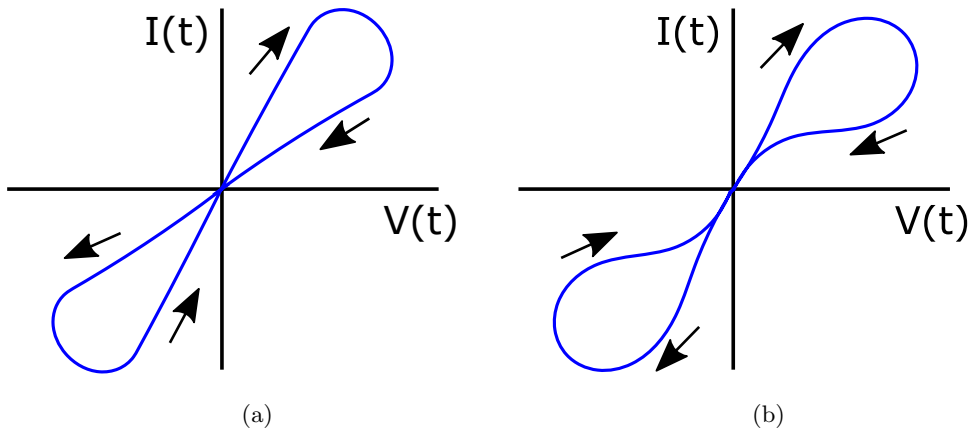
(a)   (b)

Figure 1: Schematic of current-voltage (IV) diagrams for (a) a type-I and (b) a type-II memristor, over which an AC-current is applied. The arrows indicate the path of the hysteresis loop.

is not lost as the applied voltage is set to zero, since it can have two distinct conductivities at a voltage $V(t) = 0$ [46].

In general the memristor-type is determined using the slope of hysteresis loop at the pinch. In the case of a memristor driven by a periodic voltage $V(t) = V_0 \sin\left(2\pi\frac{t}{T}\right)$ with T the period, this pinch occurs when the hysteresis loop meets itself at $V(t) = 0$. The hysteresis loop is indicative of a type-I memristor if the slope of the loop departing from the origin is different from the slope when returning to the origin, or

$$\left.\frac{dV}{dI}(t)\right|_{t=nT} \neq \left.\frac{dV}{dI}(t)\right|_{t=nT+T/2}, \tag{2.13}$$

with $n \in \mathbb{Z}$ an integer. At the times $t = nT$ and $t = nT + T/2$ the memristor passes through the origin. In the case of a type-II memristor the slope of the hysteresis loop departing from the origin is the same as returning to it, so

$$\left.\frac{dV}{dI}(t)\right|_{t=nT} = \left.\frac{dV}{dI}(t)\right|_{t=nT+T/2}. \tag{2.14}$$

Only the behaviour at the pinch determines the memristor type for this definition [45].

The type of memristor is determined to some capacity by the dependence on input u of the functions $f(\boldsymbol{x}, u, t)$ and $g(\boldsymbol{x}, u, t)$ of Eq. (2.6) and Eq. (2.7). Type-II memristive behaviour is often encountered when these are even functions of u. If the functions are non-even, we expect to encounter type-I memristive behaviour; odd functions are especially indicative of type-I crossing behaviour. There are however exceptions to this general rule in certain memristive systems [11]. From this rule we can however find that type-II memristive behaviour cannot occur in ideal memristive systems. In ideal memristive systems the functions f and g are restricted: function f must be equal to the input u, so $f(\boldsymbol{x}, u, t) = u$, and g can only depend on the state of the system $\boldsymbol{x}$, so $g(\boldsymbol{x}, u, t) = g(\boldsymbol{x})$. In this memristive system, the function $f(\boldsymbol{x}, u, t)$ clearly is an odd function of u, which results in odd-symmetric, type-I memristive behaviour [47].

This general rule can also be applied on the type of system studied in this thesis, that are described by Eq. (2.9). The memductance $G(\boldsymbol{x}, V, t)$ can be expressed in even and odd power of input $V(t)$

$$G(\boldsymbol{x}, V, t) = G_0(\boldsymbol{x}) + \sum_{i=1}^{\infty} \alpha_i(\boldsymbol{x})V(t)^{2i-1} + \sum_{j=1}^{\infty} \beta_j(\boldsymbol{x})V(t)^{2j}, \tag{2.15}$$

with G_0 the memductance at $V = 0$. In the case that the odd-powered α-terms dominate in $G(\boldsymbol{x}, V, t)$, we will most likely find type-I memristive behaviour, whereas if the even-powered β-terms dominate, we expect to encounter type-II behaviour.

From the geometry of a particular system it is possible to determine some memristive characteristics of that system. If a system is perfectly symmetric in the direction over which the potential difference V is applied, the odd terms in Eq. (2.15) must vanish, as the system cannot behave differently if the sign of the applied potential difference changes. Only the even-powered β-terms remain, which means that we expect to find type-II behaviour. If any asymmetry is introduced in the system, the odd terms reappear and type-I behaviour is again possible. System symmetry clearly is of importance in determining the memristor type.

Up until now we made the assumption that the hysteresis loop of a memristive system always crosses in the origin. However, as a result of different possible mechanisms, it can occur that the pinch of the hysteresis loop does not lie at the origin of the IV-plot anymore. This is called a non-zero crossing hysteresis loop [48]. This behaviour is often the result of a capacitive element present in the system [49, 50], which is illustrated in Fig. 2. Depending on the type of memristor and the type of capacitance, this can lead to non-pinched hysteresis loops, hysteresis loops with two crossings and hysteresis loops with the pinch at a point other than the origin [48]. In this thesis we will inspect the effect of capacitance on the hysteresis behaviour of a memristor. As this means that we will encounter non-zero crossing behaviour, we define the memristor type not by its slope at the origin, but rather by its crossing behaviour in a hysteresis loop: a type-I memristor has a single crossing and a type-II memristor has none. This is what we will mean when discussing these type-I and type-II memristors in this report.
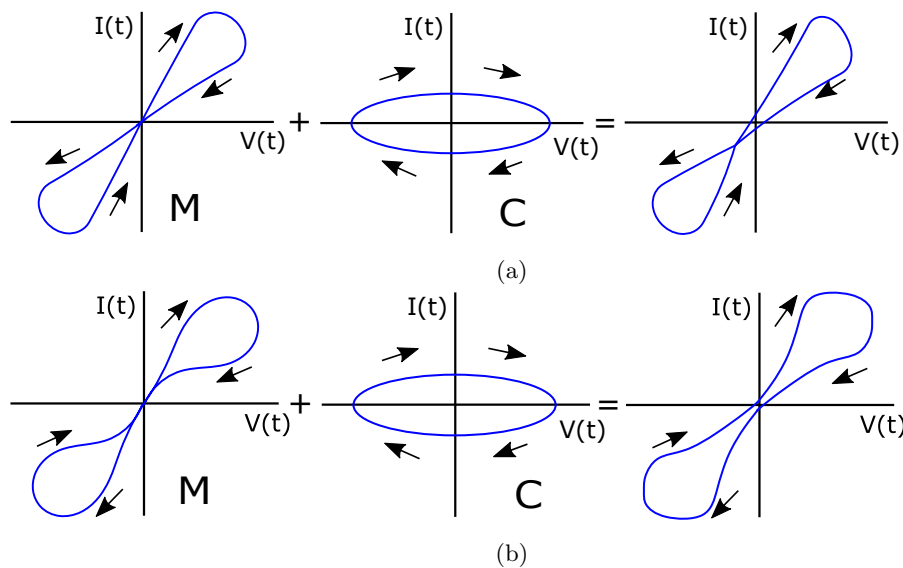

Figure 2: Schematic of current-voltage (IV) diagrams for (a) a type-I and (b) a type-II memristor (M), over which an AC-current is applied, added up with the current response of a capacitor (C). This creates non-zero crossing behaviour for (a) and no-crossing behaviour for (b).

2.3 Electrostatics and Ionic Fluids

This thesis is mostly concerned with the behaviour of an ionic nanochannel under a periodic, time-dependent potential difference. However, before we can start to study time-dependent phenomena of electrolytic systems, we first look at the equilibrium. In this subsection we will set up some of the theoretical framework required for studying electric charge transport through a channel, by describing how an *electric double layer* (EDL) is formed. An EDL forms when a charged solid surface is in contact with an electrolyte. Near this surface the electrolyte will have a net opposite charge.

In this subsection, we largely reproduce the derivations as found in chapter 11 of Ref. [51] and in chapter 8 of Ref. [52]. In these derivations we consider an aqueous 1:1 electrolyte, in contact with a planar surface with fixed charge density $e\sigma$, where e is the elementary charge. The surface is located at coordinate $z = 0$ and the electrolyte in the region $z > 0$. We assume the surface and the electrolyte to extend infinitely in the x- and y-directions, which means that the geometry in translationally invariant with respect to these two coordinates.

2.3.1 Electric Double Layer

The electric double layer can be described using the electric potential $\psi(z)$ and the distribution of the positive and negative ions $\rho_\pm(z)$ near the surface. The connection between the density and electric potential is given by Poisson's equation

$$\nabla^2 \psi(\mathbf{r}) = -\frac{Q(\mathbf{r})}{\epsilon_0 \epsilon_r}, \tag{2.16}$$

where ϵ_r is the relative permittivity of the medium and Q the electric charge density. For an ionic solution this density becomes $Q = e\,(\rho_+ - \rho_-)$. As the planar geometry is translationally invariant in the xy-plane, the Poisson equation reduces to

$$\frac{d^2\psi(z)}{dz^2} = -e\frac{\rho_+(z) - \rho_-(z)}{\epsilon_0 \epsilon_r}. \tag{2.17}$$

The second relation we have to take into account is the Boltzmann distribution, which relates the energy $\pm e\psi(z)$ of an ion with charge e in an electric potential $\psi(z)$ to the concentration of the ion species $\rho_\pm(z)$. In the planar geometry the Boltzmann distribution becomes

$$\rho_\pm(z) = \rho_b \exp\left[\mp \beta e \psi(z)\right], \tag{2.18}$$

with $\beta = \frac{1}{k_B T}$, where T is the temperature and k_B Boltzmann constant, and ρ_b the bulk ion concentration far from the surface at $z \to \infty$. Combining Eq. (2.17) and Eq. (2.18) gives

$$\frac{d^2\psi(z)}{dz^2} = -\frac{e\rho_b}{\epsilon_0 \epsilon_r}\left(\exp\left[-\beta e\psi(z)\right] - \exp\left[\beta e\psi(z)\right]\right) = \frac{2e\rho_b}{\epsilon_0 \epsilon_r}\sinh\left[\beta e\psi(z)\right]. \tag{2.19}$$

For convenience we introduce the dimensionless potential $\phi(z) = \beta e \psi(z)$, which simplifies Eq. (2.19) to $\frac{\partial^2 \phi(z)}{\partial z^2} = \kappa^2 \sinh\left[\phi(z)\right]$, where we have introduced the constant $\kappa^2 = \frac{2e^2 \beta \rho_b}{\epsilon_0 \epsilon_r}$.

To solve the differential equation, we can impose some boundary conditions. The first boundary condition concerns the potential at an infinite distance from the surface ($z \to \infty$), where the electric potential vanishes, so

$$\lim_{z \to \infty} \phi(z) = 0. \tag{2.20}$$

Another boundary condition confines the electric potential at the charged surface, which has an electric charge density of $e\sigma$. By imposing charge neutrality of the total system, we can find the potential at the surface. This charge neutrality combined with Eq. (2.17) gives

$$
\begin{aligned}
\sigma &= -\int_0^\infty dz \left(\rho_+(z) - \rho_-(z)\right) = \frac{\epsilon_0 \epsilon_r}{e} \int_0^\infty dz \frac{\partial^2 \psi(z)}{\partial z^2} \\
&= \frac{\epsilon_0 \epsilon_r}{e} \left(\frac{\partial \psi}{\partial z}(\infty) - \frac{\partial \psi}{\partial z}(0^+)\right) = -\frac{\epsilon_0 \epsilon_r}{e} \frac{\partial \psi}{\partial z}(0^+),
\end{aligned}
\tag{2.21}
$$

where $\frac{\partial \psi}{\partial z}(0^+)$ is the first derivative of the electric potential at $\lim_{z\downarrow 0}$. We have found the following three equations for the electric potential near a surface

$$
\frac{\partial^2 \phi(z)}{\partial z^2} = \kappa^2 \sinh\left[\phi(z)\right]
\tag{2.22}
$$

$$
\lim_{z\to\infty} \phi(z) = 0
\tag{2.23}
$$

$$
\frac{\partial \phi}{\partial z}(0^+) = -4\pi \lambda_B \sigma.
\tag{2.24}
$$

These equations contain the two length scales κ^{-1} and λ_B, which are the Debye length and the Bjerrum length, respectively. These two lengths are defined as

$$
\kappa^{-1} = \sqrt{\frac{2\rho_b e^2 \beta}{\epsilon_0 \epsilon_r}} \text{ and } \lambda_B = \frac{e^2 \beta}{4\pi \epsilon_0 \epsilon_r}.
\tag{2.25}
$$

The differential equation given in Eq. (2.22) together with the two corresponding boundary conditions can be solved analytically [53], which results in the following potential

$$
\phi(z) = 2\log\left[\frac{1 + \gamma e^{-\kappa z}}{1 - \gamma e^{-\kappa z}}\right],
\tag{2.26}
$$

where the constant γ can be found using the boundary condition Eq. (2.24). Solving it gives

$$
\gamma = \frac{\sqrt{1 + (a/2)^2} - 1}{a/2},
\tag{2.27}
$$

with the dimensionless surface charge $a = 4\pi \frac{\lambda_B \sigma}{\kappa}$. Using this expression for the electric potential and using Eq. (2.18), we can find the ion concentration as a function of distance from the charged surface

$$
\rho_\pm(z) = \rho_b \exp\left[\mp\phi(z)\right] = \rho_b \exp\left(\mp 2\log\left[\frac{1 + \gamma e^{-\kappa z}}{1 - \gamma e^{-\kappa z}}\right]\right) = \rho_b \left(\frac{1 \pm \gamma e^{-\kappa z}}{1 \mp \gamma e^{-\kappa z}}\right)^2.
\tag{2.28}
$$

This equation shows what the EDL entails: near the charged surface the concentration of the counter-ion is larger than the bulk concentration and the concentration of the co-ion is smaller. Moving away from the surface both concentration move towards bulk concentration, as the electric potential of the surface vanishes at large distance. This behaviour is illustrated in Fig. 3, in which ion concentrations $\rho_\pm(z)$ and the potential $\phi(z)$ are shown for distances z close to the charged surface. From these density-equations we can find the physical meaning of the Debye length $\kappa^{-1} = \lambda_D$, namely the characteristic thickness of the electric double layer.
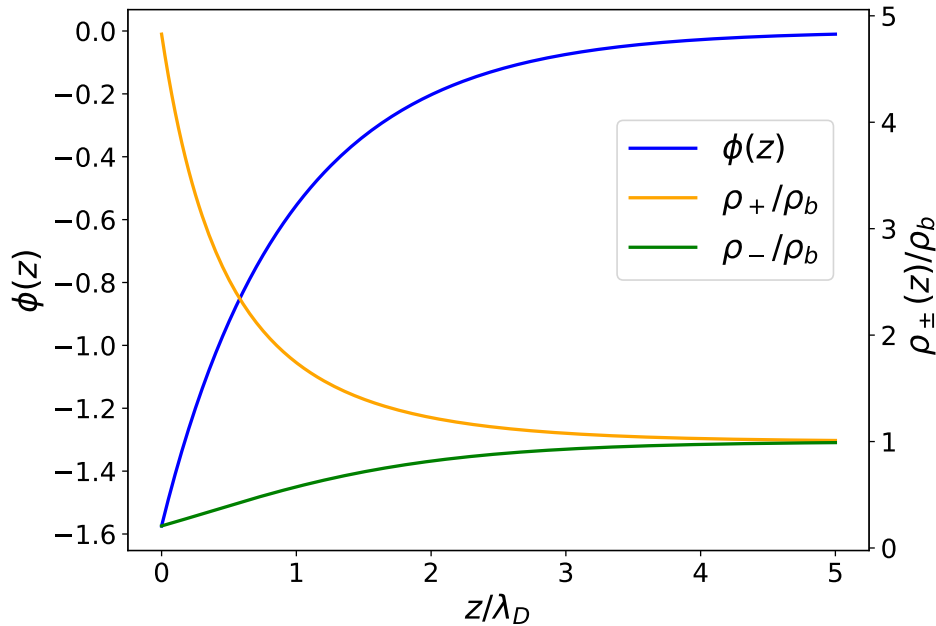
Figure 3: The electric double layer (EDL) of an infinitely large charged planar surface. The dimensionless potential ϕ and the concentrations of the positive and negative ions $\rho_{\pm}$ are plotted as a function of distance z from the charged surface.

2.3.2 Cylindrical Geometry

The pores studied in this thesis are cylindrically symmetric. We try to find an approximation for the electric potential in an infinitely long cylinder of radius R as a consequence of a charged surface. In the cylindrical geometry and the long channel limit, the Poisson-Boltzmann equation becomes

$$\frac{1}{r}\frac{\partial}{\partial r}\left(r\frac{\partial \phi(r)}{\partial r}\right) = \kappa^2 \sinh\left[\phi(r)\right], \tag{2.29}$$

where $r \in [0, R]$ is the distance from the cylinder's central axis. By symmetry the potential $\phi(r)$ does not depend on the polar angle θ and the lateral coordinate x.

This equation cannot be solved analytically, without making some assumptions. The weak field assumption, in which we assume that the potential $\phi(r) \ll 1$, is a natural step to take. Under this assumptions we can reduce the differential equation to

$$\frac{1}{r}\frac{\partial}{\partial r}\left(r\frac{\partial \phi(r)}{\partial r}\right) = \kappa^2 \phi(r). \tag{2.30}$$

This equation can be reduced to a modified Bessel differential equation of the first kind,

$$(\kappa r)^2 \frac{\partial^2 \phi}{\partial (\kappa r)^2} + \kappa r \frac{\partial \phi}{\partial (\kappa r)} - (\kappa r)^2 \phi = 0, \tag{2.31}$$

and has as the general solution

$$\phi(r) = c_1 I_0(\kappa r) + c_2 K_0(-\kappa r) \tag{2.32}$$

with the constants $c_1, c_2 \in \mathbb{R}$ and I_0 and K_0 the zeroth order modified Bessel functions of the first and second kind, respectively. To have the potential be finite at $r = 0$, we need the constant $c_2 = 0$, as $K_0(0)$ diverges. The other constant c_1 can be found using the boundary condition in Eq. (2.24), which indicates that at $r = R$, we need $\phi'(r) = 4\pi\lambda_B\sigma$. The derivative of the zeroth order Bessel function is the first order Bessel function, so we find that the solution of the potential is

$$\phi(r) = 4\pi\lambda_B\sigma \frac{I_0(\kappa r)}{\kappa I_1(\kappa R)}, \tag{2.33}$$

with $r \in [0, R]$. The potential above can be used to find the ion concentrations in the channel, which are given by

$$\rho_\pm(r) = \rho_b \exp\left[\mp\phi(r)\right] = \rho_b \exp\left[\mp 4\pi\lambda_B\sigma \frac{I_0(\kappa r)}{\kappa I_1(\kappa R)}\right]. \tag{2.34}$$

Under the assumptions made in this section the charge density and the salt concentration are given by

$$\rho_e(r) = 2\rho_b\sinh\left[-4\pi\lambda_B\sigma\frac{I_0(\kappa r)}{\kappa I_1(\kappa R)}\right]; \; \rho_s(r) = 2\rho_b\cosh\left[-4\pi\lambda_B\sigma\frac{I_0(\kappa r)}{\kappa I_1(\kappa R)}\right]. \tag{2.35}$$

A second assumption we can make is assuming that that the radius of the channel is so large, that we can approximate the channel wall to be a plane. We can make this approximation when the radius of the channel is much larger than the Debye length, so when $R \gg \kappa^{-1}$. By introducing the coordinate $s = R - r$ we can reduce the Laplacian derivative in cylindrical coordinates to

$$\nabla^2\phi(s) = \frac{1}{R-s}\frac{\partial}{\partial(R-s)}\left((R-s)\frac{\partial\phi(s)}{\partial(R-s)}\right) \approx \frac{\partial^2\phi(s)}{\partial s^2}, \tag{2.36}$$

as we are only interested in the region where $s \ll R$, because this is where the double layer is present. We can therefore reduce Poisson's equation, given in Eq. (2.29), to

$$\frac{\partial^2\phi(s)}{\partial s^2} = \kappa^2\sinh\left[\phi(s)\right], \tag{2.37}$$

which is identical to the planar Poisson equation in Eq. (2.22). The approximate solution for the electric potential in the channel is therefore given by

$$\phi(s) = 2\log\left[\frac{1 + \gamma e^{-\kappa s}}{1 - \gamma e^{-\kappa s}}\right], \tag{2.38}$$

and its corresponding ion concentration distribution by

$$\rho_\pm(s) = \rho_b\left(\frac{1 \pm \gamma e^{-\kappa s}}{1 \mp \gamma e^{-\kappa s}}\right)^2. \tag{2.39}$$

The constant γ is the same as in Eq. (2.27). In this thesis we will use the potential as given in Eq. (2.38), except if indicated otherwise.

2.4 PNPS Dynamics

In this project we study ionic nanochannel through finite-element calculations and analytic calculations with the equations that govern the dynamics of the systems. In the following section we will go through these equations. The dynamics present in the system at hand can be described by the *Poisson-Nernst-Planck equations* (PNP-equations) and the *Stokes equation*, which together can be abbreviated as the PNPS-equations.

Fluid flow is in general described by the Navier-Stokes equation. However, because the length scales of the system are in the order of micrometers, the Reynolds number $\text{Re} = \frac{\rho u L}{\eta}$ is small. The parameters ρ, u, L and η are the characteristic fluid mass density, velocity, length scale and dynamic viscosity of the system, respectively. For the nanopore we study we find $\text{Re} \approx 10^{-4}$, so $\text{Re} \ll 1$, which indicates that we can neglect the inertial forces in the system, as they are insignificant in system with small Reynolds number. The flow in the system is therefore described by Stokes' flow, which for an incompressible fluid is given by

$$\eta \nabla^2 \boldsymbol{u} - \nabla P - e\rho_e \nabla \psi = \rho \frac{\partial \boldsymbol{u}}{\partial t}, \tag{2.40}$$

$$\nabla \cdot \boldsymbol{u} = 0. \tag{2.41}$$

The forces applied on the fluid are the electric Coulomb force and the mechanical forces applied by the pressure gradients.

The fluxes of the charged ions in the electrolyte is described by the Nernst-Planck equation

$$\boldsymbol{j}_\pm = -D_\pm \left(\nabla \rho_\pm \pm \rho_\pm \frac{e\nabla \psi}{k_B T} \right) + \boldsymbol{u}\rho_\pm. \tag{2.42}$$

In this equation the concentration of the positive ions and negative ions in the 1:1 electrolyte are given by ρ_+ and ρ_-, respectively, and the corresponding fluxes of these ions by $\boldsymbol{j}_\pm$. The expression is composed of a Fickian diffusive term, an Ohmic conduction term and a Stokesian advective term, respectively. The electric potential ψ as a consequence of the charge density ρ_e is given by the Poisson equation

$$\nabla^2 \psi = -\frac{e}{\epsilon}\rho_e. \tag{2.43}$$

Finally, Eq. (2.44) represents the continuity equation, which accounts for the local conservation of the ions,

$$\nabla \cdot \boldsymbol{j}_\pm = -\frac{\partial \rho_\pm}{\partial t}. \tag{2.44}$$

These equations together are the PNPS-equations, that describe the dynamics in electrolyte systems, and we will apply these equations in our calculations to investigate the dynamics in nanopores. When a steady-state system is considered, the time derivatives in the PNPS-equations are set to zero.

Two important properties related to transport phenomena described by the PNPS-equations, are the salt concentration ρ_s and the ionic electric charge density ρ_e. These properties are written as

$$\rho_s = \rho_+ + \rho_-, \tag{2.45}$$

$$\rho_e = \rho_+ - \rho_-. \tag{2.46}$$

The salt concentration is the total ion concentration at a certain location and the ionic charge density is the negative ion concentration subtracted from the positive ion concentration. These properties will be used in the rest of this thesis.

2.5 Onsager Relations

The Poisson-Nernst-Planck and the Navier-Stokes equations can be applied to study the transport behaviour in a given geometry, under the influence of driving forces over this geometry. The relation between these driving forces and the transport phenomena are the Onsager reciprocal relations [54, 55]. The linear response of transport phenomena to a small applied driving force are described in these relations.

In this thesis we are interested in transport through nanochannels as a result of an applied voltage drop, which is the relevant driving force in our investigations. We are interested in the resulting transport of ions, electric charge and fluid through the channel; these are the salt, electric charge and fluid flux, respectively. In an axially symmetric system these fluxes are given by

$$J(x) = 2\pi \int_0^{R(x)} r\left(j_{+,x}(r,x) + j_{-,x}(r,x)\right) dr, \tag{2.47}$$

$$I(x) = 2\pi e \int_0^{R(x)} r\left(j_{+,x}(r,x) - j_{-,x}(r,x)\right) dr, \tag{2.48}$$

$$Q(x) = 2\pi \int_0^{R(x)} r u_x(r,x) dr, \tag{2.49}$$

where $j_{\pm,x}$ are the lateral components of the ion fluxes as given in Eq. (2.42) and $u_x(r,x)$ the lateral fluid velocity. The upper integral limit $R(x)$ is the radius of the channel at coordinate x.

2.5.1 Transport in a Cylinder

We derive the elements of the Onsager matrix for transport phenomena in a cylinder, as this is the simplest axially symmetric system and the elements are therefore the easiest to derive. We will largely follow the derivation of a 2020 paper by Werkhoven et al. [56]. In these derivations we consider a cylindrical pore in the long channel limit. This allows us to ignore entrance effect of the channel and assume that properties of the channel only depend on its radius. Charge density, salt concentration, and fluid velocity are thus given by $\rho_e(r)$, $\rho_s(r)$ and $\boldsymbol{u}(r)$.

To determine the fluid flux steady Q through a channel as a result of an applied potential, we first need the fluid velocity $\boldsymbol{u}(r)$ through the channel. As the only driving force we apply over the channel in the potential difference, Stokes equation in Eq. (2.40) reduces to

$$\eta \nabla^2 \boldsymbol{u} - e\rho_e \nabla \psi = 0, \tag{2.50}$$

from which we can derive the lateral velocity $u_x(r)$. In the long channel limit the field in the x-direction depends on the potential difference over the channel and is given by $-\partial_x \psi = \frac{V}{l} = E$, with l the total length of the channel and V the potential difference. The electric field is constant in the channel in this limit. Substituting the Poisson equation in Eq. (2.43) and only taking into account the x-component gives

$$\partial_r^2 u_x = \partial_r^2 \psi \frac{\epsilon}{\eta} E. \tag{2.51}$$

With the no-slip boundary condition $u_x(r = R) = 0$, this equation can easily be solved through integrating twice, which gives

$$u_x(r) = \frac{\epsilon}{\eta}\left(\psi(r) - \psi_0\right) E, \tag{2.52}$$

with $\psi_0 = \psi(R)$ the potential at the boundary of the cylinder at $r = R$. We can now find fluid flux Q by integrating over $u_x(r)$, which gives

$$Q = 2\pi \int_0^R dr r u_x(r) = E\pi \frac{\epsilon}{\eta} \int_0^R dr r \left(\psi(r) - \psi_0\right). \tag{2.53}$$

We again use the dimensionless electric potential $\phi(z) = \beta e \psi(z)$, which we substitute in to find

$$Q = \frac{e}{4\lambda_B \eta} E \int_0^R dr\, r\, (\phi(r) - \phi_0) = \frac{e}{4\lambda_B \eta} E \pi \int_0^R ds\, (R - s)\, (\phi(s) - \phi_0)$$

$$\approx \frac{e}{4\lambda_B \eta} E \pi \left(-\phi_0 R^2 + R \int_0^R ds \phi(s) \right), \qquad (2.54)$$

where we implemented the coordinate $s = R - r$ and assumed that $R \gg \kappa^{-1}$. As the potential is only non-zero near the cylinder wall in the EDL and because we assume that $R \gg \kappa^{-1}$, we can assume that $\int_0^R \phi(s)ds \approx \int_0^\infty \phi(s)ds$. The expression for the the electric potential in a cylinder is given in Eq. (2.38) for as a function of s. We can numerically integrate this expression and find

$$\frac{1}{\lambda_D} \int_0^\infty ds \phi(s) \equiv P_1. \qquad (2.55)$$

In terms of this dimensionless number the electro-osmotic fluid flux in a cylinder, caused by a potential drop V, is given by

$$Q_{EO} = -\pi \frac{e}{4\lambda_B \eta} R^2 E \left(\phi_0 - \frac{\lambda_D}{R} P_1 \right) = -\pi \frac{e}{4\lambda_B \eta} R^2 E \left(\phi_0 + \mathcal{O} \left[\frac{\lambda_D}{R} \right] \right). \qquad (2.56)$$

In Appendix A an expression for the electric charge flux response I is derived, using the same techniques as were applied above.

3   Memristor Model and Model System

In this section the general analytic model for memristors applied in this thesis is introduced, which we do by stating the equations that govern the memristive system's behaviour and showing its equivalent circuit. Following this, we introduce the ionic nanopore system, on which the memristor model is applied. Afterwards, we explain how we perform finite-element calculations on ionic nanopore systems.

3.1   General Memristive Model

The type of memristor considered in this thesis is voltage dominated, which means that a voltage is applied over the memristor as input, resulting in a current as output. The relation between current I and applied voltage V, which has already been given in Eq. (2.9), is the following

$$I(t) = g(t)V(t),$$

with $g(t)$ the memductance of the system. A characteristic of a memristive system is that its memductance depends on the input applied over it in the past, which is the potential difference V. We assume that when a static potential difference is applied over the memristor for a very long time, the memductance will revert to the steady-state conductance $g_\infty [V(t)]$ for this voltage. This steady-state conductance depends on the specific situation in the memristive system being considered.

We propose the use of an Ansatz to predict how the memductance responds to a changes in potential difference. We assume that the derivative of the memductance depends linearly on the difference between the steady state conductance $g_\infty[V]$ and the memductance of the memristor at that moment. This Ansatz can be written as

$$\tau \frac{\partial g(t)}{\partial t} = g_\infty [V(t)] - g(t). \tag{3.1}$$

The constant τ in this equation is some characteristic timescale of the memristor, that determines how fast the memductance responds to changing voltages. This Ansatz ensures that the memductance will revert to the steady-state conductance $g_\infty [V(t)]$ if the potential difference is held constant for a long time. The conductance of the system always strives towards $g_\infty[V]$.

Solving the differential equation in Eq. (3.1) we find the following solution

$$g(t) = e^{-\frac{t}{\tau}} \left(\int_0^t d\theta g_\infty [V(\theta)] e^{\frac{\theta}{\tau}} + A \right), \tag{3.2}$$

with A a constant of integration, which can be determined using the fact that in the case of a steady state potential difference the conductivity must be constant. This allows us to extract A from the expression above.

The steady-state conductance depends on the potential difference applied over the memristor. We can expand this steady-state conductance in terms of even powers and odd powers of V,

$$g_\infty(V) = g_0 \left(1 + \sum_{i=1}^{\infty} \alpha_i V^{2i-1} + \sum_{j=1}^{\infty} \beta_j V^{2j} \right), \tag{3.3}$$

with g_0 the conductance if no potential difference is applied. To find memductance $g(t)$ we can insert g_∞ into Eq. (3.2) and solve the integral, either analytically or numerically.

It is possible to relate the expansion in Eq. (3.3) to the similar expansion in Eq. (2.15). In section 2.2 we discussed how this expansion can influence the hysteresis behaviour. As in section 2.2 we

predict that when the odd-powered α-terms dominate in $g_\infty[V(\theta)]$, we will most likely find type-I memristive behaviour, and if the even β-terms dominate we expect to encounter type-II behaviour. The symmetry arguments made in section 2.2 are also valid for the memristor described in this section.

When a potential is applied over a memristor, it can exhibit capacitive behaviour besides memristive behaviour, which is something many memristive system do [48]. This capacitive behaviour has an influence on the current measured over the memristive system. To include this capacitive element in the analytic model, we introduce a capacitor to the system, whose current contribution is given by

$$I_C(t) = C\frac{\partial V_C(t)}{\partial t}, \tag{3.4}$$

with C its capacitance and V_C the potential difference applied over the capacitor. We place this capacitor parallel to the memristor, which results in the circuit as given in Fig. 4.
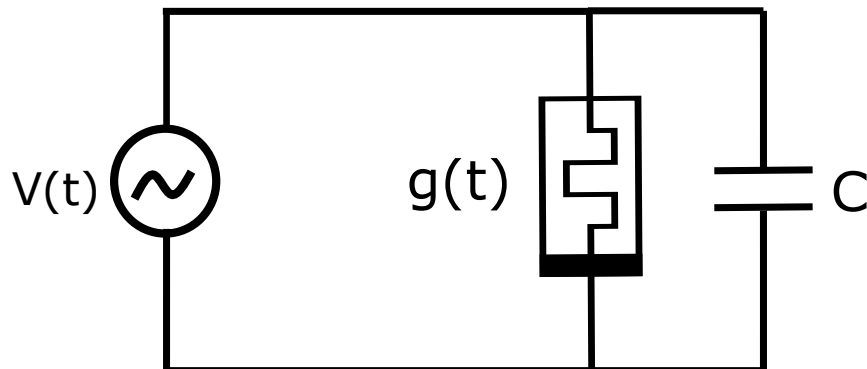

Figure 4: The circuit diagram of a memristor with memductance $g(t)$ and a capacitive element under a time-dependent potential difference $V(t)$. A capacitive element is included in the model by putting a capacitor with capacitance C parallel to the memristor.

In the circuit in Fig. 4 the potential difference over the memristor is the same as the potential difference over the capacitor, namely $V(t)$. Hence, the total current through the system, consisting of a memristive element and a capacitive element, is given by

$$I(t) = g(t)V(t) + C\frac{\partial V(t)}{\partial t}, \tag{3.5}$$

which we found using Kirchhoff's current law. The total current $I(t)$ over the memristive system is the memristive current and the capacitive current added up.

In Appendix B a different type of circuit is analysed, which contains an extra resistor in series with the capacitor. We defend the use of capacitive model as given in Fig. 4 in this appendix, based on the low RC-times we encounter in the systems studied in this thesis.

The model described in this section is very similar to the model used to describe memristors in Ref. [49]. The authors of Ref. [49] applied their model to describe the memristive behaviour of plant tissue. In this article they considered only the first three terms in the expansion given in Eq. (3.3) separately.

3.2   Model Ionic Channel

The model described in the previous section will be applied to ionic nanochannels in this thesis, as this is a system which has memristive properties. Its conductive properties come from charged ions moving through the pore, under the influence of an applied potential difference.

The geometry of the pores we study in this project is indicated in Fig. 5. It consists of two reservoirs filled with an aqueous electrolyte, connected to each other through a channel. The electrolyte in the device is a 1:1 electrolyte, so the bulk ion concentrations are $\rho_+ = \rho_- = \rho_b$. The diffusion constant of the positive and negative ions are $D_+ = D_- = D$. The electrolyte has viscosity η, mass density ρ and relative permittivity ϵ_r. As can be seen in Fig. 5, the two reservoirs are connected to each other by a channel with a charged wall. The radius of the channel is given by:

$$R(x) = \begin{cases} R_1(x) = R_t - \frac{x}{L_1}\left(R_b - R_t\right) & \text{for } -L_1 \leq x \leq 0 \\ R_2(x) = R_t + \frac{x}{L_2}\left(R_b - R_t\right) & \text{for } 0 \leq x \leq L_2. \end{cases} \tag{3.6}$$
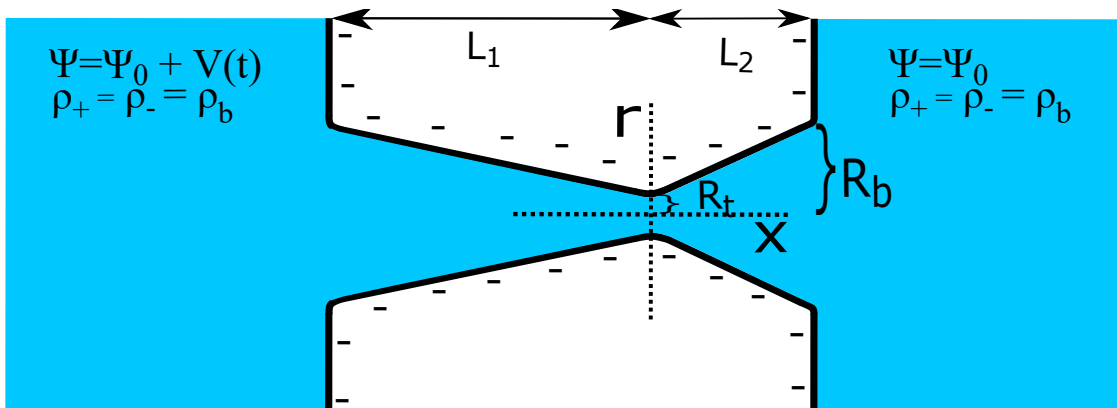

Figure 5: Schematic of the azimuthally symmetric channel of interest of this thesis. This channel consists of two coaxial cones with identical base radius R_b and tip radius $R_t < R_b$. The two cones have two different lengths L_1 (at $x < 0$) and L_2 (at $x > 0$), where x is the Cartesian axial coordinate such that at $x = 0$ the tips of the two cones connect. The distance to the negatively charged channel walls from the central axis is denoted by radial coordinate r. The channel connects two bulk reservoirs, filled with an aqueous 1:1 electrolyte with identical ion concentrations, identical pressure, but with time-dependent potential difference $V(t)$.

We define the difference between the radius at the opening and the radius at the center of the channel as $\Delta R = R_b - R_t$. The lengths L_1 and L_2 are defined such that the total channel length is constant at $2L$, which gives that $L_1 + L_2 = 2L$. The individual lengths L_1 and L_2 are defined in terms of the ratio δ as

$$L_1 = (1 + \delta)L \text{ and } L_2 = (1 - \delta)L, \tag{3.7}$$

where the range of the ratio is $\delta \in [0, 1]$. By varying L_1 and L_2 through δ we can change the geometry of the channel. If $L_1 = L_2$, so if $\delta = 0$, the channel is a symmetric hourglass channel, but for any non-zero value of δ the channel is no longer symmetric, as in this case $L_1 > L_2$. If $\delta = 1$, the two lengths are $L_1 = 2L$ and $L_2 = 0$, which means that the channel is purely conical. By changing the ratio δ we can control the geometry of the channel and its symmetricity.

We implement some boundary conditions on this channel. In the reservoirs at large distance from the channel, the pressure is P_0, the salt concentration is $\rho_s = 2\rho_b$ and the electric charge density is $\rho_e = 0$. At large distance from the channel in the reservoir at $x < 0$ the electric potential is $\Psi_0 + V(t)$, while it is Ψ_0 in the reservoir at $x > 0$. We apply no-slip and blocking boundary conditions on the walls. At the walls we thus find that the fluid velocity is zero, so $\boldsymbol{u} = 0$, and that the ion transport normal to the wall vanishes, so $\boldsymbol{n} \cdot \boldsymbol{j}_\pm = 0$, where $\boldsymbol{n}$ is the vector normal to the wall.

The channel surface has a charge density of $e\sigma$, which causes a potential ψ_0 to form at the wall. Gauss's law also applies at the wall, so $\boldsymbol{n} \cdot \nabla\psi = e\sigma/\epsilon$ holds. This potential leads to changes in the particle concentration $\rho_\pm(x, r, t)$ and can also cause a fluid velocity $\boldsymbol{u}(x, r, t)$ and ionic fluxes $\boldsymbol{j}_\pm(x, r, t)$ to form.

3.3 Finite-Element Calculations

We study the conductive and memristive properties of the ionic nanochannels by performing *finite-element calculations* (FE-calculations). Through FE-calculations with appropriate boundary conditions, we can solve the PNPS-equations numerically for a given geometry. These FE-calculations include steady state calculations, with a constant potential difference applied over the channel, and time-dependent calculations, with the applied voltage periodically varying in time.

The FE-calculations are performed using the software program COMSOL MULTIPHYSICS. This program allows one to construct the geometry of a system, which is then divided up into a mesh of individual cells. Each of these cells possesses a distinct set of the relevant values, describing the state of this cell. The geometries used in this thesis are 3D-axially symmetric channels, which allows us to treat the channel as a quasi-2D geometry in the FE-calculations, as the result will not depend on the angular θ coordinate. Examples of these 3D-axially symmetric grids for the channel, as described in Fig. 5, are shown in Appendix C.

In this thesis we will study the channel for a fixed set of standard parameters. These parameters are used in the FE-calculations and in calculations with an analytic model. The parameters, which represent water at room temperature, are given in Tab. 1.

ρ	998.2 kg/m^3
η	10^{-3} Pa $\cdot$ s
T	293.15 K
ρ_b	1 mol/m^3
$e\sigma$	-3.2044 mC/m^2
ϵ_r	80.2
R_b	450 nm
R_t	100 nm
$2L$	10 μm
D	10^{-9} m^2/s

Table 1: The parameters used in the finite-element calculations and analytical calculations in this thesis, representative of an aqueous 1:1 electrolyte at room temperature.

The bulk concentration of both the positive and negative ions is set at $\rho_b = 1.0$ mM, so the bulk salt concentration is $\rho_s = 2.0$ mM. The bulk conditions are achieved by setting the ion concentrations $\rho_\pm$ at the far boundaries of the reservoirs equal to ρ_b. The surface charge $e\sigma = -0.0032044$ C/m^2 is equivalent to two elementary charges per 100 nm^2. The diffusion coefficient D of both the co-ions and counter-ions is set to $D = 10^{-9}$ m^2/s.

The current I through the channel is the most important information found through the FE-calculations. It is extracted from the FE-calculations by measuring the total charge flux at the narrowest part of the channel. We integrate over the channel slice at $x = 0$ to find the total positive and negative ion-flux, and we find the total charge flux by subtracting these from each other. We can in turn find the current by multiplying this total charge flux by the elementary charge e. We can, however, also find the total fluid flux Q by integrating the fluid velocity u_x over the same channel slice. We have found that I and Q largely stay the same, as we change the x-coordinate where we integrate over the fluxes, such that they do not depend on the x-coordinate.

4   Model System: Ionic Channel

In this section we analyse the ionic channel, which we use as a realisation of a memristive system. The expressions for the salt concentration, charge density, electric current and capacitance in the channel are derived. An estimate for the characteristic timescale at which the channel responds to voltage changes is also made.

From Eq. (2.42) we can find expressions for the electric and salt flux. These are, respectively,

$$\boldsymbol{j}_e = \boldsymbol{j}_+ - \boldsymbol{j}_- = -D\left(\nabla\rho_e + \rho_s\frac{e\nabla\psi}{k_BT}\right) + \boldsymbol{u}\rho_e, \tag{4.1}$$

$$\boldsymbol{j}_s = \boldsymbol{j}_+ + \boldsymbol{j}_- = -D\left(\nabla\rho_s + \rho_e\frac{e\nabla\psi}{k_BT}\right) + \boldsymbol{u}\rho_s, \tag{4.2}$$

where we assume that $D_+ = D_- = D$. The three terms in these equations describe the diffusive, conductive and advective flux, in that order. Similarly we can find a continuity equation for these fluxes from Eq. (2.44), which gives

$$\nabla \cdot \boldsymbol{j}_e = -\frac{\partial\rho_e}{\partial t}, \tag{4.3}$$

$$\nabla \cdot \boldsymbol{j}_s = -\frac{\partial\rho_s}{\partial t}. \tag{4.4}$$

The total lateral current and lateral salt flux in the channel can be found by integrating the lateral components of the fluxes in Eq. (4.1) and Eq. (4.2) over the cross section of the channel, so $I(x,t) = 2\pi e \int_0^{R(x)} j_{e,x}(x,r,t)rdr$ and $J(x,t) = 2\pi \int_0^{R(x)} j_{s,x}(x,r,t)rdr$.

4.1   Steady State Salt Concentration

To get insight in how a potential drop over the channel affects the salt concentration in the channel, we first inspect the total lateral salt flux J in the channel. The derivations in this subsection are largely based on the derivations from a preprint by Boon et al. [41].

In deriving an expression for the total flux J we consider the channel to be in the long channel limit, so we assume the length of the channel is much larger than its radius, which means $L \gg R_b$. We can therefore neglect the entrance effects that can have an influence on J. In this limit the lateral components of the fluxes and gradients are much larger than their radial components, which we from here on out neglect. This allows us to work with a radially averaged salt concentration $c_R(x)$, as in this limit $\rho_x(r,x) \approx c_R(x)$, for all values of r outside the EDL. We also assume that the electric field does not depend on the radial coordinate r, so $\partial_x\psi(x,r) \approx \partial_x\psi(x)$.

A second assumption we make in this derivation is that the EDL is much thinner than the radius of the channel, so $\lambda_D \ll R_t$. This indicates that the charge density is negligible outside the EDL, which allows us to assume $\rho_e(r \ll R_t - \lambda_D) \approx 0$. Hence, the charge density ρ_e outside the EDL has minimal effect on the salt flux. The assumption $\lambda_D \ll R_t$ also allows us to ignore the effect of wall-curvature on the EDL, which means that we can apply the EDL-expressions of a flat-plate in our derivations, as given in Eq. (2.38) and Eq. (2.39).

Under these assumptions, the total salt flux becomes

$$J(x) = 2\pi \int_0^{R(x)} j_{s,x}(x,r)rdr = 2\pi \int_0^{R(x)} \left[-D\left(\partial_x c_R(x) + \rho_e\frac{e\partial_x\psi(x)}{k_BT}\right) + u_x c_R(x)\right] rdr$$

$$= -D\left(\pi R^2(x)\partial_x c_R(x) - 2\pi R(x)\sigma\frac{e\partial_x\psi(x)}{k_BT}\right) + Q c_R(x), \tag{4.5}$$

where Q is the total volume flux, defined as

$$Q(x) = 2\pi \int_0^{R(x)} u_x(r)rdr. \tag{4.6}$$

By assuming that the only space charge contribution in the channel comes from the EDL and that the total charge is conserved in the system, we can use

$$2\pi R(x)\sigma = -\int_0^{R(x)} \rho_e(r)rdr, \tag{4.7}$$

which allows us to insert the surface charge density σ in the expression for the salt flux.

Equation (4.4) shows that the salt current is divergence free in the steady state solution, hence we impose $\partial_x J = 0$, using Eq. (4.5) for $J(x)$. In the long channel limit, this results in the following differential equation:

$$\partial_x J = D\partial_x \left(\pi R^2(x)\partial_x c_R - 2\pi R(x)\sigma \frac{e\partial_x\psi}{k_B T} \right) - Q\partial_x c_R = 0. \tag{4.8}$$

By solving this equation we can find an expression for the steady state salt concentration $c_R(x)$. However, it is still necessary to obtain expressions for $\partial_x\psi$ and Q to find c_R.

The electric field $\partial_x\psi$ in the channel can be determined using Gauss's law and by neglecting any space charge outside of the EDL. We assume that the total system is charge neutral and the only significant charge contribution in the fluid lies in the EDL. The total charge within a slice of the channel and channel wall must therefore be zero, so the divergence of the electric field is zero $\nabla \cdot \nabla\psi = 0$. The electric field cannot penetrate through the channel wall, hence we find that $\pi R^2(x)\partial_x\psi = constant$, as we ignore the radial field components. The electric field must increase as the channel radius decreases and is given by

$$\partial_x\psi = \frac{constant}{\pi R^2(x)}.$$

We apply a total potential drop of V over the channel, so if we integrate $\partial_x\psi$ laterally we must find

$$V = -\int_{-L_1}^{L_2} \partial_x\psi dx = -\int_{-L_1}^{L_2} \frac{constant}{\pi R^2(x)} dx. \tag{4.9}$$

Solving this integral allows us to specify the *constant*, which leads to an expression for the electric field,

$$\partial_x\psi = -\frac{V}{2L} \frac{R_b R_t}{R^2(x)}. \tag{4.10}$$

In Fig. 6 the electric field from finite-element calculations and from Eq. (4.10) are compared. The channel being considered in Fig. 6 has the dimensions and the system parameters as given in Tab. 1. As these results closely match, we are confident that we can use Eq. (4.10) in combination with Eq. (4.5) for $J(x)$ to determine the salt concentration $c_R(x)$ in the channel.

The volume flux Q is completely electro-osmotic, as there is no pressure difference or chemical potential difference over the channel. We do not have an exact expression for the electric-osmotic flow over an hourglass channel or a conical channel. However, we do have an expression for the
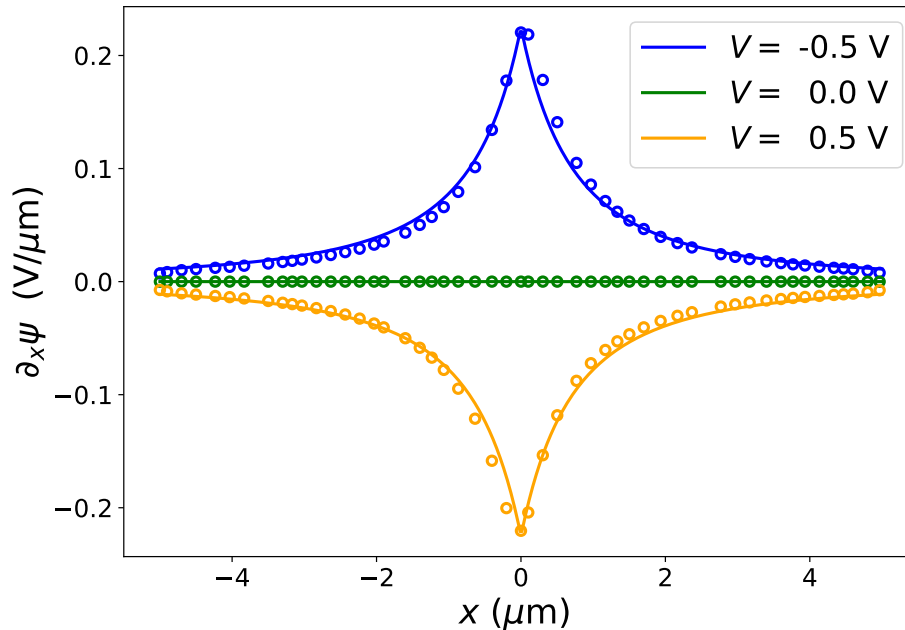
Figure 6: Electric field $\partial_x \psi$ at the centre line of a channel with $\delta = 0.0$, at radius $r = 0$. The results from the theory of Eq. (4.10) are denoted by the lines, the results from finite-element calculations are denoted by the circles.

electro-osmotic flow Q_{eo} through a cylindrical channel, which we found in Eq. (2.56). If we use this expression in the limit $\lambda_D \ll R$ the fluid flux through the channel reduces to

$$Q_{eo} = \frac{e\psi_0}{\eta} \pi R^2(x) \partial_x \psi = -\frac{V}{2L} \pi R_t R_b \frac{e\psi_0}{\eta}. \tag{4.11}$$

We inserted the electric field $\partial_x \psi$ from Eq. (4.10) into this expression, which cancels out the $R(x)$ dependence. We have found an approximate expression for Q, which does not depend on coordinate x, which is to be expected for the transport of an incompressible fluid through a nanopore.

To determine if this expression accurately predicts the fluid flux through a channel as described in Fig. 5, we compare its results to the results from finite-element calculations.

The channel being considered has the dimensions and system parameters as given in Tab. 1. The flux in the finite-element calculations and from the theoretical model follow the same general trend, as can be seen in Fig. 7, but the flux-values are not identical. At a voltage of $V = 1.0$ V the difference between the theoretical result and the FE-result is 13 %. At a voltage of $V = 0.1$ V this difference is 37 %. At negative voltages, the difference between theory and FE-calculations is a bit larger for the channel with $\delta = 0.95$; at $V = -1.0$ V the difference is 20 %.

There is some difference between the theory and the finite-element calculations for fluid flux, but it is not so substantial that we cannot use the expression for Q_{eo} for our analytic model. We will use it in our calculations from now on.

With Eq. (4.10) and Eq. (4.11) we have determined all unknowns of Eq. (4.8), which results in the following differential equation:

$$D\partial_x \left(\pi R^2(x) \partial_x c_R(x) + \pi \sigma \frac{eV}{Lk_B T} \frac{R_b R_t}{R(x)} \right) - Q_{eo} \partial_x c_R(x) = 0. \tag{4.12}$$
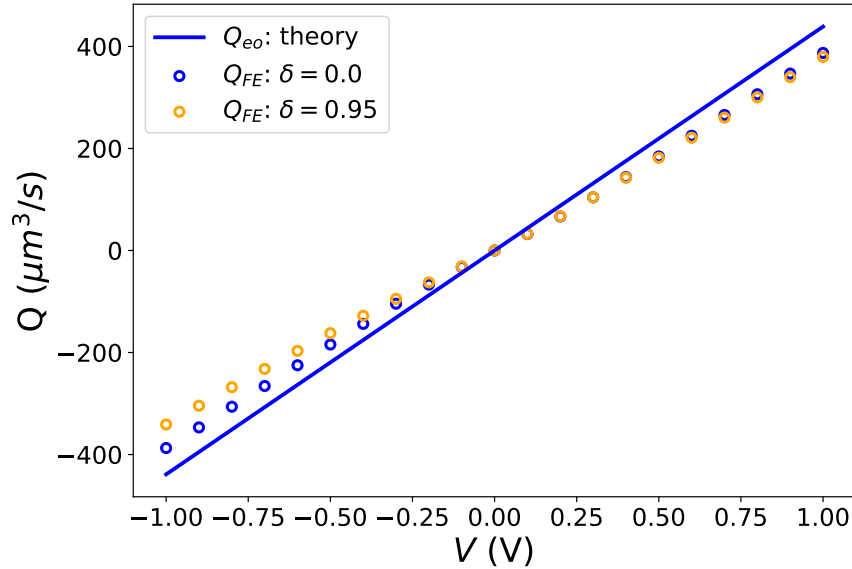
Figure 7: Fluid flow Q through a channel as a result of applying a static potential difference V. Finite-element calculations of channels with different δ are compared with a theoretical approximation, as given in Eq. (4.11).

We solve this equation to find the radially averaged salt concentration in the channel for a given channel geometry. To specify this pore the geometry studied in this thesis, we insert $R(x)$ from Eq. (3.6). To solve the differential equation for the geometry described by radius $R(x)$, we need to implement a boundary condition on the concentration c_R, which is

$$c_R\left(-L_1\right) = c_R\left(L_2\right) = 2\rho_b, \tag{4.13}$$

such that the salt concentration reverts to bulk concentration at the entrances to the channel. This boundary condition allows us to solve the differential equation, which gives

$$c_{R,\infty}(x) = \begin{cases} 2\rho_b + \frac{\Delta\rho}{\text{Pe}}\left[\left(1+\frac{x}{L_1}\right)\frac{R_t}{R(x)} + \frac{1}{\text{Pe}}\frac{4L^2}{L_1L_2}\frac{R_b}{R_t}\frac{1}{1-\exp\left[\text{Pe}\frac{R_t}{R_b}\right]}\left(1-\exp\left[\text{Pe}\frac{R_t}{R_b}\frac{L_2}{L_1+L_2}\right]\right.\right. \\ \qquad\left.\left. - \exp\left[\text{Pe}\left(1+\frac{x}{L_1}\right)\left(\frac{L_1}{L_1+L_2}\frac{R_t^2}{R_bR(x)}\right)\right] + \exp\left[\text{Pe}\frac{R_t(L_1R_t(1+x/L_1)+L_2R(x))}{(L_1+L_2)R_bR(x)}\right]\right)\right] \qquad \text{for } -L_1 \le x \le 0 \\[2em] 2\rho_b + \frac{\Delta\rho}{\text{Pe}}\left[\left(1-\frac{x}{L_2}\right)\frac{R_t}{R(x)} - \frac{1}{\text{Pe}}\frac{4L^2}{L_1L_2}\frac{R_b}{R_t}\frac{1}{1-\exp\left[-\text{Pe}\frac{R_t}{R_b}\right]}\left(1-\exp\left[-\text{Pe}\frac{R_t}{R_b}\frac{L_1}{L_1+L_2}\right]\right.\right. \\ \qquad\left.\left. - \exp\left[-\text{Pe}\left(1-\frac{x}{L_2}\right)\left(\frac{L_2}{L_1+L_2}\frac{R_t^2}{R_bR(x)}\right)\right] + \exp\left[-\text{Pe}\frac{R_t(L_2R_t(1-x/L_2)+L_1R(x))}{(L_1+L_2)R_bR(x)}\right]\right)\right] \qquad \text{for } 0 \le x \le L_2, \end{cases}$$
$$\tag{4.14}$$

where we used subscripts R and ∞ to indicate that this is the radially averaged, steady state concentration. Included in this expression are the Péclet number at the narrowest part of the channel

$$\text{Pe} = \frac{2LQ\,[V]}{\pi DR_t^2}, \tag{4.15}$$

which indicates the ratio of the advective transport rate, divided by the diffusive transport rate.

Also included is a measure for the concentration inhomogeneity in the channel

$$\Delta\rho = \frac{2\sigma\Delta R}{R_t^2}\frac{eV}{k_BT},\tag{4.16}$$

which shows that if $\Delta R = 0$ there will be no lateral salt concentration gradient in the channel.

Equation (4.14) is quite involved, but it is consistent with results for similar channels. When we take the limit $L_1 \gg L_2$, in which one cone in the channel is much longer than the other, the concentration c_L reduces to the expression Boon et al. [41] found for a conical channel. If we take $L_1 = L_2$, we retrieve the following laterally averaged concentration for a symmetric hourglass channel

$$c_{R,\infty}(x) = \begin{cases} 2\rho_b + \frac{\Delta\rho}{\text{Pe}}\left[\frac{R_t}{R(x)}\left(1+\frac{x}{L}\right) + \frac{4R_b}{\text{Pe}R_t}\frac{1-\exp\left[\frac{\text{Pe}}{2}\left(1+\frac{x}{L}\right)\frac{R_t^2}{R_bR(x)}\right]}{1+\exp\left[\frac{\text{Pe}}{2}\frac{R_t}{R_b}\right]}\right] & \text{for } -L_1 \le x \le 0 \\[4ex] 2\rho_b + \frac{\Delta\rho}{\text{Pe}}\left[\frac{R_t}{R(x)}\left(1-\frac{x}{L}\right) - \frac{4R_b}{\text{Pe}R_t}\frac{1-\exp\left[-\frac{\text{Pe}}{2}\left(1-\frac{x}{l}\right)\frac{R_t^2}{R_bR(x)}\right]}{1+\exp\left[-\frac{\text{Pe}}{2}\frac{R_t}{R_b}\right]}\right] & \text{for } 0 \le x \le L_2. \end{cases}\tag{4.17}$$

We can test the accuracy of the salt concentration $c_{R,\infty}$ from Eq. (4.14) by comparing it to results from finite-element calculations, with parameters and system parameters as given in Tab. 1.

(a)   (b)
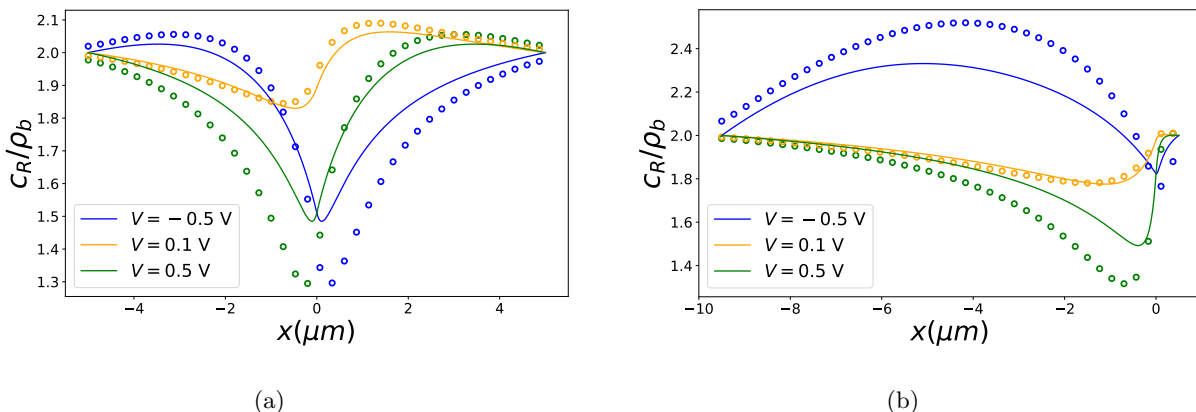
Figure 8: The analytic radially averaged salt concentration $c_R(x)$ from Eq. (4.14), are compared to the concentration in the centre of the channel of finite-element numerical calculations, denoted by the circles. The channels considered have (a) a ratio $\delta = 0.0$ and (b) a ratio $\delta = 0.9$, over which a static potential difference V is applied.

In Fig. 8 the concentration c_R from Eq. (4.14) is compared to the concentration in the central channel axis from FE-calculations. The analytic expression generally accurately mimics the salt concentration encountered in the numerical FE-calculations. The theory predicts the general behaviour of the concentration in a channel under an applied voltage, but it underestimates the change in concentration for higher voltages, which can be seen for $V = -0.5$ V and $V = 0.5$ V in Fig. 8(a) and Fig. 8(b).
From Fig. 8 it becomes clear that both the geometry of the channel and the applied potential difference determine the salt concentration in the channel. Especially the sign of the applied potential difference determines if there is a general concentration increase or decrease in the channel, especially for more asymmetric channels with high δ.

By integrating Eq. (4.14) over the length of the channel we can find the laterally averaged salt concentration, which results in the following expression

$$c_{L,\infty}[V] = \frac{1}{L_1 + L_2} \int_{-L_1}^{L_2} c_{R,\infty}[V, x] dx$$

$$= 2\rho + \frac{\Delta\rho}{\text{Pe}} \frac{1}{\Delta R^2} \left[R_t \left(R_b \log\left[\frac{R_b}{R_t}\right] - \Delta R \right) \right. \tag{4.18}$$

$$+ \frac{R_b}{\text{Pe}\left(e^{\text{Pe}\frac{R_t}{R_b}} - 1\right)} \left(\frac{4\Delta R}{1 - \delta^2} \left(1 + e^{\text{Pe}\frac{R_t}{R_b}} - e^{\text{Pe}\frac{(1+\delta)R_t}{2R_b}} - e^{\text{Pe}\frac{(1-\delta)R_t}{2R_b}} \right) \right.$$

$$+ \frac{1+\delta}{1-\delta} \text{Pe} R_t e^{-\text{Pe}\frac{(1+\delta)R_t^2}{2R_b\Delta R}} \left(1 - e^{\text{Pe}\frac{(1-\delta)R_t}{2R_b}} \right) \left(\text{Ei}\left[\text{Pe}\frac{(1+\delta)R_t}{2\Delta R} \right] - \text{Ei}\left[\text{Pe}\frac{(1+\delta)R_t^2}{2R_b\Delta R} \right] \right)$$

$$+ \left. \frac{1-\delta}{1+\delta} \text{Pe} R_t e^{\text{Pe}\frac{(1-\delta)R_t}{2\Delta R}} \left(1 - e^{\text{Pe}\frac{(1+\delta)R_t}{2R_b}} \right) \left(\text{Ei}\left[-\text{Pe}\frac{(1-\delta)R_t}{2\Delta R} \right] - \text{Ei}\left[-\text{Pe}\frac{(1-\delta)R_t^2}{2R_b\Delta R} \right] \right) \right) \right].$$
$$\tag{4.19}$$

This expression includes the exponential integral function $\text{Ei}(z)$, which is defined as

$$\text{Ei}(z) = \int_{-\infty}^{z} \frac{e^t}{t} dt. \tag{4.20}$$

The potential difference dependence of the laterally averaged concentration $c_{L,\infty}$ lies in the Péclet number Pe and in the factor $\Delta\rho$.

In Fig. 9 the salt concentration from Eq. (4.19) is compared to the concentration from FE-calculations, performed using the parameters of Tab. 1. The general concentration is described well by Eq. (4.19), as it accurately predicts that a positive potential difference in general leads to a concentration decrease, whereas a negative potential difference can lead to an increase in concentration. This increase mostly occurs for larger values of δ; the difference between the concentration in the case of a negative voltage and of a positive voltage is greater for higher values of δ. In comparison, for $\delta = 0.0$ the sign of the applied potential does not have an influence on the concentration in the channel.

The analytic expression, however, fails in predicting the magnitude of the concentration. It generally underestimates the change from the bulk concentration $c_L = 2\rho_b$ as a potential difference is applied, which is the case for both increases as decreases in concentration. However, in describing the memristive behaviour we are mostly interested in the general behaviour of the channel and we therefore will continue to use Eq. (4.19) for the calculations in this thesis.

We can expand the concentration in Eq. (4.19) in powers of V, which gives

$$c_{L,\infty}[V] = 2\rho_b \left(1 + \alpha V + \beta V^2 + \mathcal{O}\left[V^3\right] \right), \tag{4.21}$$

where the factors α and β are given by

$$\alpha = -e\sigma \frac{2\Delta R + (R_b + R_t)\log\left[\frac{R_t}{R_b}\right]}{2\rho_b k_B T \Delta R^2} \delta \tag{4.22}$$

$$\beta = \frac{1}{2\rho_b} \frac{e\epsilon_0\epsilon_r\sigma\psi_0}{24 D k_B T R_b \Delta R^3 \eta} \left[-\Delta R \left(2R_b^2 + 5R_b R_t - R_t^2 \right) - 6\log\left[\frac{R_b}{R_t}\right] R_b^2 R_t \right.$$

$$+ \left. \left(-\Delta R \left(10R_b^2 + 7R_b R_t + R_t^2 \right) + 2\log\left[\frac{R_b}{R_t}\right] R_b \left(2R_b^2 + 5R_b R_t + 2R_t^2 \right) \right) \delta^2 \right]. \tag{4.23}$$
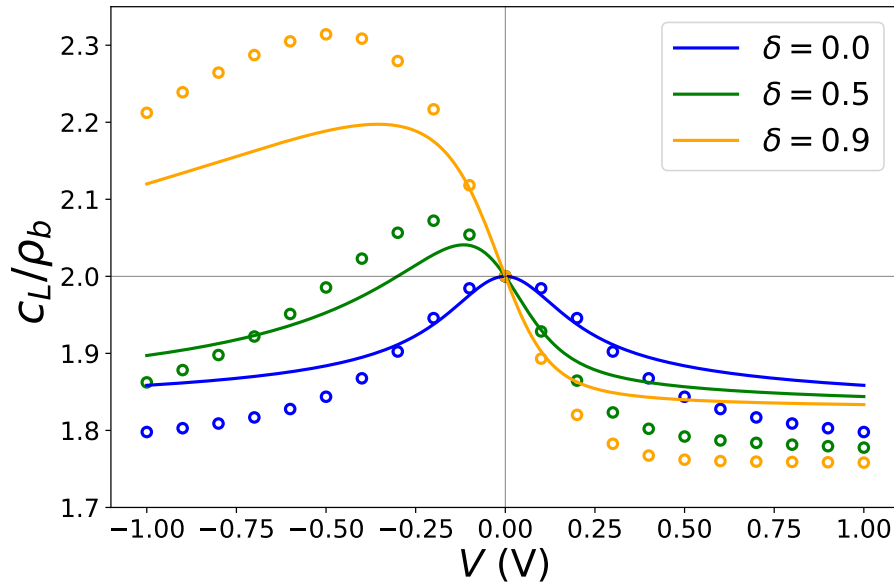
Figure 9: The laterally averaged concentration c_L in channels with various geometries, characterised by δ, over a range of steady state potential differences V. The results from FE-calculations, indicated by circles, are compared to the theoretical expression of 4.19, indicated by lines.

We can see from Eq. (4.22) that α is linear in terms of geometry parameter δ. From Eq. (4.23) we find that β has two terms: a constant term and a term quadratic in δ. In a perfectly symmetric channel, which has a ratio $\delta = 0$, there is clearly no linear V-contribution to the concentration $c_{L,\infty}$, because in this case the factor $\alpha = 0$. There is, however, always a quadratic contribution to the concentration, as β possesses a constant term, which does not depend on δ. Only as δ becomes non-zero, the concentration gains a linear voltage contribution that increases in significance when δ gets larger, as α also increases.

The concentration $c_{L,\infty}$ in general does not depend on odd powers of V if the channel is symmetric, since the sign of the applied voltage cannot have an influence on the concentration in the symmetric case, as a change of sign amounts to a change of direction in which the potential difference is applied. In a symmetric channel this change of direction makes no difference for the laterally averaged concentration.

4.2   Ionic Current

We can find an expression for the current I through the channel by radially integrating Eq. (4.1) for the electric flux. In determining the salt flux we worked in the long channel limit, which allowed us to ignore the radial coordinate r and to use the radially averaged salt concentration $\rho_s(r, x) \approx c_R(x)$. The other assumption we made was that the charge is negligible outside the EDL, so $\rho_e(r \ll R - \lambda_D) \approx 0$. We make the same approximations in determining the total current I through the channel. Under these assumptions only the conductive part of the charge flux in Eq.

(4.1) remains, as we neglect the terms which contain charge density ρ_e, which results in

$$I_c(x) = 2\pi \int_0^{R(x)} ej_{e,x}(x,r,t)rdr = -2\pi \int_0^{R(x)} eDc_R(x)\frac{e\partial_x\psi(x)}{k_BT}rdr$$

$$= -eD\frac{e\partial_x\psi}{k_BT}\pi R^2(x)c_R(x) = eD\frac{eV}{2Lk_BT}\pi R_b R_t c_R(x), \tag{4.24}$$

where we have substituted the electric field of Eq. (4.10) into the expression for $I(x)$. The conductive current now depends on the coordinate x, which is problematic if we want to determine the current of the channel, if we treat it like a circuit element, as a circuit element can only give a single current output from its applied input. We can instead use the laterally averaged channel conductivity to cancel out this x-coordinate dependence, which gives

$$I_{c,L} = eD\frac{eV}{2Lk_BT}\pi R_b R_t \int_{-L_1}^{L_2} dx\frac{c_R(x)}{2L} = eD\frac{eV}{2Lk_BT}\pi R_b R_t c_L. \tag{4.25}$$

In Section 4.1 we found an expression for the laterally averaged steady state salt concentration $c_{L,\infty}$. We are therefore now able to predict the conductive current in the steady state. From this expression above we can also define the conductivity of the channel if no potential difference is applied, which is

$$G_0 = 2\rho_b eD\frac{e}{2Lk_BT}\pi R_b R_t = \frac{2\rho_b e^2 D}{k_BT}\frac{\pi R_b R_t}{2L}, \tag{4.26}$$

where the bulk salt concentration $c_L = 2\rho_b$ was inserted and we divided the expression into a geometric term and a related to the charged ions.

For the time-dependent concentration we use the following Ansatz. We assume that the time derivative of the laterally averaged current in the channel is proportional to the difference between the actual concentration and the steady state concentration of the applied potential difference, which gives

$$\tau\partial_t c_L(t) = c_L(t) - c_{L,\infty}[V(t)], \tag{4.27}$$

where τ is some appropriate timescale of the system that indicates in what time the concentration changes, when a potential difference is applied over the channel. We can use the expression for $c_{L,\infty}$ from Eq. (4.19) in the equation above. This Ansatz is very similar to the one made in Eq. (3.1) for the conductivity of a memristor. To adapt this differential equation to the general Ansatz of Eq. (3.1) all densities c_L need to be multiplied as follows

$$g(t) = \frac{\pi R_b R_t}{L}\frac{e^2 Dc_L(t)}{k_BT} \tag{4.28}$$

in order to find the memductance of the channel.

4.2.1 Timescale τ

To solve the differential equation in Eq. (4.27) it is necessary to find an appropriate timescale τ of the nanopore. We can find an approximate expression for time constant τ using the salt current $J(x,t)$ and the steady state salt concentration $c_{R,\infty}(x)$, which can be related to each other by continuity Eq. (4.4). By integrating this equation radially the continuity equation condenses to

$$\partial_t \left(\pi R^2(x)c_R(x)\right) = -\partial_x J(x), \tag{4.29}$$

where $c_R(x)$ is the radially averaged salt concentration.

If we in turn integrate $c_R(x)\pi R^2$ laterally over entire length of the channel, we find the total ion number N in the channel:

$$\int_{-L_1}^{L_2} dx \pi R^2(x) c_R(x) = N \tag{4.30}$$

Integrating the right-hand side of Eq. (4.29) gives

$$\int_{-L_1}^{L_2} dx \partial_x J(x) = J(L_2) - J(-L_1). \tag{4.31}$$

Combining these results with Eq. (4.29) we find $\partial_t N = -(J(L_2) - J(-L_1))$, which we use to find an approximate timescale τ by taking

$$\tau = \frac{N}{\partial_t N} = \frac{\int_{-L_1}^{L_2} dx \pi R^2(x) c_R(x)}{-(J(L_2) - J(-L_1))}, \tag{4.32}$$

where we insert the concentration $c_R(x) = c_{R,\infty}(x)$ from Eq. (4.14). This timescale follows from the amount of salt added to the channel, divided by the rate at which this occurs. However, we derived $c_{R,\infty}(x)$ using the equation $\partial_x J = 0$, so under this concentration $J(L_2) - J(-L_1) = 0$, which we cannot use in determining timescale τ.

We can instead consider a channel with constant concentration, so $\partial_x c_R = 0$, and determine the salt flux when we apply a potential difference V; this is the salt flux caused by a sudden change from $V = 0$ to $V = \Delta V$. From Eq. (4.5) and Eq. (4.10) we find that the flux in this case is

$$J_{\partial_x c_R = 0} = -\pi D\sigma \frac{e\Delta V}{L k_B T} \frac{R_b R_t}{R(x)}. \tag{4.33}$$

As $R(-L_1) = R(L_2) = R_b$, we again find that $J(L_2) - J(-L_1) = 0$, which results in the same problem as before. However, if we only consider the channel section from $x = -L_1$ to $x = 0$, which amounts the cone with length L_1, we get

$$\partial_t N_{(x<0,\partial_x c_R=0)} = -[J(0) - J(-L_1)] = \pi D\sigma \frac{eV}{L k_B T}\Delta R, \tag{4.34}$$

so the change in the ion number in the lower cone has a linear V-dependence.

We now determine the total ion-number of the cone with length L_1 and expand it in powers of V, to find

$$N_\infty[V] = \int_{-L_1}^{0} \pi R^2(x) c_{R,\infty}(x) = 2N_0 + \Delta N_1[V] + \mathcal{O}[V^2], \tag{4.35}$$

where $N_0 = \rho_b \pi L_1 (R_t^2 + \Delta R^2/3 + R_t \Delta R)$ and the first order term ΔN_1 is

$$\Delta N_1 = \frac{e\sigma \pi L_1^2 \Delta R}{12 L k_B T}V = \frac{e\sigma(1+\delta)^2 L^2 \pi \Delta R}{12 L k_B T}V. \tag{4.36}$$

Using the first order expansion-term ΔN_1 and the flux term from Eq. (4.34) we find the following estimate for τ,

$$\tau = \frac{\Delta N_1}{\partial_t N_{(x<0,\partial_x c_R=0)}} = \frac{(1+\delta)^2 L^2}{12D}, \tag{4.37}$$

which increases as δ increases.

4.3   Capacitance

The main characteristic which determines the current running through an ionic nanochannel, is its conductance. However, the channel can also possess a capacitive element, leading to charge buildup in the channel as a voltage is applied; non-zero charge densities of opposite sign can form in areas on opposite sides of the centre of the channel. This capacitive element influences the current measured in this channel. We can add a capacitive effect to the theoretical model by putting a capacitor parallel to the memristor, which results in the circuit element as illustrated in Fig. 4.

From Eq. (3.4) we find that the current over a capacitor is $I_C = C\frac{\partial V_C(t)}{\partial t}$. To find the total current over the memristive pore we need to add the capacitive current to the current we found using the techniques discussed in Section 4.2, such that the total current is given by

$$I_{tot}(t) = eD\frac{eV(t)}{2Lk_BT}\pi R_b R_t c_L(t) + C\frac{\partial V(t)}{\partial t}. \tag{4.38}$$

In this thesis a periodic voltage $V(t) = V_0 \sin[\omega t]$ is applied over the memristor. In the case of this periodic voltage the capacitive current becomes

$$I_C = V_0 \omega \cos[\omega t]. \tag{4.39}$$

The capacitive current contribution get larger as angular frequency ω increases and therefore the capacitive element dominates at large frequencies in this model.

James Hall gave a relation between the capacitance C and the resitance R of a circular nanopore with a given geometry in a 1975 letter [57], which is

$$C = \frac{\epsilon \rho_m}{R}, \tag{4.40}$$

where ϵ is the permittivity and ρ_m the resistivity of the medium present in the pore. We can extract an estimate for the resistance R of the channel from Eq. (4.26), which describes the steady state conductance G_0 of the channel, by taking $R = 1/G_0$. Combining Eq. (4.25) and Eq. (4.40) we find the following estimate for the capacitive current over the channel

$$I_C(t) = \epsilon_0 \epsilon_r \rho_m \frac{\rho_b e^2 D}{k_B T} \frac{\pi R_b R_t}{L} \frac{\partial V(t)}{\partial t}. \tag{4.41}$$

5 Results

In this section we inspect the conductive properties of ionic channels under the application of steady state voltages and periodically oscillating voltages, which we both extract from finite-element calculations. The results from these calculations will then be compared to the results from the model developed in Sections 3 and 4.

5.1 Finite-Element Calculations

In Fig. 10(a) the current response of a symmetric hourglass channel and a conical channel under a stationary current are shown. In both the completely symmetric channel, indicated by $\delta = 0$, and the conical channel, indicated by $\delta = 0.95$, we find that the linear Ohmic resistance dominates, but if we subtract the Ohmic current from the total current, as we do in Fig. 10(b), the difference between the current responses of the two channels becomes clear. For $\delta = 0.95$, we find diodic behaviour; if the potential difference is negative, the conductivity is larger than if it is positive. For $\delta = 0.0$ this diodic behaviour is not present, but there is a slight sigmoidal shape to its curve in Fig. 10(b), which indicates a difference in behaviour between the low potential difference and high potential difference regime.
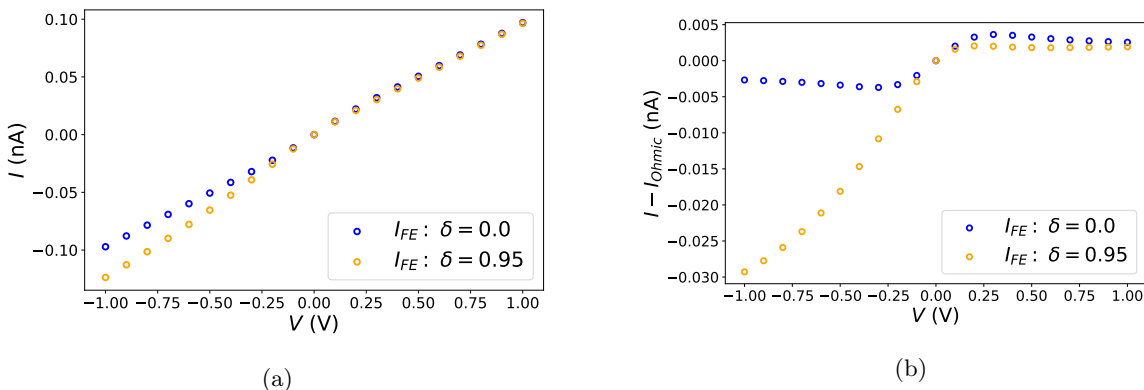

Figure 10: (a) The total current I and (b) the non-Ohmic current $I - I_{\text{Ohmic}}$ in channels with $\delta = 0.0$ and $\delta = 0.95$, as the result of the application of a static potential difference V. The results come from FE-calculations.

We can also apply a periodic potential difference $V(t) = V_0 \sin [2\pi f t]$ over the ionic channels instead of a stationary voltage. In Fig. 11(a) the result is plotted for a calculation, in which we used a frequency $f = 75$ Hz and an amplitude $V_0 = 0.5$ V.

The current as plotted in Fig. 11(a) is again dominated by the linear resistance component of the channel, but if we again subtract the linear current from the total current, as we do in Fig. 11(b), we can more clearly see the memristive behaviour. Subtracting the Ohmic current from the total current will be common practice for the rest of this thesis, as we are interested in the type of memristive behaviour nanopores exhibit.

For both $\delta = 0.0$ and $\delta = 0.95$ the current response to an applied voltage results in a pinched hysteresis loop in the IV-diagram. The curve for $\delta = 0.95$ crosses itself once, at the origin, which indicates that this channel behaves as a *type-I memristor*. The curve for $\delta = 0.0$ does not cross itself, but the two ends of the curve do approach each other at the origin, which is indicative of a *type-II memristor* with an additional capacitive element.
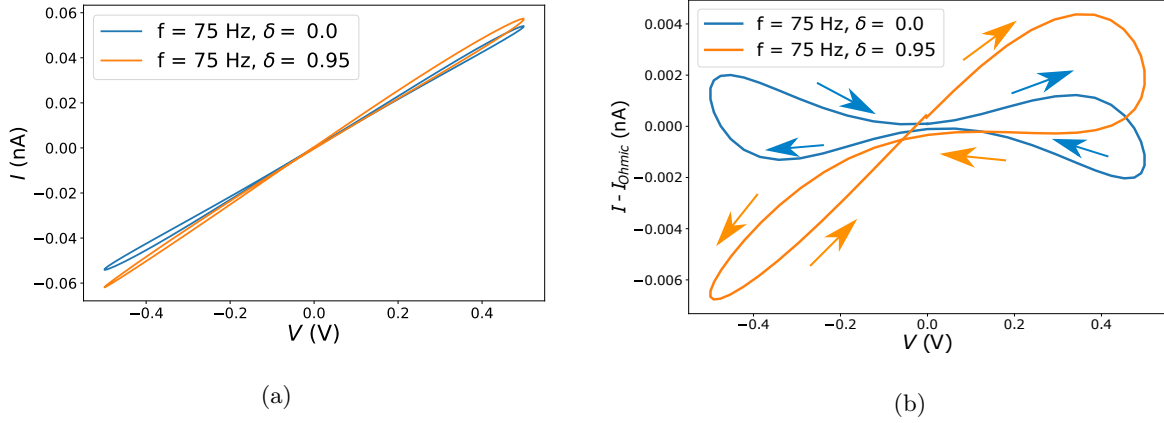
(a)

(b)

Figure 11: (a) The total current I and (b) the non-Ohmic current $I - I_{Ohmic}$ in channels with $\delta = 0.0$ (blue) and $\delta = 0.95$ (orange), as the result of the application of a periodic potential difference $V(t) = V_0 \sin [2\pi f t]$ with frequency $f = 75$ Hz, extracted from FE-calculations. The loop for $\delta = 0.0$ shows type-II behaviour and the loop for $\delta = 0.95$ type-I behaviour.

If we increase δ from $\delta = 0.0$ to $\delta = 0.95$ we encounter a change from a type-II memristor to a type-I memristor, characterised by a change in the number of crossings of their respective hysteresis loops. As δ increases and we move from a symmetric channel to a conical one, the hysteresis-type clearly changes. However, as we increase δ and move from type-II behaviour to type-I memristive behaviour, there is an intermediate type of hysteresis behaviour, in which the hysteresis loop has two crossings. We denote this type of hysteresis behaviour as belonging to a *type-c memristor*; the letter c refers to the two crossings in a type-c hysteresis loop. In Fig. 12 one can see this intermediate crossing behaviour in the hysteresis loop for a channel with $\delta = 0.6$, in which the two crossings are present in the third quadrant of the IV-diagram, with one positioned close to the origin and the other positioned farther in the lower left corner.
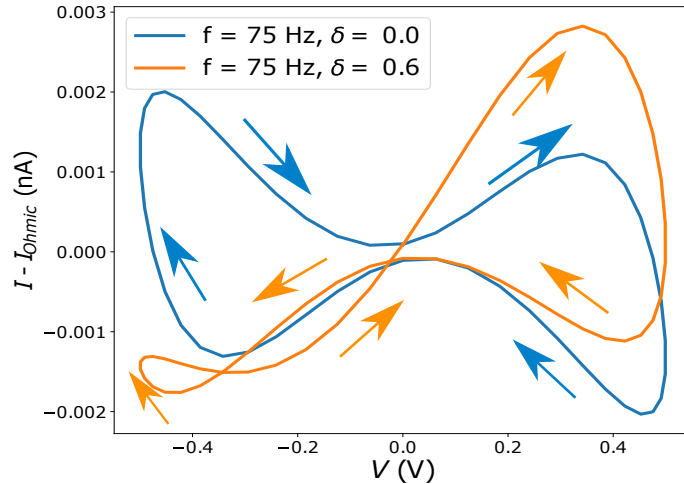

Figure 12: Current-voltage hysteresis loop for ionic nanochannels with $\delta = 0.0$ and $\delta = 0.6$, as the result of the application of a periodic potential difference $V(t) = V_0 \sin [2\pi f t]$ with frequency $f = 75$ Hz, extracted from FE-calculations. The loop for $\delta = 0.0$ shows type-II behaviour and the loop for $\delta = 0.6$ type-c behaviour.

5.1.1   Frequency Dependence

In the previous section the effect of changing the channel geometry through the ratio δ was investigated at a single frequency of $f = 75$ Hz. Changing the frequency also has an effect on the current-voltage hysteresis behaviour of a memristor. In Fig. 13 the hysteresis loops for a range of frequencies are shown for a ratio of $\delta = 0.0$, from which two general features can be found. At very low frequencies the total enclosed loop area is small, but this area increases as the frequency becomes higher, yet at even higher frequencies this area decreases again. The second feature is that the specific non-linear resistive features of the channel become less pronounced and eventually disappear, as the frequency increases. At $f = 1.0$ Hz the conductivity is smaller at higher potential differences than at low potential differences, which is the result of a lower salt concentration in the channel. At $f = 1000$ Hz the conductivity of the channel is almost linear and the hysteresis loop closes. This is behaviour associated with volatile memristors, as discussed in Section 2.1. At low frequencies a memristor behaves like a non-linear resistor, while it behaves like a linear-resistor at high frequencies.
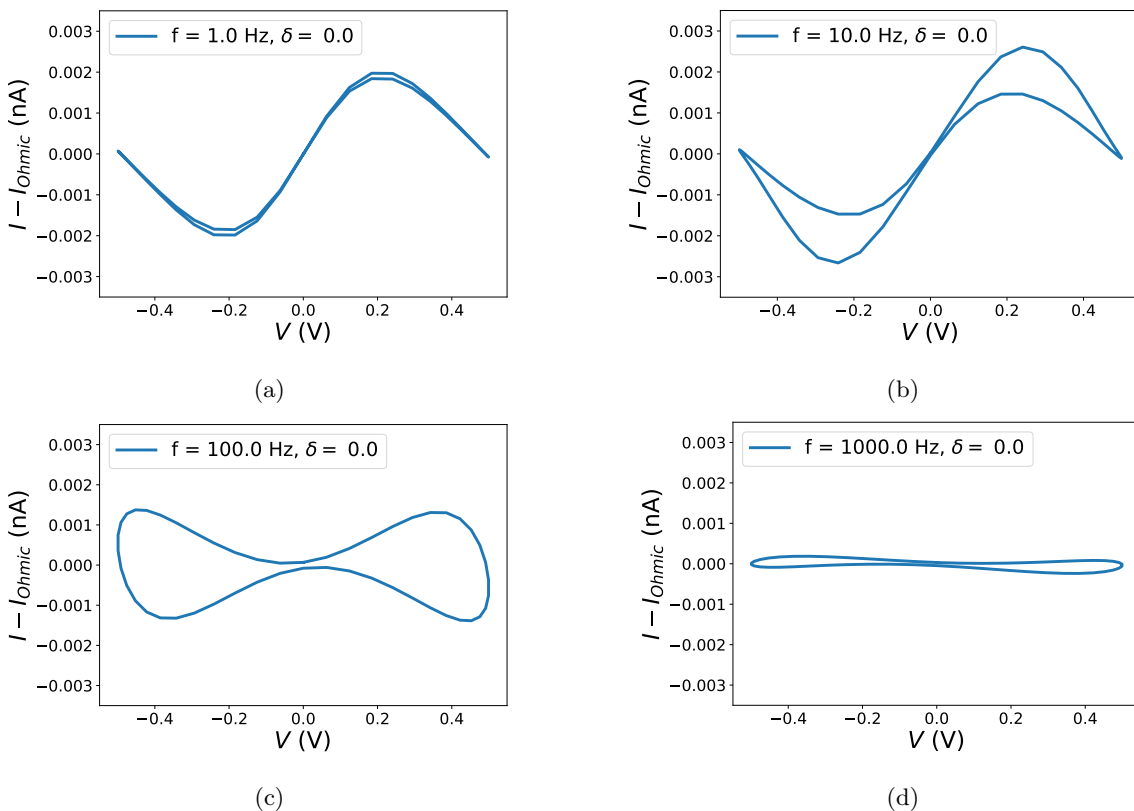

Figure 13: The non-Ohmic current in channels with $\delta = 0.0$, as the result of the application of a periodic potential difference $V(t) = V_0 \sin[2\pi f t]$, extracted from FE-calculations. The driving frequency f in the figures is (a) $f = 1$ Hz, (b) $f = 10$ Hz, (c) $f = 100$ Hz and (d) $f = 1000$ Hz

All hysteresis loops in Fig. 13 are indicative of type-II memristive behaviour; changing the frequency does not alter the memristor-type for a symmetric ionic channel. However, changing the frequency can have an effect on the memristive behaviour of a channel, which can be seen in Fig. 14, in which the hysteresis loops of a channel with $\delta = 0.5$ are plotted for various potential difference frequencies f. Similar to the channel with $\delta = 0.0$, one can see that the non-linear resistive effects of the channel

decrease with higher frequencies and that the loop area first increases and then decreases as the frequency increases. A different feature is that the hysteresis-type changes: for $f = 1, 10, 100$ Hz the loops have 2 crossings, but for $f = 1000$ Hz there are none, which constitutes a change from type-c behaviour to type-II memristive behaviour.
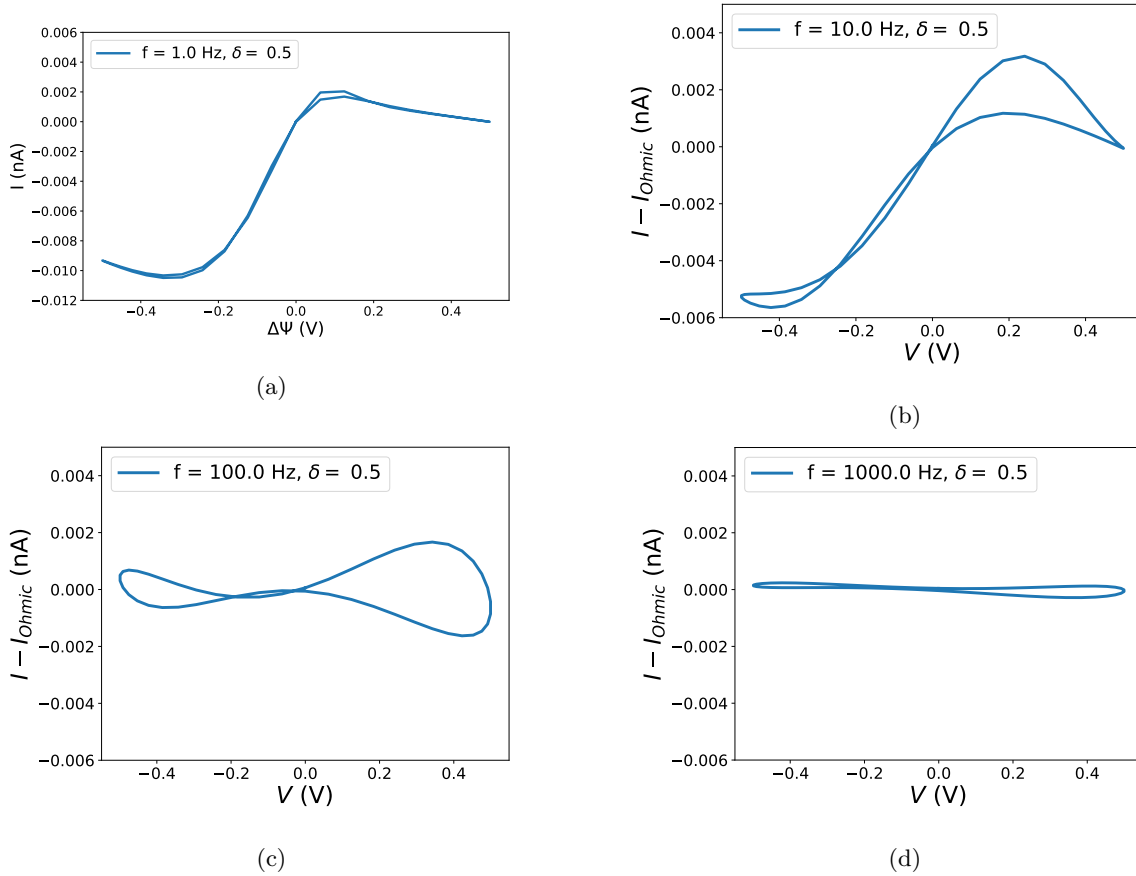

Figure 14: The non-Ohmic current in channels with $\delta = 0.5$, as the result of the application of a periodic potential difference $V(t) = V_0 \sin[2\pi ft]$, extracted from FE-calculations. The driving frequency f in the figures is (a) $f = 1$ Hz, (b) $f = 10$ Hz, (c) $f = 100$ Hz and (d) $f = 1000$ Hz

5.1.2   Hysteresis Loop Area

In Fig. 13 and Fig. 14 one can see that the enclosed hysteresis loop area changes as the frequency of the applied voltage changes; altering the factor δ can also change this area. We can find the loop area by integrating the current over the voltage,

$$S = \int I(t)dV = \int I(t)\frac{\partial V}{\partial t}dt = \int I(t)\omega V_0 \cos[\omega t]\,dt, \qquad (5.1)$$

with $\omega = 2\pi f$ the angular frequency. The area S has a power dimension and therefore has the unit Watt (W). We introduce a dimensionless parameter $\hat{S}$ for the area of the hysteresis loop, which considers a single period T of voltage oscillations,

$$\hat{S} = \frac{1}{V_0^2 G_0}\int_{nT}^{nT+T} I(t)\omega V_0 \cos[\omega t]\,dt, \qquad (5.2)$$

which covers the entire hysteresis loop, with $n \in \mathbb{Z}$ an integer. In this equation G_0 is the rest conductivity over the channel as defined in Eq. (4.26) and V_0 the amplitude of the potential difference oscillation.

In Fig. 14 we saw that the hysteresis loop can cross itself, which results in a negative contribution to the integral S; these crossings occur in the second half of the voltage oscillation period, when potential difference V is negative. By integrating over the time $t \in [nT, nT + T/2]$, with $n \in \mathbb{Z}$, we only consider positive contribution to the area S, which allows us to better compare the hysteresis area of channels with different geometries. For this purpose we define the following dimensionless parameter

$$\hat{S}_1 = \frac{1}{V_0^2 G_0} \int_{nT}^{nT+T/2} I(t)\omega V_0 \cos\left[\omega t\right] dt, \tag{5.3}$$

In Fig. 15(a) the area $\hat{S}_1$ is plotted for a range of frequencies f, for a set of channels with different values of δ. All channels have the largest loop area for intermediate frequencies, of around $f = 50$ Hz. It is interesting to see that there are large differences in area $\hat{S}_1$ between various geometries, indicated by δ. The smallest values are found for the symmetric hourglass channel with $\delta = 0.0$, but when δ increases and the channel becomes more conical, the area $\hat{S}_1$ increases as well. This increase of the peak value occurs at a linear pace with δ and the frequency at which this peak occurs decreases as δ increases.

In Fig. 15(b) the area $\hat{S}$ is plotted for various values of δ over a range of frequencies f. From this figure we find that the value of $\hat{S}$ decreases in general as δ increases, which is the opposite of what we saw for $\hat{S}_1$. This is a consequence of the hysteresis loops possessing crossings for higher values of δ, which means that the negative contribution to $\hat{S}$, discussed in this section above, is larger for these larger δ-values. However, we again find that the peak value frequency of $\hat{S}$ is around $f = 50$ Hz and that this peak area frequency decreases with δ.
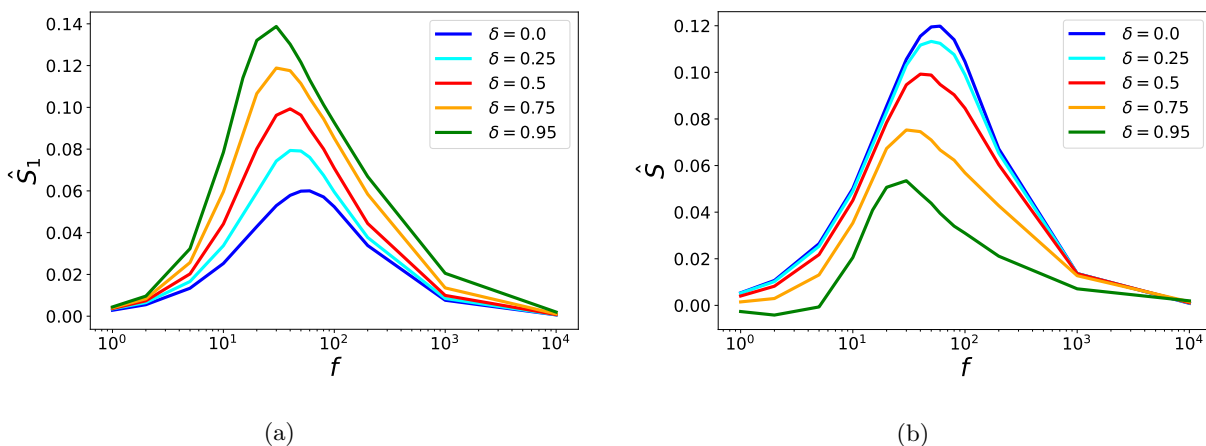

Figure 15: Hysteresis area (a) $\hat{S}_1$, as defined in Eq. (5.3), and (b) $\hat{S}$, as defined in Eq. (5.2) over a range of potential difference frequencies f for channels with various ratio's δ, extracted from FE-calculations. Here $\hat{S} = 1$ corresponds to $S = 1.3$ pW.

5.1.3 Capacitive Element

We have encountered that when a voltage is applied over a nanochannel an ionic current forms. A second effect we encountered is a buildup of charges in the channel, as a result of a capacitive element in the system. This charge buildup, however, is quite minor and can easily be confused

with the charge density associated with the EDL. The effect of the EDL on the charge density in a cylindrical channel is given in Eq. (2.35) and we can use this equation to derive an expression for the charge density through the centre of the channel ($r = 0$)

$$\rho_e\left[V\right] = 2c_L\left[V\right]\sinh\left[\frac{-4\pi\lambda_B\sigma}{\kappa\left[V\right]I_1\left(\kappa\left[V\right]R[x]\right)}\right], \tag{5.4}$$

where the V-dependence of the concentration is now also considered. The Debye length κ^{-1}, defined in Eq. (2.25), now also depends on V through c_L as follows,

$$\kappa^{-1} = \sqrt{\frac{2c_L(V)e^2\beta}{\epsilon_0\epsilon_r}}.$$

In Fig. 16(a) the charge density in the centre of a channel extracted from numerical calculations, is compared to the charge density from Eq. (5.4), for the case that no voltage is applied over the channel. In both results the effect of the geometry is obvious, as we find the largest density at the location with the smallest radius, at $x = 0$, since the influence of the EDL is largest at this point. The numerical and analytic results agree largely, except for the width of the charge density peak, which is slightly larger for the numerical results.
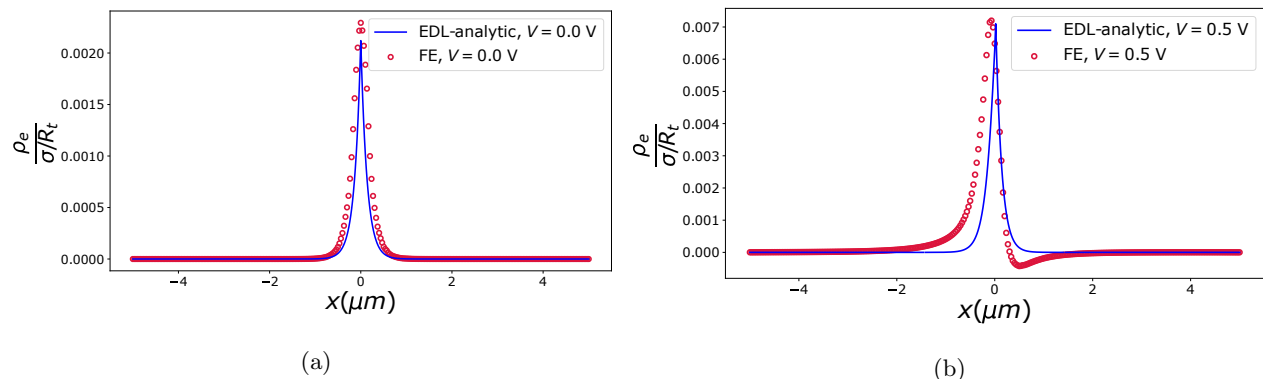

(a)
(b)

Figure 16: Ionic charge density through the centre of a ionic channel with $\delta = 0.0$ under a potential difference of (a) $V = 0.0$ V and (b) $V = 0.5$ V. Results from FE-calculations and analytic calculations using the EDL thickness are compared. The charge density $\rho_e = \rho_+ - \rho_-$ is given in terms of the surface charge density per tip-radius σ/R_t.

In Fig. 16(b) the effect of applying a potential difference of $V = 0.5$ V over the channel is shown. From the finite-element results calculations we find that the symmetric peak is now asymmetric, with the charge density increasing for $x < 0$ and decreasing for $x > 0$, with respect to the calculation for $V = 0.0$ V. This can be a result of two effects; the first one is the change in salt concentration c_L in the channel resulting in a change of the thickness of the EDL, which can explain the change in ρ_e, but not the negative ρ_e encountered in Fig. 16(b). Although the overall increase in ρ_e is predicted well by the analytic model, the charge asymmetry in the channel is not found in the model. The second possible cause for this charge density change is the capacitive element present in the channel. Indicative for this capacitive element would be a positive charge buildup in one area of the channel and a negative charge buildup in another area, which is what we encounter in the channel when a potential difference is applied. The negative charge density in Fig. 16(b) can also be explained by capacitance.
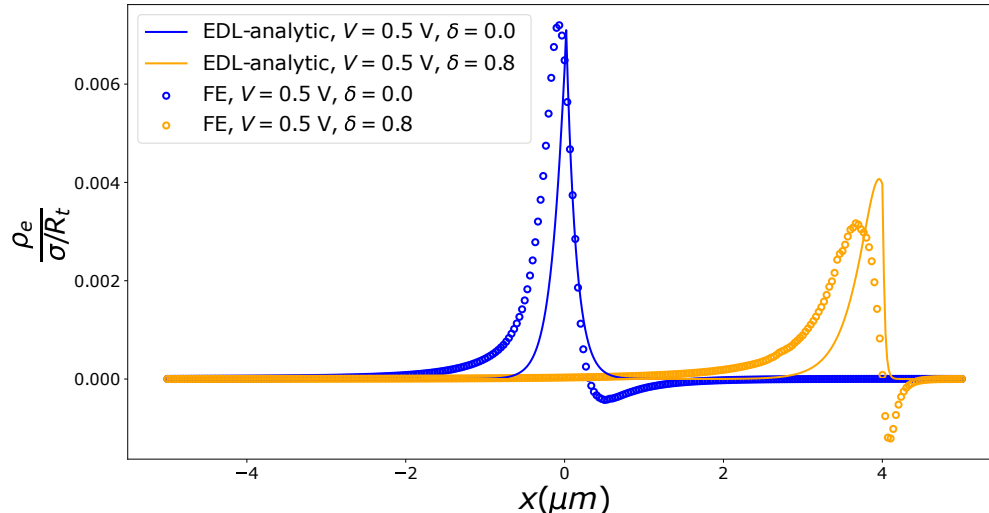
Figure 17: Charge density through the centre of a ionic channel with different values of δ under potential difference $V = 0.5$ V. Results from FE-calculations and analytic calculations are compared. The charge density $\rho_e = \rho_+ - \rho_-$ is given in terms of the surface charge density per tip-radius σ/R_t.

In Fig. 17 we compare the charge density for channels with different values of δ. The expression for ρ_e in Eq. (5.4) accurately predicts that at larger δ the peak charge density is larger and that it spreads out asymmetrically, but it again cannot predict the negative charge density associated with the capacitive element of the channel. In the FE-results for a channel with $\delta = 0.8$ we now encounter a larger negative charge density than for a channel with $\delta = 0.0$, but the negative charge density is spread out over shorter length.

To quantify the charge buildup we integrate the charge density over the negatively charged areas as follows,

$$q_{\mathrm{neg}} = \int_{\rho_e < 0} dx e \rho_e (x) \pi R^2(x), \tag{5.5}$$

where we have included the channel cross section area term $\pi R^2(x)$ in the integration, to account for the change in radius in determining the total charge. The charge q_{neg} can give an indication of the total charge buildup on one end of the capacitor.

To find an estimate of the capacitance in the channel we treat the capacitive element in the channel as a standard parallel-plate capacitor, with the charge-voltage relation given by $V = \frac{q}{C}$. We thus find the capacitance by taking $C = \frac{-q_{\mathrm{neg}}}{V}$.

In Fig. 18 the charge q_{neg} is shown over a range of potential differences. It is given as a ratio of $\sigma L R_t$, which is an indicator of the total EDL-charge in one half of the channel. Like we expected, the the absolute value of the total charge increases as the potential difference over the channel increases, which is a regular response for a capacitor to a voltage. However, the increase does not occur linearly, as would be expected from a capacitor, but occurs at a higher rate for larger V, although from $V = 0.4$ V on this increase does seem to occur linearly. The charge buildup in channels with different δ is similar, so it seems that the parameter δ has little influence on the capacitance of a certain pore.

By taking the charge buildup at $V = 1.0$ V for a channel with $\delta = 0.0$, we find an estimate for the capacitance, namely

$$C = \frac{-q_{\mathrm{neg}}}{V} = \frac{0.0027 \cdot 10^{-15}}{1.0} \text{ F} = 2.7 \cdot 10^{-18} \text{ F}, \tag{5.6}$$
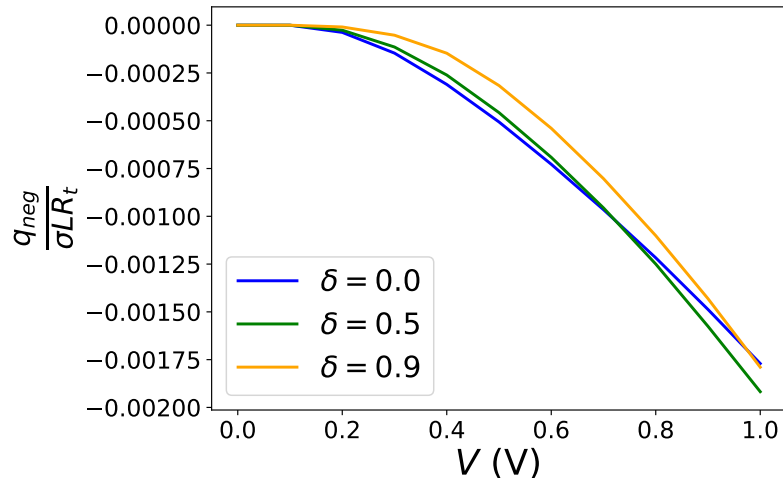
Figure 18: Total negative electric charge buildup in the channel q_{neg}, as defined in Eq. (5.5), extracted from FE-calculations. The negative charge is evaluated over a range of potential differences V and for multiple values of the geometry parameter δ.

which is a small capacitance. We can compare this to the Hall-capacitance estimate of Eq. (4.40), which is $C = \frac{\epsilon_r \epsilon_0 \rho_m}{R}$. We take the resistivity of water to be $\rho_m = 68 \ \Omega\mathrm{m}$ [58] and the resistance of the pore to be $R = 1/G_0$, with conductivity G_0 as given in Eq. (4.26). This gives the capacitance

$$C_{\mathrm{Hall}} = \epsilon_0 \epsilon_r \rho_m \frac{\rho_b e^2 D}{k_B T} \frac{\pi R_b R_t}{L} = 5.1 \cdot 10^{-18} \ \mathrm{F}, \tag{5.7}$$

which is of the same order as the capacitance we found through the derivation of q_{neg} from the numerical calculations. This estimate seems fairly accurate for the systems studied. We can also determine the RC-time of the channel from the Hall-estimate, which is given by

$$\tau_{RC,\mathrm{Hall}} = \epsilon_r \epsilon_0 \rho_m = 4.8 \cdot 10^{-8} \ \mathrm{s}. \tag{5.8}$$

Comparing this time to the characteristic timescale of the channel, as given in Eq. (4.37), we see that this time is much smaller than the characteristic timescale of the ionic channels, studied in this thesis. The RC-time is most probably not the characteristic time of the system.

5.2 Analytic Model: Zero Capacitance

Using the results from Section 4.2 we can try to reconstruct the results of the numerical simulations. The conductivity can be found by solving the differential equation in Eq. (4.27) for the salt concentration, in which we insert the potential difference $V(t) = V_0 \sin[2\pi f t]$, the timescale τ from Eq. (4.37) and the laterally averaged steady state concentration $c_{L,\infty}$ from Eq. (4.19). To find the resulting current from the potential difference and concentration we use

$$I(t) = \frac{De^2 c_L(t)}{k_B T} \frac{\pi R_b R_t}{2L} V(t),$$

from Eq. (4.25).

We first compare the results from the analytic model to the stationary FE-calculation. The current I as a result of an applied stationary voltage V is plotted in Fig. 19(a), which includes the current from the FE-calculations and the current as described by Eq. (4.25). The Ohmic linear current dominates, so we subtract it from the total current to obtain Fig. 19(b).
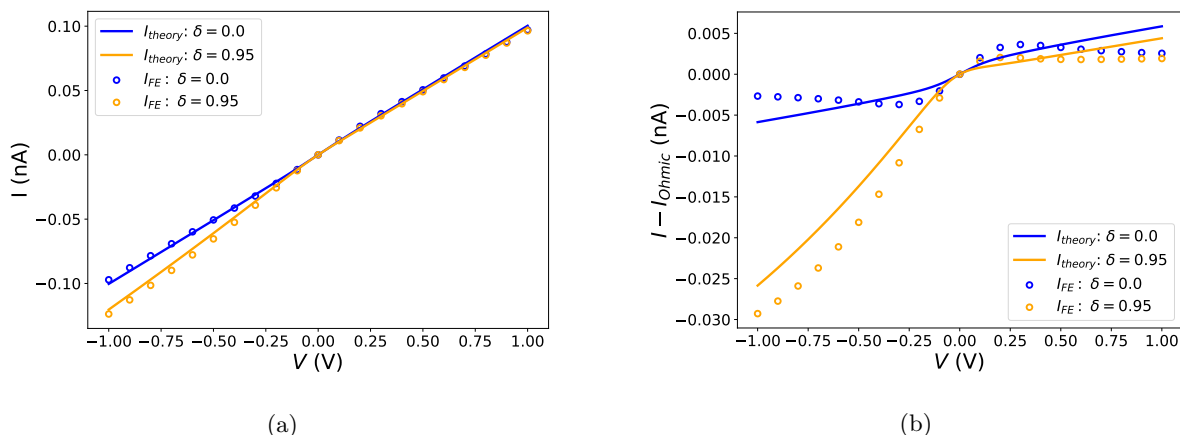

Figure 19: (a) The total current I and (b) the non-Ohmic current $I - I_{\text{Ohmic}}$ in channels with $\delta = 0.0$ and $\delta = 0.95$, as the result of the application of a static potential difference V. The current from finite-element calculations is indicated by the individual rings and the analytic current from Eq. (4.25) is indicated by the lines.

In Fig. 19(b) we can see that the analytically obtained current is very similar to the current from the FE-results. For $\delta = 0.0$ the current response shape is slightly sigmoidal, although not as much as the FE-calculations current. The current rectifying behaviour encountered in the pore with $\delta = 0.95$ is well predicted by Eq. (4.25); the conductivity is larger when a negative potential difference is applied than when a positive one is applied. This is a consequence of the salt concentration c_L decreasing with respect to its bulk value when a positive potential difference is applied for a channel with $\delta = 0.95$, while a negative potential difference in turn leads to an increase in concentration, as can be seen in Fig. 9. The conductivity linearly depends on the salt concentration, so this causes the pore to behave as a diode.

5.2.1 Symmetric Channel

We now apply the theory on the symmetric hourglass channel with $\delta = 0.0$ and inspect what occurs when an oscillating voltage is applied over the pore.

The following linear and quadratic V-dependence constants α and β, that come from Eq. (4.22) and Eq. (4.23), are associated with this channel,

$$\alpha = 0.0 \text{ V}^{-1}; \ \beta = -1.34 \text{ V}^{-2}; \ \tau = 2.1 \text{ ms.}$$

with timescale τ coming from Eq. (4.37). Because $\alpha = 0$, there is no linear potential difference contribution to the laterally averaged salt concentration in the channel. If we use the salt concentration $c_{L,\infty}$ from Eq. (4.19) in determining the concentration $c_L(t)$, using differential equation Eq. (4.27), for a channel with $\delta = 0.0$, we end up with the results in Fig. 20.
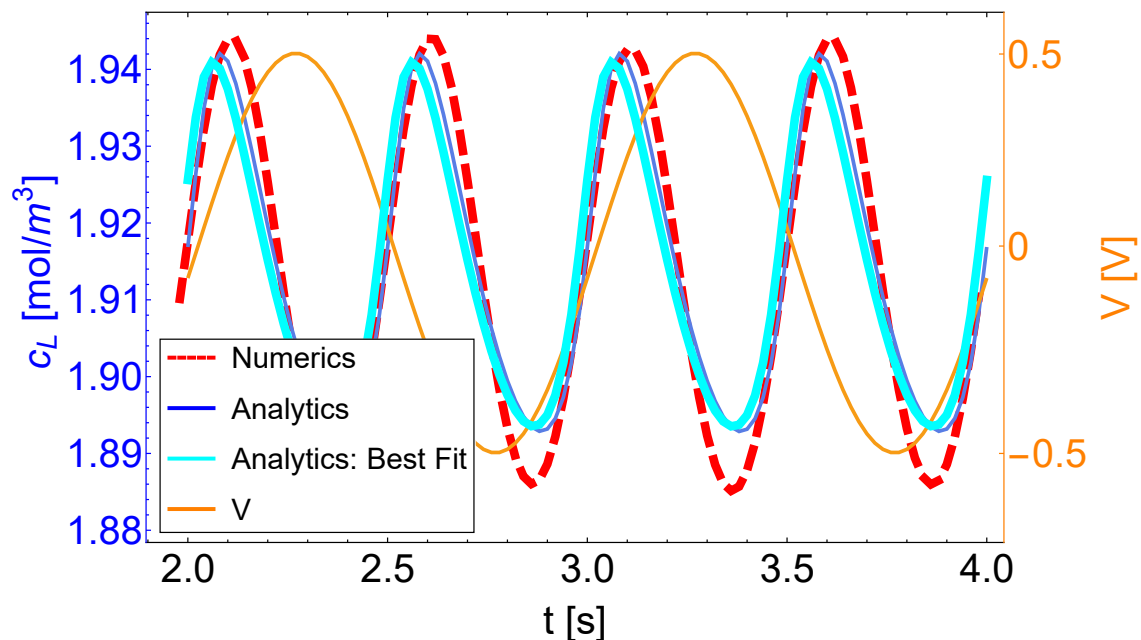

Figure 20: Laterally average salt concentration c_L against time for a channel with $\delta = 0.0$. A periodic voltage of $V(t) = V_0 \sin[2\pi f t]$ is applied over the channel, with $V_0 = 0.5$ V and frequency $f = 75$ Hz. The voltage is plotted in orange. The numerical and analytic results are compared. The numerical value for c_L is found by averaging the concentration through the centre line of the channel.

The numerical results and the analytic results in Fig. 20 are largely in agreement, qualitatively and quantitatively. Both the numerical and analytic laterally averaged concentration follow the same oscillating pattern, with oscillations having twice the driving frequency, though the peak concentration is observed to occur a bit later in the numerical calculations than in the analytic calculations. The numerical results and the analytic results have a similar oscillation amplitude and average value for c_L, but the amplitude of the numerical results is a bit larger.

The frequency of c_L is twice that of $V(t)$, which indicates that c_L largely depends on even terms of $V(t)$. The linear $V(t)$-dependence term in $c_{L,\infty}$ also dropped out for $\delta = 0.0$, as we found $\alpha = 0.0$. In symmetric systems, like the one being considered, we do not expect to find odd-powered terms in the expression for the conductivity.

We observe in Fig. 20 that the peak values for c_L occur a short time after the potential difference $V(t)$ reaches its peak, or after it reaches $V(t) = 0$. This makes it clear that the concentration does not immediately adapt to the applied potential difference and that the concentration also depends

on the voltage input in the past. This is the memory element present in the channel, which is associated with memristors.

The best fit for the timestep τ, where the analytic model is fitted against the numerical data, is $\tau \approx 2.2$ ms, which is almost the same as the timestep that was derived analytically in Eq. (4.37).
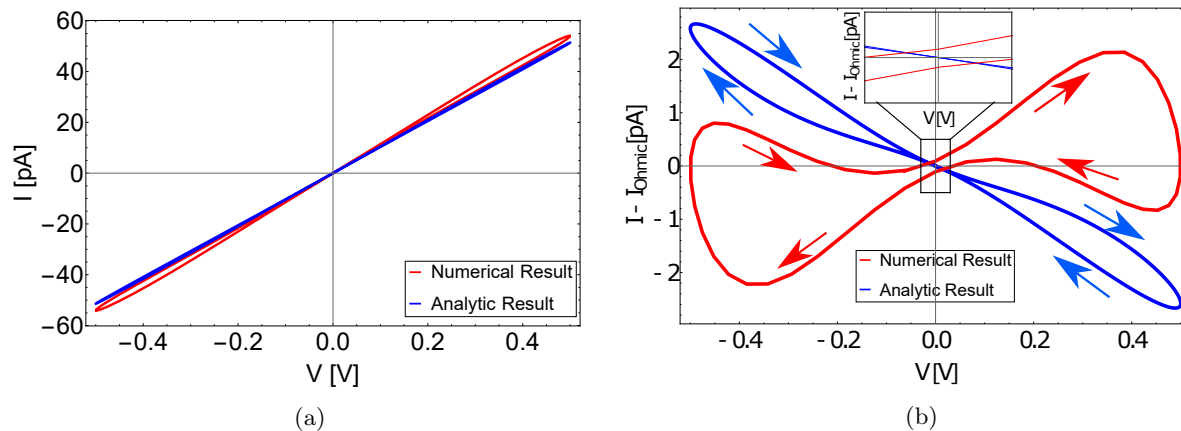

(a) (b)

Figure 21: (a) Total current I and (b) non-Ohmic current $I - I_{\text{Ohmic}}$ responses, plotted against periodic potential difference $V(t) = V_0 \sin[2\pi f t]$ with frequency $f = 75$ Hz for a channel with $\delta = 0.0$. Numerical and analytic results are plotted.

In Fig. 21 the current as a result of the applied periodic voltage $V(t)$ is plotted. This current is largely Ohmic; subtracting this Ohmic current gives us a clearer image of the memristive behaviour of the channel. The hysteresis loops of both the analytic and numerical result are indicative of a type-II memristor. The difference between the two loops is that the hysteresis loop of the analytic result touches itself at the pinch, whereas the hysteresis loop of the numerical results does not touch itself. This is a consequence of a capacitive element present in the channel, which induces a capacitive current.

5.2.2 Asymmetric Channel

Applying the same techniques on a system with $\delta = 0.9$ gives the following results. The constants are now

$$\alpha = -0.62 \ V^{-1}; \ \beta = 0.48 \ V^{-2}; \ \tau = 7.5 \text{ ms}.$$

The linear constant α is now larger in the absolute sense than the quadratic constant β. The linear potential difference contribution to the salt concentration now plays a part, which it did not for $\delta = 0.0$. Solving the differential equation for c_L with steady state concentration $c_{L,\infty}$ of Eq. (4.19) for $\delta = 0.9$, leads to the results in Fig. 22.

In Fig. 22 we compare the analytic results with the numerical results. We see in Fig. 22(a) that the results for the salt concentration $c_L(t)$ agree qualitatively. The concentrations of both the numerical and analytic calculations oscillate at the same frequency, namely the frequency of the applied voltage, which is half the frequency we observed for $\delta = 0.0$. This indicates that for $\delta = 0.9$ the concentration depends mostly on odd powers of voltage $V(t)$, whereas for $\delta = 0.0$ the even terms dominated. We again see that the peaks in concentration lag behind the peak values of the

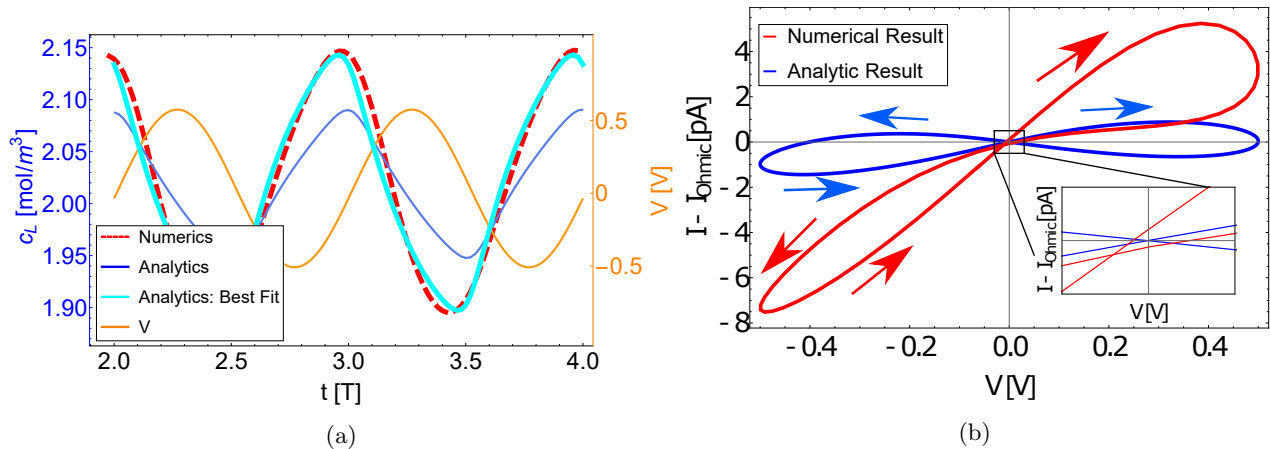(a)   (b)

Figure 22: Comparison between the numerical and analytic calculations for a channel with $\delta = 0.9$, over which a periodic potential difference $V(t) = V_0 \sin[2\pi f t]$ is applied frequency $f = 75$ Hz. In this figure (a) the laterally averaged concentration c_L is plotted against time and (b) the non-Ohmic $I - I_{\text{Ohmic}}$ current is plotted against the potential difference.

potential difference. The concentration in the channel does not immediately adapt to the applied voltage and therefore possesses a memory element.

The results are, however, not completely in quantitative agreement, as the amplitude of the concentration fluctuations is larger in the numerical case than in the analytic case, but the average concentration on the other hand is approximately the same in both cases. If we take a best of fit of the analytic result with fit parameter τ, we find almost perfect correspondence between the analytic and numerical results. The best fit of the timescale is $\tau = 3.8$ ms, which is approximately half the timescale found with the analytic theory. This indicates that the timescale found using Eq. (4.37) is not completely accurate, but it is of the same order of magnitude as the best fit τ.

In Fig 22(b) we plot the IV-hysteresis loops of the numerical and analytic results, where the linear Ohmic current contribution has been removed from both IV-loops. These loops are similar and both indicative of a type-I memristor, but there are two major difference between them. The first one is the difference in slope, which corresponds to a difference in conductivity. Looking at Fig. 22(b) this difference looks substantial, but the Ohmic current has been subtracted from both currents, which makes the difference seem larger.

The second difference is the location of the crossing. In the analytic result this crossing lies at the origin of the IV-diagram, which is the pinch in the hysteresis loop associated with memristors. In the numerical result this crossing lies in the third quadrant instead of the centre, which is a result of a capacitive element present in the system, which is not yet included in the analytic model.

5.2.3   Number of Crossings

To compare the overall behaviour of the IV-loops from the numerical and analytic results, we inspect the number of crossings over a range of values of δ. The number of crossings is indicative for the memristor-type: a type-I memristor has one crossing, a type-II memristor has zero and the intermediate type-c memristor has two. We can see in Fig. 23 that the analytic and numerical calculations follow the same general pattern as δ increases: first zero crossings, then two and finally one. The numerical results, however, lag behind the analytic results: in the analytic results there are two crossings as soon the channel becomes asymmetric, so if δ is non-zero, whereas in the

numerical results we only find two crossings from $\delta = 0.4$ onward. The switch from two crossings to one crossing also occurs at higher δ in the numerical case.
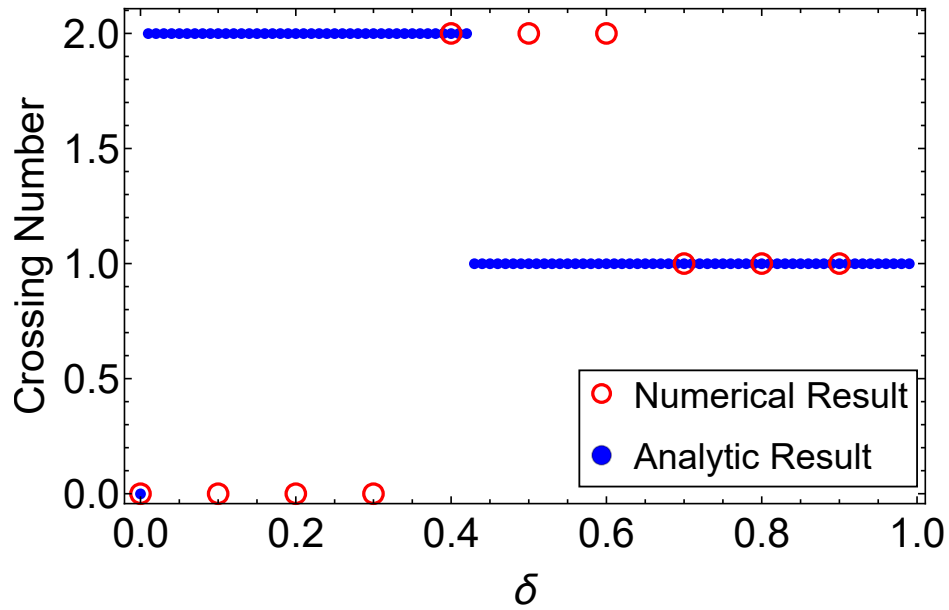

Figure 23: Number of crossings in the hysteresis loop for values of δ at a potential difference frequency of $f = 75$ Hz. The results from numerical and analytic calculations are plotted. The analytic results were generated in calculations with zero capacitance, so $\frac{C}{G_0 \tau} = 0$.

5.3   Analytic Model: Finite Capacitance

From the comparison between the analytic and numerical results in Section 5.2 we found that a capacitive element should be added to the model to mimic certain features encountered in the numerical calculations. The current in the analytic model will now be given by Eq. (4.38), which under a periodic voltage of $V(t) = V_0 \sin(\omega t)$ becomes

$$I_{tot}(t) = eD \frac{eV(t)}{2Lk_BT} \pi R_b R_t c_L(t) + C\omega \cos(\omega t).$$

Applying this model on channels with $\delta = 0.0$ and $\delta = 0.9$ with a capacitance of $C = 5.1 \cdot 10^{-18}$ F, as given by the Hall estimate of Eq. (5.7), gives the current-voltage diagrams of Fig. 24. The effect of this added capacitive element, however, is so small that it cannot be observed. In the numerical results non-zero crossing behaviour occurs when $\delta = 0.9$, as the crossing does not occur at the pinch, and if $\delta = 0.0$ we find that the two ends of the hysteresis loop do not touch at the pinch. These capacitance related effects do not noticeably appear in the analytic calculations with the Hall capacitance.
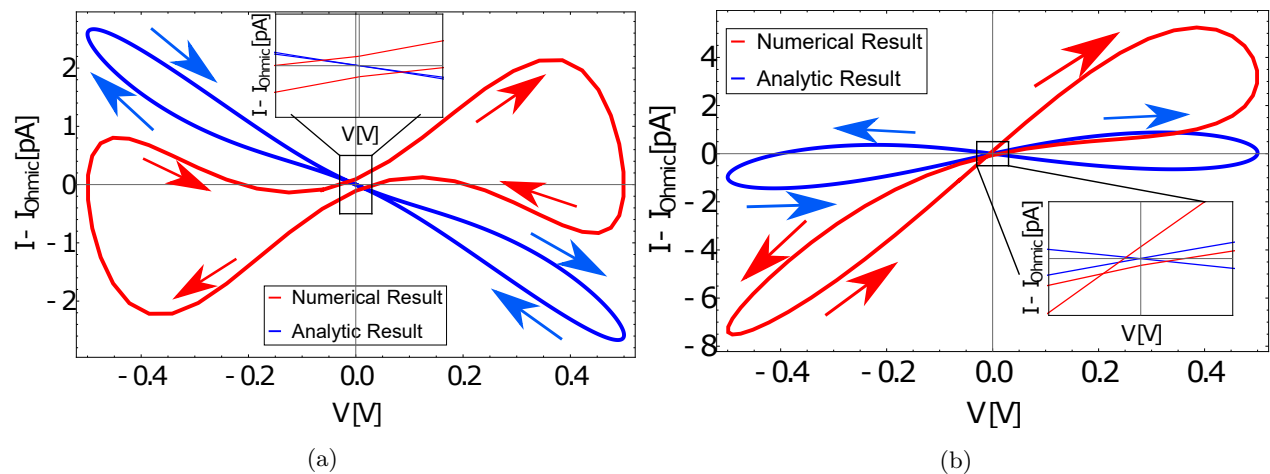

Figure 24: Comparison of the current response $I - I_{\text{Ohmic}}$ to the application of a periodic voltage $V(t) = V_0 \sin[2\pi f t]$ between the numerical and analytic calculations for a channel with (a) $\delta = 0.0$ and for a channel with (b) $\delta = 0.9$. The frequency of the applied voltage is $f = 75$ Hz. The analytic calculations include capacitive element of C_{Hall} as given in Eq. (5.7).

When we compare the number of crossings for IV-loops from numerical calculations and from analytic calculations with the Hall capacitance estimate, we find that the Hall-capacitance has very little influence on the crossing behaviour. In Fig. 25 we find very similar crossing behaviour as we did in Fig. 23. To find a better predictor of the crossing behaviour, a larger capacitance must be implemented.
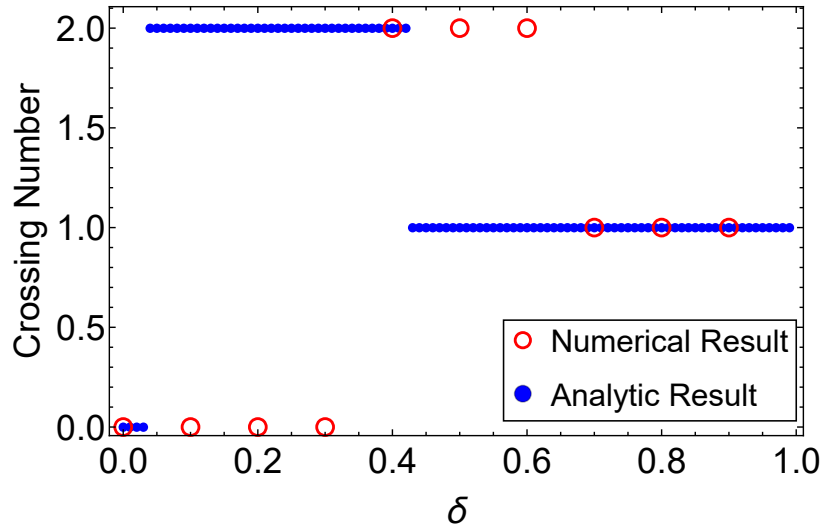
Figure 25: Number of crossings in the hysteresis loop for a range of values of δ at a potential difference frequency of $f = 75$ Hz. The results from numerical and analytic calculations are plotted. The analytic results are performed with the Hall estimate capacitance of Eq. (5.7).

If we instead take the capacitance estimate $C = 5.4 \cdot 10^{-16}$ F, amounting to a dimensionless capacitance of $\frac{C}{G_0\tau} = 0.002$ with $\tau = 5$ ms, and implement it in the analytic model, we get the results in Fig. 26, that we compare to results from numerical FE-calculations. The capacitive effect now has a noticeable effect, as some features of the hysteresis loops from the numerical results are reproduced. In Fig. 26(a) the hysteresis loop does not touch itself at the origin, which is also the case in the numerical calculation. For a channel with $\delta = 0.9$ the pinch of the analytic hysteresis loop in Fig. 26(b) does not lie at the origin anymore, but in the third quadrant of the IV-diagram, similar to what occurs in the numerical result.
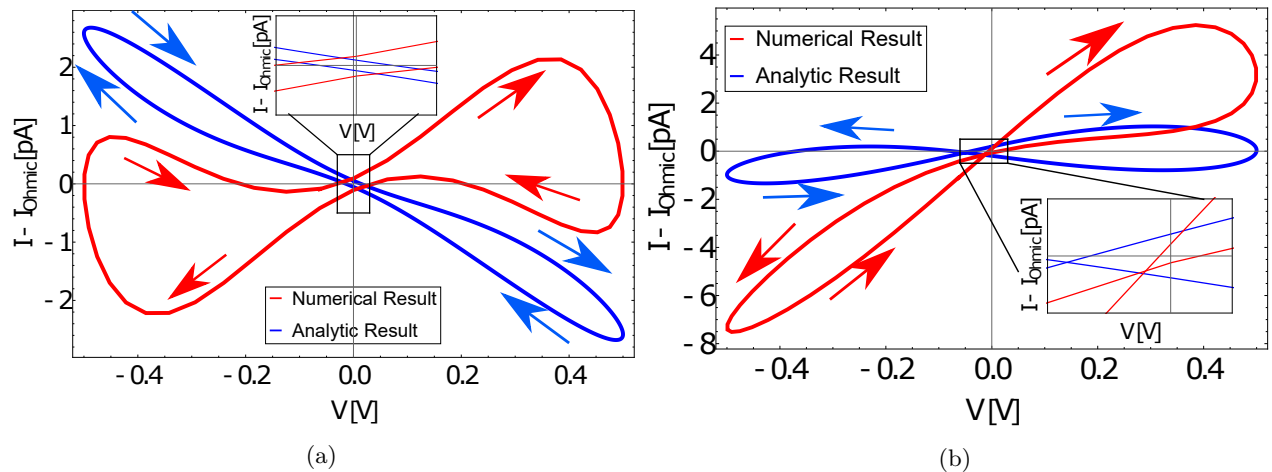

Figure 26: Comparison of the current response $I - I_{\mathrm{Ohmic}}$ to the application of a periodic voltage $V(t) = V_0\sin[2\pi ft]$ between the numerical and analytic calculations for a channel with (a) $\delta = 0.0$ and for a channel with (b) $\delta = 0.9$. The frequency of the applied voltage is $f = 75$ Hz. The analytic calculations include a capacitive element of $C = 5.4 \cdot 10^{-16}$ F, equivalent to $\frac{C}{G_0\tau} = 0.002$.

The crossing behaviour associated with this capacitance is given in Fig. 27. It follows a pattern that is closer to the numerical results, than the zero-capacitance result plotted in Fig. 23. There is a region with low values of δ in which there are 0 crossings in the hysteresis loop, as is also the case for the numerical result, whereas in Fig. 23 the hysteresis loop already gained two crossings as δ became non-zero. The switch from 2 crossings to 1 crossing also occurs later as a result of the capacitive element in the system and is closer to the switch observed in the numerical calculations. However, the pattern is not completely in agreement with the numerical calculations: the switch from 2 crossings to 1 crossing occurs at higher values for the numerical results (at around $\delta = 0.7$) than for the analytic results (at around $\delta = 0.5$). All things considered, adding a capacitive element to the analytic model improves its mimicking power significantly.
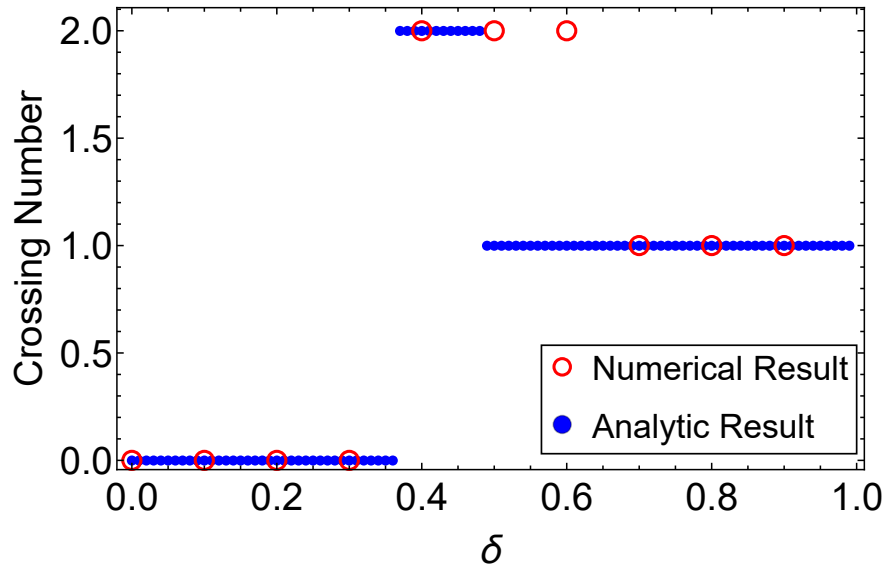

Figure 27: Number of crossings in the hysteresis loop for a range of values of δ at a potential difference frequency of $f = 75$ Hz. The results from numerical and analytic calculations are plotted. The analytic results are performed with a capacitive element of $C = 5.4 \cdot 10^{-16}$ F, equivalent to $\frac{C}{G_0 \tau} = 0.002$.

5.4   State Diagrams: Frequency and Geometry

Up until now we have only inspected the crossing behaviour of the hysteresis loops at a frequency of $f = 75$ Hz, but frequency has an important role in the memristive behaviour, as we already encountered in Section 5.1.1. To give a full indication of the efficacy of the analytic model, we construct a state diagram where the number of crossings indicates the type of memristor. We can identify the type of memristive system for a certain configuration of parameters using the number of crossings of the hysteresis loop in the current-voltage diagram. We differentiate between three types of memristors: type-I memristors, type-II memristors and type-c memristors, which have hysteresis loops with one, zero and two crossings, respectively.

The state diagram is shown in Fig. 28, in which the memristive behaviour for the analytic model with no capacitance is plotted, together with the memristive behaviour from FE-calculations. The results from FE-calculations are plotted in this figure as individual circles, the analytic results are the hues in the background.
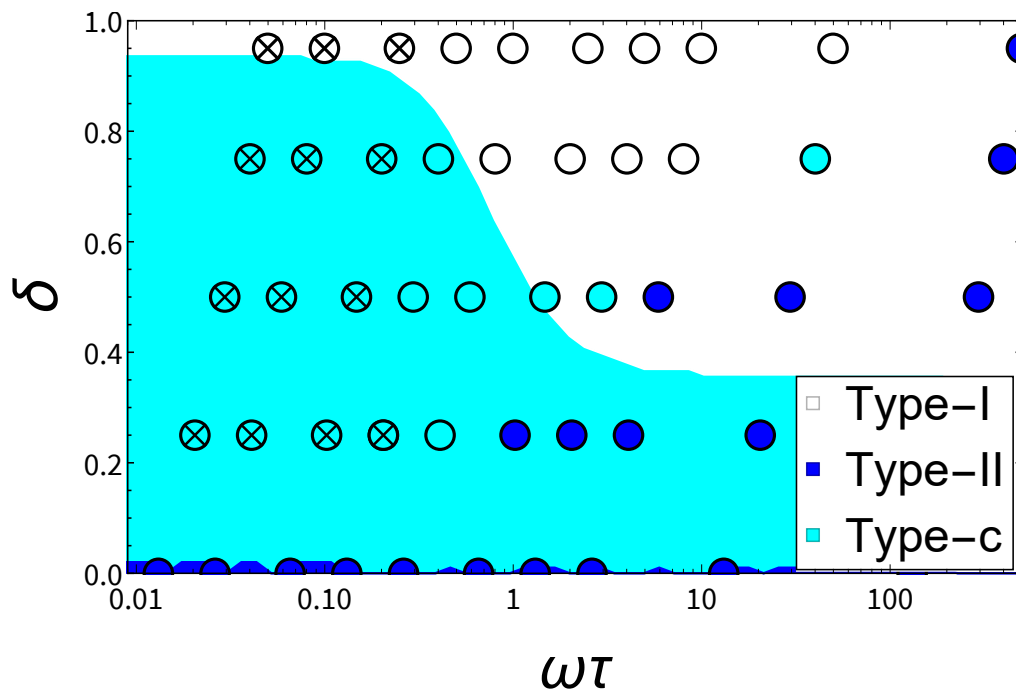
Figure 28: Diagram of memristor-types for various geometries, given by δ, and various dimensionless potential difference frequencies $\omega\tau$. Results from finite-element calculations, as indicated by the coloured dots, are compared to results from the analytic model, indicated by the hues in the background. The analytic model contains no capacitive element, so $\frac{C}{G_0\tau} = 0$. The crossed dots are discussed in Appendix D.

The analytic model has some areas in which it accurately mimics the memristor-type from the FE-calculations, such as in the areas with low $\omega\tau$, where the memristor-type results from FE-simulations overlap with the results from the analytic model. The model predicts the observed change from type-c memristive behaviour to type-I memristive behaviour for larger values of δ as the frequency increases.

However, at higher frequencies the predictions becomes less accurate, as the model largely fails to predict the type-II memristive behaviour that occurs at low δ. It only accurately predicts that this

behaviour occurs at $\delta = 0.0$, but not that it also occurs for higher values of δ if the frequency $\omega\tau$ is large. Type-II memristive crossing behaviour for a large part depends on a capacitive element present in the system. Another issue with the model is that it does not predict the extra crossings that are observed at lower frequencies $\omega\tau$ in the FE-calculations. These extra crossings observed in FE-calculations are denoted by a cross through the coloured dots. In Appendix D this feature of the hysteresis loops is discussed in more detail.

In Fig. 29 a state diagram of the hysteresis behaviour is shown for the case that a capacitive element is included in the model and it is clear that the analytic model now more accurately mimics the results found through finite-element calculations. The analytic model predicts type-II behaviour for low values of δ over the entire range of frequencies, as well as the type-II crossing behaviour at high frequencies $\omega\tau$, which we both also find in the FE-calculations. Only at large values of δ and large frequencies the model fails to mimic the FE-behaviour, with the analytic model predicting type-II behaviour and the FE-calculations indicating type-I behaviour. This is a result of the capacitive element being too dominant in this range; the contribution of the capacitive element to the total current increases with the frequency, such that at large frequencies we only encounter non-crossing behaviour. The current response of a capacitor to a periodic voltage is non-crossing, hence a dominant capacitor will lead to non-crossing behaviour.
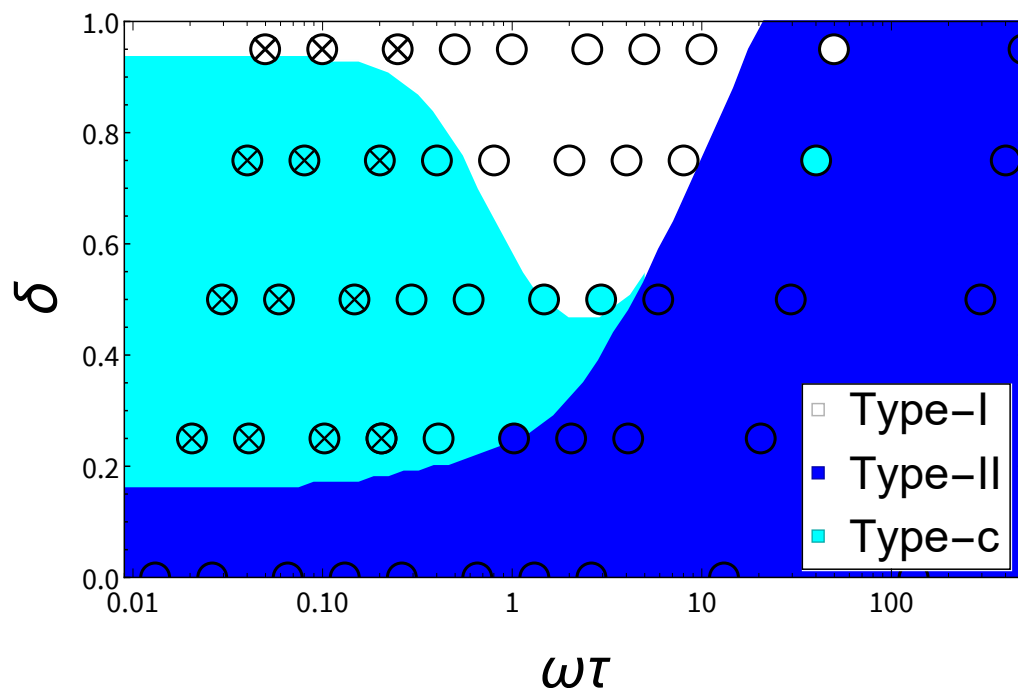

Figure 29: Diagram of memristor-types for various geometries, given by δ, and various dimensionless potential difference frequencies $\omega\tau$. Results from finite-element calculations, as indicated by the coloured dots, are compared to results from the analytic model, indicated by the hues in the background. The analytic model contains a capacitive element, with a magnitude of $\frac{C}{G_0\tau} = 0.002$.

5.5   Hysteresis Area

In Eq. (5.3) we introduced a parameter $\hat{S}_1$, which indicates the size of the area enclosed by one half of the hysteresis loop in an IV-diagram. In Fig. 15(a) it was shown that this area is different for various values of δ and at various potentential difference frequencies f. In Fig. 30 we compare the results from the analytic model to the results from finite-element calculations. The results from Fig. 15(a), in which $\hat{S}_1$ was given as a function of frequency f, was adapted to Fig. 30(a) by changing f into $\omega\tau = 2\pi f \tau$, where we take the timescale τ from Eq. (4.37).
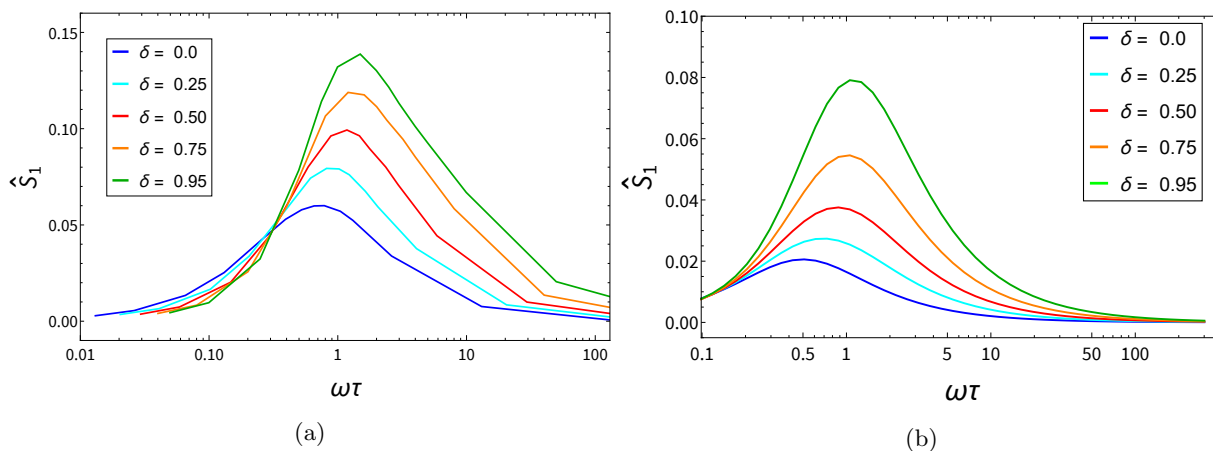

Figure 30: The area $\hat{S}_1$, as defined in Eq. (5.3) over a range of dimensionless frequencies $\omega\tau$, for various values of geometry parameter δ. In this figure we show (a) results from finite-element calculations and (b) results from the analytic model. The analytic results were generated in calculations with zero capacitance, so $\frac{C}{G_0\tau} = 0$. Here $\hat{S}_1 = 1$ corresponds to $S_1 = 1.3$ pW.

The analytic model and the FE-calculations are in qualitative agreement with each other. For both results the total hysteresis area increases as δ increases and the peak of this hysteresis area is around $\omega\tau = 1.0$ in both cases, with the frequency of this peak value increasing slightly when δ becomes larger. The values of $\hat{S}_1$ in both results are of the same order, but they are in general twice as large in the FE-calculations as in the results from the analytic model.

In Fig. 31 a comparison is made of between the area $\hat{S}$ for the hysteresis loops of the analytic calculations and $\hat{S}$ for the FE-calculations loops, with $\hat{S}$ introduced in Eq. (5.2). We can see that $\hat{S}$ in general decreases as δ becomes greater, which is a consequence of the crossing behaviour changing from type-II behaviour to type-I behaviour as δ increases; the negative contribution to $\hat{S}$, associated with the crossings present in type-c and type-I memristive loops, increases in this case. We also find that in the analytic result $\hat{S}$ becomes negative for large values of δ, indicating that the hysteresis loop lobe in the third quadrant has a larger area than the lobe in the first quadrant, which does not occur in the FE-results.
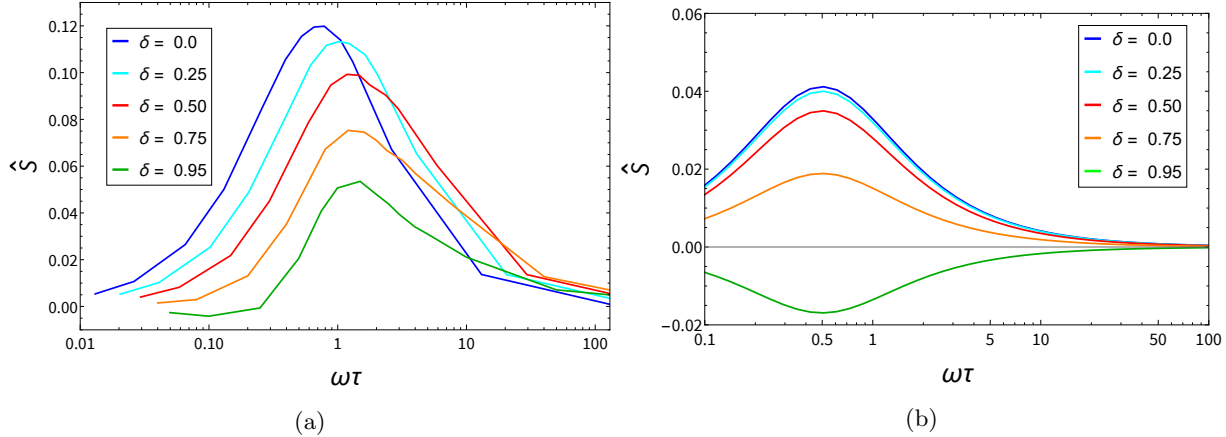
Figure 31: The area $\hat{S}$, as defined in Eq. (5.2) over a range of dimensionless potential difference frequencies $\omega\tau$, for various values of geometry parameter δ. In this figure we show (a) results from finite-element calculations and (b) results from the analytic model. The analytic results were generated in calculations with zero capacitance, so $\frac{C}{G_0\tau} = 0$. Here $\hat{S} = 1$ corresponds to $S = 1.3$ pW.

In the analytic result, plotted in Fig. 31(b), we observe that the peak value of $\hat{S}$ occurs at the same frequency of around $\omega\tau = 0.5$ for all values of δ, except for $\delta = 0.95$, because it has its lowest value at $\omega\tau = 0.5$. This is not the case for the FE-calculations; the frequency of the peak value increases with δ, although it is constant from $\delta = 0.5$ on. This is possibly related to the expression for τ from Eq. (4.37) not being accurate enough, which means that the frequencies $\omega\tau$ are not accurate as well in the FE-calculations.

5.6   General Model

We analysed the hysteresis loop crossing behaviour of ionic nanopores, which possess memristive properties. It is possible to apply the same analysis to the general memristive model, as described in Eq. (3.1), Eq. (3.3) and Eq. (3.5). These equations describe a system's changing conductivity, the steady state conductivity of a specific system and the current through this general memristor, in that order. This is described by these equations:

$$g_\infty [V] = g_0 \left(1 + \alpha V + \beta V^2\right) \tag{5.9}$$

$$\tau \partial_t g(t) = g_\infty [V(t)] - g(t) \tag{5.10}$$

$$I(t) = g(t)V(t) + C\frac{\partial V(t)}{\partial t}, \tag{5.11}$$

where $g(t)$ indicates the conductivity of the memristor, $g_\infty [V]$ its steady state conductivity, of which we now only consider its first three expansion terms, and the factor τ is a characteristic timescale of the system. We can solve these first two equations numerically under a periodic potential difference $V = V_0 \sin [\omega t]$. In this voltage expression we have $\omega = 2\pi f$, with f the frequency of the periodic potential difference. As in the nanochannel model, we model the capacitive element of the memristor with a capacitor, as done in Fig 4, with C the capacitance of this capacitor.

To generalise this model, we make that it depends on a series of dimensionless parameters. To determine on which dimensionless parameters this model depends, we can perform a *Buckingham-π* analysis, in which we condense the parameters present in our model to a smaller number of essential dimensionless parameters. The parameters and their fundamental SI-units are given in Tab. 2.

Parameter	Fundamental Units
g_0	$A^2 \ s^3 \ kg^{-1} \ m^{-2}$
α	$A^1 \ s^3 \ kg^{-1} \ m^{-2}$
β	$A^2 \ s^6 \ kg^{-2} \ m^{-4}$
C	$A^2 \ s^4 \ kg^{-1} \ m^{-2}$
V_0	$A^{-1} \ s^{-3} \ kg^1 \ m^2$
ω	s^{-1}
τ	s^1

Table 2: Parameters of the general model, as described in Eq. (5.9), Eq. (5.10) and Eq. (5.11), with their respective fundamental units.

To find the relevant dimensionless parameters we form the dimensional matrix of the parameters in Tab. 2. In this dimensional matrix the rows correspond to the fundamental dimensions of the parameters and the columns correspond to the parameters themselves, which results in the matrix as given in Tab. 3.

$$M = \begin{array}{c|ccccccc} & g_0 & \alpha & \beta & C & V_0 & \omega & \tau \\ \hline A & 2 & 1 & 2 & 2 & -1 & 0 & 0 \\ s & 3 & 3 & 6 & 4 & -3 & -1 & 1 \\ kg & -1 & -1 & -2 & -2 & 1 & 0 & 0 \\ m & -2 & -2 & -4 & -1 & 2 & 0 & 0 \end{array}$$

Table 3: Dimensional matrix of the parameters in the general model.

In the dimensional matrix in Tab. 3 the units of a parameter are positioned in a single column, so the unit of the zero-potential conductivity, $[g_0] = A^2 \ s^3 \ kg^{-1} \ m^{-2}$, is given by the vector $(2, 3, -1, -2)^T$.

The dimensionless parameters can be obtained by finding the subspace of vectors $\boldsymbol{a}$ that obey $\boldsymbol{Ma} = \boldsymbol{0}$; when the vector is multiplied with the dimensional matrix, it results in a null-vector. This vector subspace for the matrix in Tab. 3, which is called its nullspace, is given in Eq. (5.12)

$$\boldsymbol{a}_1 = \begin{pmatrix} 0 \\ 1 \\ 0 \\ 0 \\ 1 \\ 0 \\ 0 \end{pmatrix}, \ \boldsymbol{a}_2 = \begin{pmatrix} 1 \\ 0 \\ 0 \\ -1 \\ 0 \\ 0 \\ 1 \end{pmatrix}, \ \boldsymbol{a}_3 = \begin{pmatrix} -1 \\ 0 \\ 0 \\ 1 \\ 0 \\ 1 \\ 0 \end{pmatrix}, \ \boldsymbol{a}_4 = \begin{pmatrix} 0 \\ -2 \\ 1 \\ 0 \\ 0 \\ 0 \\ 0 \end{pmatrix}. \tag{5.12}$$

The nullspace-vectors in Eq. (5.12) indicate what the relevant dimensionless parameters are for the memristor-capacitor model. Each value in the vector corresponds to the order to which a parameter, as given in the top row of Tab. 3, is present in a dimensionless parameter. For example, vector $\boldsymbol{\alpha}_1$ has a non-zero value of 1 in its second and fifth row, corresponding to the parameters α and V_0, respectively, and thus the dimensionless parameter of vector $\boldsymbol{\alpha}_1$ is $\alpha^1 V_0^1$. All dimensionless parameters are given in Eq. (5.13)

$$d_1 = \alpha V_0, \ d_2 = \frac{g_0 \tau}{C}, \ d_3 = \frac{C\omega}{g_0}, \ d_4 = \frac{\beta}{\alpha^2}. \tag{5.13}$$

The dimensionless parameter d_1 indicates the ratio between the potential difference amplitude V_0 and the linear potential difference response of the memristor-conductivity, indicated by α. The parameters d_2 and d_3 give the ratio between the RC-time $\frac{C}{g_0}$ of the system and the timescale τ and frequency ω, respectively. For convenience we also introduce parameter

$$d_5 = d_2 d_3 = \omega\tau,$$

indicating the ratio between the potential difference frequency and the system's timescale. Because for a particular system τ is predetermined, a change in d_5 indicates a change in the frequency of the voltage. The parameter d_3 can in turn be used to indicate the strength of the capacitive effect in the memristor.

The parameter d_4 shows the ratio between the linear and quadratic potential difference dependence of the conductivity of the memristor. The factors α and β in d_4 are used in the expression of the memristor conductivity g_∞ in Eq. (5.9).

For a given capacitance we can make a state diagram of the type of memristor we find for a certain configuration of parameters, which we do for a system with zero capacitance in Fig. 32. This state diagram is symmetric in the x-axis; we find the same type of memristor at positive values of $\frac{\alpha^2}{\beta}$ as we find at negative values of equal size. Only at $\frac{\alpha^2}{\beta} = 0$ do we find type-II memristors, since when $\frac{\alpha^2}{\beta}$ becomes non-zero, we find type-c memristors and at even higher absolute values of $\frac{\alpha^2}{\beta}$ we encounter type-I memristors. As we increase the driving frequency of the potential difference, given by the dimensionless $\omega\tau$, a change from type-c to type-I memristors occurs for some values of $\frac{\alpha^2}{\beta}$.

Adding a capacitance to the model changes the crossing behaviour, as is shown in Fig. 33. For low frequencies the crossing behaviour is almost identical to the capacitance-free model. At higher frequencies we find that the capacitance becomes more dominant, which results in non-crossing hysteresis loops. The sign of the parameter $\frac{\alpha^2}{\beta}$ now has an influence on the crossing behaviour, which it did not in the capacitance-free model of Fig. 32. We find, for example, that at high frequencies we encounter type-I memristors for certain positive values of $\frac{\alpha^2}{\beta}$, while we find type-II memristors for negative values of $\frac{\alpha^2}{\beta}$ of the same magnitude.
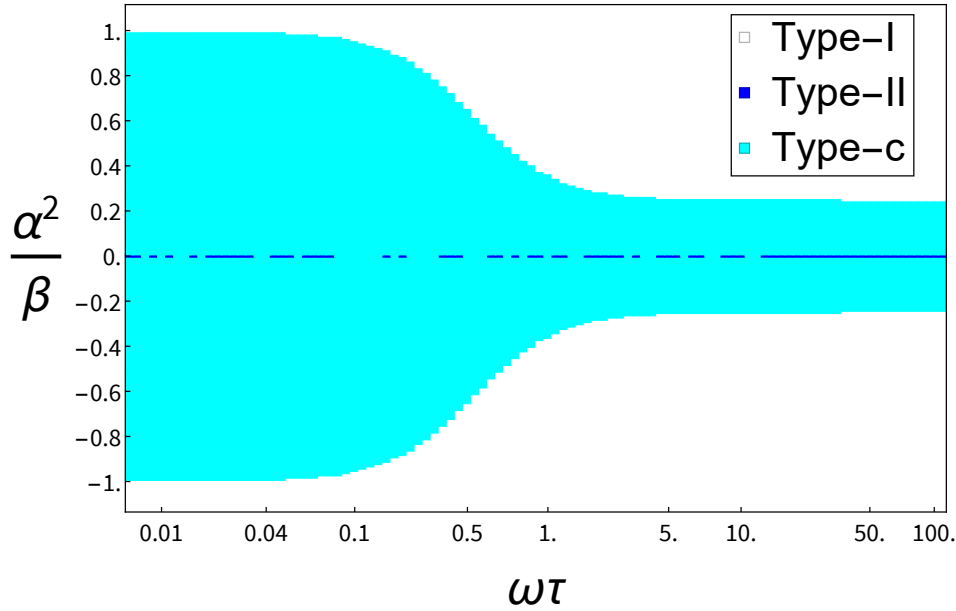
Figure 32: State diagram of memristor-types for the general memristor model with a dimensionless capacitance of $\frac{C\omega}{g_0} = 0.0$. The memristor-type for varying $\frac{\alpha^2}{\beta}$ and frequencies $\omega\tau$ is shown.
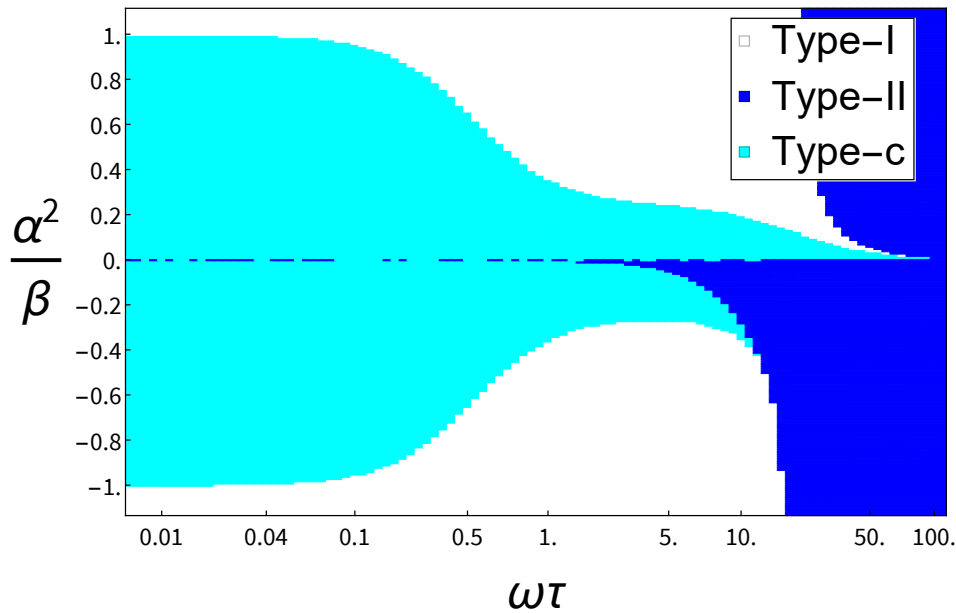

Figure 33: State diagram of memristor-types for the general memristor model with a dimensionless capacitance of $\frac{C\omega}{g_0} = 0.001$. The memristor-type for varying $\frac{\alpha^2}{\beta}$ and frequencies $\omega\tau$ is shown.

The lower half of Fig. 29 strongly reflects the results from the memristor state diagram for the ionic channel, given in Fig. 29, although the diagram results are vertically mirrored. This is to be expected, as β is negative for most values of δ for the ionic channel, which results in a negative value of $\frac{\alpha^2}{\beta}$. In an ionic channel α^2 increases with δ, thus an increase in δ can be associated with an decrease in the factor $\frac{\alpha^2}{\beta}$, if the factor $\frac{\alpha^2}{\beta}$ is negative.

6   Discussion

For this master thesis research project we set out to develop a model that is able to mimic the hysteresis behaviour of volatile memristive systems that contain a capacitive element. The model we developed was based on a simple Ansatz and a simple expansion of the conductivity of the memristor, in powers of the applied potential difference V. We tested this model on an ionic nanopore, which is a realisation of a volatile memristor.

In Section 4.2 an expression for the conductivity of the ionic nanopores was derived analytically, which required a large number of assumptions to be made that did not always reflect the physical situation in the channel. For example, we assumed that the salt concentration does not depend on the radial coordinate r of the channel, which neglects the effect of the EDL, and the entrance effects of the channel were completely neglected. Despite these approximations, the derived expressions are fairly accurate in mimicking the voltage-response of the concentration profiles in channels with various geometries. Although the change in concentration as a result of an applied voltage, is underestimated, the processes that govern the behaviour are included in the expressions, which is surprising considering the number of assumptions made in deriving them. The differences between the analytic equations and the FE-calculations are probably a result of these approximations.

Much attention in this thesis was given to the crossing behaviour of memristor hysteresis loops, with most attention being given to their number of crossings. The model was fairly accurate in reproducing the number of crossings encountered in FE-calculations on nanopore systems. Comparing the model to the nanopore FE-calculations revealed the large role that the capacitive element of a memristive system plays in determining the number of crossings. Type-II behaviour, in which the loop does not cross itself, is associated with symmetric systems and correspondingly, in analytic calculations with zero capacitance this behaviour was only found for completely symmetric systems, for which $\delta = 0.0$; any asymmetry would result in two crossings in the hysteresis loop. However, in the FE-calculations we encountered zero-crossing behaviour for asymmetric systems with non-zero values of δ.
Implementing a very minor capacitive element in the model allowed us to more accurately reproduce the results from FE-calculations; type-II memristive behaviour now was observed for non-zero values of δ in the analytic model as well. Compared to the conductive element of the memristive system, the capacitive element is small. Nevertheless, it has an important influence on the hysteresis behaviour, as a very minor capacitance protects type-II crossing behaviour from turning into type-c and type-I behaviour if asymmetry is introduced into a memristive system. When studying the crossing behaviour of physical systems, one should not neglect this capacitance.

Although the capacitive element required to accurately mimic the finite-element memristive crossing behaviour was small, it was larger than the capacitance we expected to find in a nanopore, as predicted by Hall [57]. There are multiple causes for the discrepancy between the Hall-estimate and the capacitance, which was eventually implemented. The first one is that we might have underestimated the specific resistivity of the electrolyte, which in turn decreases the capacitance of the Hall-estimate. The second option is that the geometry causes an increase in the capacitance of the pore. The narrowing of the pore might lead to more charge building up, than one would expect in a cylindrical nanopore. However, we also found that changing the channel geometry, through changing the factor δ, has little effect on the capacitance of a channel. It is therefore not likely that this is the cause of the discrepancy
The model also failed to predict the larger number of crossings in the hysteresis loops, observed in

FE-calculations at low frequencies, which we discus in Appendix D. The reason for this discrepancy probably lies in the fact that the Ansatz, which describes how the conductivity in the channel changes under the application of a time dependent voltage, is not accurate enough. There might be a second, more complex process, not described by the Ansatz, that also plays a part in determining the channel's changing conductivity. This process must have a larger timescale than the one described through the Ansatz, as the effect of this process only becomes clear at low frequencies.

A difficulty encountered in adapting the ionic nanochannel to the analytic model was generating an appropriate timescale τ to use in the model. The timescale we generated, as given in Eq. (4.37), depended on the total ion-number in a single cone of the channel, even though the conductivity of the channel depends on the laterally averaged salt concentration in the entire channel. Generating a timescale based on these last properties gave some difficulties, even though the timescale we found seems to possess some general characteristics of the actual timescale of the system. The best-fit timescales are of the same order as the analytically derived timescale and both the best-fit and analytic timescale increase as δ increases. However, at large values of δ the two timescales diverge, as, to give an illustration, at $\delta = 0.95$ the analytic timescale is twice as large as the best-fit timescale. The inaccurate timescale leads to some problems in comparing results from FE-calculations and analytic calculations. When comparing the area S between these two calculations, as we did in Section 5.5, we converted the frequencies f for the FE-calculations to dimensionless frequencies $\omega\tau$, by multiplying f by timescale $2\pi\tau$. This might explain the discrepancy between numerics and analytics we encountered in this section, which concerned the frequency at which the maximum value of S was found.

From the analytic results of Fig. 31(b) we find the peak value of S is reached at at a standard frequency $\omega\tau_{\mathrm{max}}$. This would indicate that the dimensionless $\omega\tau$ is the relevant frequency parameter for predicting hysteresis behaviour of memristors, which is supported by its presence in the set of relevant dimensionless parameters we found through Buckingham-π analysis. One could use this property to determine the timescale τ of a specific system, by determining the frequency f_{max} at which the area S is maximal. Using this method a fundamental property of a memristor can be extracted through experiments.

A mathematical analysis of the hysteresis crossing behaviour is necessary to determine how this maximum area frequency $\omega\tau_{\mathrm{max}}$ arises. There are still some open questions regarding this frequency, such as why it occurs at $\omega\tau = 0.5$ and why the maximum area is the same for all geometries. This analysis can limit itself to a simple expression of g_∞, as given in Eq. (2.15).

We strongly encourage experimental research to be performed on the memristive behaviour of the pores described in this thesis. Although some experiments have been performed on the memristive behaviour of nanopores, very little attention has been given to the effect of changing the geometry of the channels; most research has been focused on conical nanopores [42, 44]. Attention was given to the effect of changing the voltage scanning rate, equivalent to the frequency, but the frequencies at which the experiments were performed did not cover the range of frequencies studied in this thesis. These experiments were performed at relatively low frequencies and crossing behaviour besides type-I behaviour was not observed in these experiments on nanopores. However, non-zero crossing behaviour, an effect of capacitance in the system, was observed.

The hourglass-shaped pores should be relatively simple to construct. Experiments on this symmetric channel alone and comparing it to experiments on conical nanopores should give new insights into the effect of system symmetry on memristive behaviour. We also expect to observe the effect of the capacitive element more clearly, as this is easier to observe in type-II memristors than type-I memristors.

7   Conclusion

In this thesis we have developed an analytic model for volatile memristors that possess a capacitive element. This model was used to mimic the memristive behaviour of ionic nanopores which connect two electrolyte reservoirs, as a periodic voltage is applied over the pore-system.

We found that the conductivity of the pores largely depends on their salt concentration, which is affected by the potential difference applied over the channel. The channel possesses the memory-characteristic of a memristor, due to the concentration not immediately adapting to the changing voltage. Determining the salt concentration progression in time allowed us to mimic the memristive properties of the pore.

Our analysis showed that the geometry of the memristive system strongly determines its type of hysteresis behaviour. A symmetric system exhibits non-crossing type-II memristive behaviour, whereas an asymmetric system in general exhibits single crossing type-I behaviour or double crossing type-c behaviour, in the case of slight deviations from the symmetric geometry. However, type-II behaviour can also be encountered in systems that slightly deviate from a symmetric geometry, as a result of a minor capacitive element in the system. The frequency of the potential difference also has an influence on the crossing behaviour, with type-II memristors becoming more prevalent at higher frequencies, as the capacitive element becomes more dominant.

The total area enclosed by the memristor hysteresis loop depends on both the voltage frequency and the geometry of the memristor. There are indications that the maximum enclosed area is found at a set dimensionless frequency $\omega\tau_{\mathrm{max}}$, with τ the characteristic timescale of a system.

Further research on memristors is necessary to gain more insight into their hysteresis behaviour. A thorough mathematical analysis of crossing behaviour and the area enclosed by hysteresis loops is therefore encouraged. We also recommend for more experimental research into the memristive properties of ionic nanopores to be performed, which would allow for further testing of the memristor model developed in this thesis.

References

[1] L. Chua. "Memristor-The missing circuit element". In: *IEEE Transactions on Circuit Theory* 18.5 (1971), pp. 507–519. DOI: 10.1109/TCT.1971.1083337.

[2] L. Chua and S. M. Kang. "Memristive devices and systems". In: *Proceedings of the IEEE* 64.2 (1976), pp. 209–223. DOI: 10.1109/PROC.1976.10092.

[3] J. P. Carbajal and F. Caravelli. "Memristors for the curious outsiders". In: (Sept. 2018). DOI: 10.31224/osf.io/c4qr9. URL: https://doi.org/10.31224/osf.io/c4qr9.

[4] V. Francis. *Fundamentals of Discharge Tube Circuits*. Methuen's monographs on physical subjects. Methuen, 1948. URL: https://books.google.nl/books?id=LNDOAAAAIAAJ.

[5] F. Argall. "Switching phenomena in titanium oxide thin films". In: *Solid-State Electronics* 11.5 (May 1968), pp. 535–541. DOI: 10.1016/0038-1101(68)90092-0. URL: https://doi.org/10.1016/0038-1101(68)90092-0.

[6] L. Chua. "If it's pinched it's a memristor". In: *Semiconductor Science and Technology* 29.10 (Sept. 2014), p. 104001. DOI: 10.1088/0268-1242/29/10/104001. URL: https://doi.org/10.1088/0268-1242/29/10/104001.

[7] L. Chua. "Memristor, Hodgkin–Huxley, and Edge of Chaos". In: *Nanotechnology* 24.38 (Sept. 2013), p. 383001. DOI: 10.1088/0957-4484/24/38/383001. URL: https://doi.org/10.1088/0957-4484/24/38/383001.

[8] D. B. Strukov, G. S. Snider, D. R. Stewart, and R. S. Williams. "The missing memristor found". In: *Nature* 453.7191 (May 2008), pp. 80–83. DOI: 10.1038/nature06932. URL: https://doi.org/10.1038/nature06932.

[9] J. J. Yang, M. D. Pickett, X. Li, D. A. A. Ohlberg, D. R. Stewart, and R. S. Williams. "Memristive switching mechanism for metal/oxide/metal nanodevices". In: *Nature Nanotechnology* 3.7 (June 2008), pp. 429–433. DOI: 10.1038/nnano.2008.160. URL: https://doi.org/10.1038/nnano.2008.160.

[10] E. Gale. "TiO_2-based Memristors and ReRAM: Materials, Mechanisms and Models (a Review)". In: *Semiconductor Science and Technology* 29.10 (Sept. 2014), p. 104004. DOI: 10.1088/0268-1242/29/10/104004. URL: https://doi.org/10.1088/0268-1242/29/10/104004.

[11] Y. V. Pershin and M. D. Ventra. "Memory effects in complex materials and nanoscale systems". In: *Advances in Physics* 60.2 (Apr. 2011), pp. 145–227. DOI: 10.1080/00018732.2010.544961. URL: https://doi.org/10.1080/00018732.2010.544961.

[12] I. Boybat et al. "Neuromorphic computing with multi-memristive synapses". In: *Nature Communications* 9.1 (June 2018). DOI: 10.1038/s41467-018-04933-y. URL: https://doi.org/10.1038/s41467-018-04933-y.

[13] R. Wang et al. "Recent Advances of Volatile Memristors: Devices, Mechanisms, and Applications". In: *Advanced Intelligent Systems* 2.9 (July 2020), p. 2000055. DOI: 10.1002/aisy.202000055. URL: https://doi.org/10.1002/aisy.202000055.

[14] D. V. Christensen et al. "2022 roadmap on neuromorphic computing and engineering". In: *Neuromorphic Computing and Engineering* 2.2 (May 2022), p. 022501. DOI: 10.1088/2634-4386/ac4a83. URL: https://doi.org/10.1088/2634-4386/ac4a83.

[15]   E. Chicca and G. Indiveri. "A recipe for creating ideal hybrid memristive-CMOS neuromorphic processing systems". In: *Applied Physics Letters* 116.12 (Mar. 2020), p. 120501. DOI: `10.1063/1.5142089`. URL: `https://doi.org/10.1063/1.5142089`.

[16]   V. K. Sangwan and M. C. Hersam. "Neuromorphic nanoelectronic materials". In: *Nature Nanotechnology* 15.7 (Mar. 2020), pp. 517–528. DOI: `10.1038/s41565-020-0647-z`. URL: `https://doi.org/10.1038/s41565-020-0647-z`.

[17]   L. Chua, V. Sbitnet, and H. Kim. "Hodgkin-Huxley axon is made of memristors". In: *International Journal of Bifurcation and Chaos* 22.03 (2012), p. 1230011. DOI: `10.1142/S021812741230011X`. URL: `https://doi.org/10.1142/S021812741230011X`.

[18]   A. L. Hodgkin and A. F. Huxley. "A quantitative description of membrane current and its application to conduction and excitation in nerve". In: *The Journal of Physiology* 117.4 (Aug. 1952), pp. 500–544. DOI: `10.1113/jphysiol.1952.sp004764`. URL: `https://doi.org/10.1113/jphysiol.1952.sp004764`.

[19]   M. P. Sah, H. Kim, and L. O. Chua. "Brains Are Made of Memristors". In: *IEEE Circuits and Systems Magazine* 14.1 (2014), pp. 12–36. DOI: `10.1109/mcas.2013.2296414`. URL: `https://doi.org/10.1109/mcas.2013.2296414`.

[20]   P. Robin, N. Kavokine, and L. Bocquet. "Modeling of emergent memory and voltage spiking in ionic transport through angstrom-scale slits". In: *Science* 373.6555 (Aug. 2021), pp. 687–691. DOI: `10.1126/science.abf7923`. URL: `https://doi.org/10.1126/science.abf7923`.

[21]   T. Dudev and C. Lim. "Factors Governing the Na^+ vs K^+ Selectivity in Sodium Ion Channels". In: *Journal of the American Chemical Society* 132.7 (Jan. 2010), pp. 2321–2332. DOI: `10.1021/ja909280g`. URL: `https://doi.org/10.1021/ja909280g`.

[22]   L. Bocquet. "Nanofluidics coming of age". In: *Nature Materials* 19.3 (Feb. 2020), pp. 254–256. DOI: `10.1038/s41563-020-0625-8`. URL: `https://doi.org/10.1038/s41563-020-0625-8`.

[23]   W. Sparreboom, A. van den Berg, and J. C. T. Eijkel. "Principles and applications of nanofluidic transport". In: *Nature Nanotechnology* 4.11 (Nov. 2009), pp. 713–720. DOI: `10.1038/nnano.2009.332`. URL: `https://doi.org/10.1038/nnano.2009.332`.

[24]   L. Chen et al. "Millifluidics, microfluidics, and nanofluidics: manipulating fluids at varying length scales". In: *Materials Today Nano* 16 (Dec. 2021), p. 100136. DOI: `10.1016/j.mtnano.2021.100136`. URL: `https://doi.org/10.1016/j.mtnano.2021.100136`.

[25]   S. Succi, A. A. Mahammad, and J. Horbach. "Lattice-Boltzmann Simulations of Dense Nanoflows: a Comparison with Molecular Dynamics and Navier-Stokes Solutions". In: *International Journal of Modern Physics C* 18.04 (Apr. 2007), pp. 667–675. DOI: `10.1142/s0129183107010929`. URL: `https://doi.org/10.1142/s0129183107010929`.

[26]   J. A. Thomas and A. J. H. McGaughey. "Water Flow in Carbon Nanotubes: Transition to Subcontinuum Transport". In: *Physical Review Letters* 102.18 (May 2009). DOI: `10.1103/physrevlett.102.184502`. URL: `https://doi.org/10.1103/physrevlett.102.184502`.

[27]   T.-D. Li, J. Gao, R. Szoszkiewicz, U. Landman, and E. Riedo. "Structured and viscous water in subnanometer gaps". In: *Physical Review B* 75.11 (Mar. 2007). DOI: `10.1103/physrevb.75.115415`. URL: `https://doi.org/10.1103/physrevb.75.115415`.

[28]   L. Bocquet and E. Charlaix. "Nanofluidics, from bulk to interfaces". In: *Chem. Soc. Rev.* 39.3 (2010), pp. 1073–1095. DOI: `10.1039/b909366b`. URL: `https://doi.org/10.1039/b909366b`.

[29] M. M. Hatlo, D. Panja, and R. van Roij. "Translocation of DNA Molecules through Nanopores with Salt Gradients: The Role of Osmotic Flow". In: *Physical Review Letters* 107.6 (Aug. 2011). DOI: 10.1103/physrevlett.107.068101. URL: https://doi.org/10.1103/physrevlett.107.068101.

[30] D. Branton et al. "The potential and challenges of nanopore sequencing". In: *Nature Biotechnology* 26.10 (Oct. 2008), pp. 1146–1153. DOI: 10.1038/nbt.1495. URL: https://doi.org/10.1038/nbt.1495.

[31] Y. Zhang and G. C. Schatz. "Conical Nanopores for Efficient Ion Pumping and Desalination". In: *The Journal of Physical Chemistry Letters* 8.13 (June 2017), pp. 2842–2848. DOI: 10.1021/acs.jpclett.7b01137. URL: https://doi.org/10.1021/acs.jpclett.7b01137.

[32] X. Wang, C. Cheng, S. Wang, and S. Liu. "Electroosmotic pumps and their applications in microfluidic systems". In: *Microfluidics and Nanofluidics* 6.2 (Jan. 2009), pp. 145–162. DOI: 10.1007/s10404-008-0399-9. URL: https://doi.org/10.1007/s10404-008-0399-9.

[33] Z. Zhang, L. Wen, and L. Jiang. "Nanofluidics for osmotic energy conversion". In: *Nature Reviews Materials* 6.7 (Apr. 2021), pp. 622–639. DOI: 10.1038/s41578-021-00300-4. URL: https://doi.org/10.1038/s41578-021-00300-4.

[34] A. Siria, P. Poncharal, A.-L. Biance, R. Fulcrand, X. Blase, S. T. Purcell, and L. Bocquet. "Giant osmotic energy conversion measured in a single transmembrane boron nitride nanotube". In: *Nature* 494.7438 (Feb. 2013), pp. 455–458. DOI: 10.1038/nature11876. URL: https://doi.org/10.1038/nature11876.

[35] A. Siria, M.-L. Bocquet, and L. Bocquet. "New avenues for the large-scale harvesting of blue energy". In: *Nature Reviews Chemistry* 1.11 (Nov. 2017). DOI: 10.1038/s41570-017-0091. URL: https://doi.org/10.1038/s41570-017-0091.

[36] M. Elimelech and W. A. Phillip. "The Future of Seawater Desalination: Energy, Technology, and the Environment". In: *Science* 333.6043 (Aug. 2011), pp. 712–717. DOI: 10.1126/science.1200488. URL: https://doi.org/10.1126/science.1200488.

[37] B. Balannec, A. Ghoufi, and A. Szymczyk. "Nanofiltration performance of conical and hourglass nanopores". In: *Journal of Membrane Science* 552 (Apr. 2018), pp. 336–340. DOI: 10.1016/j.memsci.2018.02.026. URL: https://doi.org/10.1016/j.memsci.2018.02.026.

[38] M. L. Kovarik, K. Zhou, and S. C. Jacobson. "Effect of Conical Nanopore Diameter on Ion Current Rectification". In: *The Journal of Physical Chemistry B* 113.49 (Dec. 2009), pp. 15960–15966. DOI: 10.1021/jp9076189. URL: https://doi.org/10.1021/jp9076189.

[39] D. G. Haywood, A. Saha-Shah, L. A. Baker, and S. C. Jacobson. "Fundamental Studies of Nanofluidics: Nanopores, Nanochannels, and Nanopipets". In: *Analytical Chemistry* 87.1 (Dec. 2014), pp. 172–187. DOI: 10.1021/ac504180h. URL: https://doi.org/10.1021/ac504180h.

[40] L. Jubin, A. Poggioli, A. Siria, and L. Bocquet. "Dramatic pressure-sensitive ion conduction in conical nanopores". In: *Proceedings of the National Academy of Sciences* 115.16 (Apr. 2018), pp. 4063–4068. DOI: 10.1073/pnas.1721987115. URL: https://doi.org/10.1073/pnas.1721987115.

[41] W. Boon, T. Veenstra, M. Dijkstra, and R. van Roij. "Pressure-sensitive ion conduction in a conical channel: optimal pressure and geometry". In: (May 2022). DOI: 10.48550/ARXIV.2205.02002. URL: https://arxiv.org/abs/2205.02002.

[42] D. Wang, M. Kvetny, J. Liu, W. Brown, Y. Li, and G. Wang. "Transmembrane Potential across Single Conical Nanopores and Resulting Memristive and Memcapacitive Ion Transport". In: *Journal of the American Chemical Society* 134.8 (Feb. 2012), pp. 3651–3654. DOI: `10.1021/ja211142e`. URL: `https://doi.org/10.1021/ja211142e`.

[43] P. Ramirez, J. J. Perez-Grau, J. Cervera, S. Nasir, M. Ali, W. Ensinger, and S. Mafe. "Negative differential resistance and threshold-switching in conical nanopores with KF solutions". In: *Applied Physics Letters* 118.18 (May 2021), p. 181903. DOI: `10.1063/5.0051422`. URL: `https://doi.org/10.1063/5.0051422`.

[44] Y. Li, D. Wang, M. M. Kvetny, W. Brown, J. Liu, and G. Wang. "History-dependent ion transport through conical nanopipettes and the implications in energy conversion dynamics at nanoscale interfaces". In: *Chemical Science* 6.1 (2015), pp. 588–595. DOI: `10.1039/c4sc02195a`. URL: `https://doi.org/10.1039/c4sc02195a`.

[45] S. P. Adhikari, M. P. Sah, H. Kim, and L. O. Chua. "Three Fingerprints of Memristor". In: *Handbook of Memristor Networks*. Springer International Publishing, 2019, pp. 165–196. DOI: `10.1007/978-3-319-76375-0_5`. URL: `https://doi.org/10.1007/978-3-319-76375-0_5`.

[46] P. Robin et al. *Long-term memory and synapse-like dynamics of ionic carriers in two-dimensional nanofluidic channels*. 2022. DOI: `10.48550/ARXIV.2205.07653`. URL: `https://arxiv.org/abs/2205.07653`.

[47] D. Biolek, V. Biolkova, and Z. Biolek. "Pinched hysteretic loops of ideal memristors, memcapacitors and meminductors must be 'self-crossing'". In: *Electronics Letters* 47.25 (Dec. 2011), pp. 1385–1387. DOI: `10.1049/el.2011.2913`. URL: `https://doi.org/10.1049/el.2011.2913`.

[48] B. Sun, M. Xiao, G. Zhou, Z. Ren, Y. Zhou, and Y. Wu. "Non–zero-crossing current-voltage hysteresis behavior in memristive system". In: *Materials Today Advances* 6 (June 2020), p. 100056. DOI: `10.1016/j.mtadv.2020.100056`. URL: `https://doi.org/10.1016/j.mtadv.2020.100056`.

[49] V. S. Markin, A. G. Volkov, and L. Chua. "An analytical model of memristors in plants". In: *Plant Signaling & Behavior* 9.10 (Oct. 2014), e972887. DOI: `10.4161/15592316.2014.972887`. URL: `https://doi.org/10.4161/15592316.2014.972887`.

[50] S. Sarma, B. M. Mothudi, and M. S. Dhlamini. "Observed coexistence of memristive, memcapacitive and meminductive characteristics in polyvinyl alcohol/cadmium sulphide nanocomposites". In: *Journal of Materials Science: Materials in Electronics* 27.5 (Jan. 2016), pp. 4551–4558. DOI: `10.1007/s10854-016-4330-y`. URL: `https://doi.org/10.1007/s10854-016-4330-y`.

[51] P. C. Hiemenz and R. Rajagopalan. *Principles of colloid and surface chemistry*. New York: Marcel Dekker, 1997. ISBN: 0-8247-9397-8.

[52] R. van Roij. *Soft Condensed Matter Theory: 2020-2021*. Lecture Notes. Feb. 2021.

[53] H.-J. Butt, K. Graf, and M. Kappl. *Physics and chemistry of interfaces*. Weinheim: Wiley-VCH, 2003. ISBN: 3-527-40413-9.

[54] L. Onsager. "Reciprocal Relations in Irreversible Processes. I." In: *Phys. Rev.* 37 (4 Feb. 1931), pp. 405–426. DOI: `10.1103/PhysRev.37.405`. URL: `https://link.aps.org/doi/10.1103/PhysRev.37.405`.

[55] L. Onsager. "Reciprocal Relations in Irreversible Processes. II." In: *Phys. Rev.* 38 (12 Dec. 1931), pp. 2265–2279. DOI: `10.1103/PhysRev.38.2265`. URL: `https://link.aps.org/doi/10.1103/PhysRev.38.2265`.

[56] B. L. Werkhoven and R. van Roij. "Coupled water, charge and salt transport in heterogeneous nano-fluidic systems". In: *Soft Matter* 16.6 (2020), pp. 1527–1537. DOI: `10.1039/c9sm02144b`. URL: `https://doi.org/10.1039/c9sm02144b`.

[57] J. E. Hall. "Access resistance of a small circular pore." In: *Journal of General Physiology* 66.4 (Oct. 1975), pp. 531–532. DOI: `10.1085/jgp.66.4.531`. URL: `https://doi.org/10.1085/jgp.66.4.531`.

[58] *Conductivity standard solution, 146.9 μs/cm, KCL, 500 ml.* URL: `https://www.hach.com/conductivity-standard-solution-146-9-s-cm-kcl-500-ml/product?id=7640206167`.

A   Appendix: Current Cylinder

In Section 2.5 an expression for the fluid flux Q_{eo} through a cylinder of infinite length with radius R was derived, as a potential difference V is applied over it. We can also determine the electric current response I to a potential difference V applied over a cylindrical channel, where we only take into account the linear V-dependence of I. This electro-osmotic current I_{EO} has a conductive part and an advective part, as the potential difference induces a fluid flow through the channel. The conductive part is given by

$$
\begin{aligned}
I_{EO,con} &= \int_0^{2\pi} d\theta \int_0^R dr\, re\, (j_{+,x,con} - j_{-,x,con}) \\
&= 2\pi D \frac{e^2}{k_B T} E \int_0^R dr\, r\, (\rho_+(r,x) + \rho_-(r,x)) \\
&= 4\pi D \rho_0 \frac{e^2}{k_B T} E \int_0^R dr\, r\, \cosh\left[\phi(r)\right],
\end{aligned}
\tag{A.1}
$$

where we have taken the long channel limit, which gives that the electric field is given by $-\partial_x \psi = \frac{V}{l} = E$ and that the potential $\phi(r)$ does not depend on the lateral coordinate x. We also used the Boltzmann weight to determine the ion-densities $\rho_{\pm}$ and we extracted the conductive contribution to the ion flux $j_{+,x,con}$ from Eq. (2.42). The only place where the salt concentration is not equal to the bulk concentration, is in the EDL. We can therefore split the integral into a bulk term and surface term

$$
I_{EO,con} = 4\pi D \rho_0 \frac{e^2}{k_B T} E \left(\int_0^R dr\, r + \int_0^R dr\, r\, (\cosh\left[\phi(r)\right] - 1) \right).
\tag{A.2}
$$

We have found an approximation for the field in the channel in Eq. (2.38); hence, we can solve the integral of the surface term in Eq. (A.2) using coordinate $s = R - r$

$$
\begin{aligned}
\int_0^R dr\, r\, (\cosh\left[\phi(r)\right] - 1) &= \int_0^R ds\, (R - s)\, (\cosh\left[\phi(s)\right] - 1) \\
&\approx R \int_0^R ds\, (\cosh\left[\phi(s)\right] - 1),
\end{aligned}
\tag{A.3}
$$

where we have assumed that $\kappa^{-1} \ll R$. The potential $\phi(s)$ vanishes at large s, so the term $\cosh\left[\phi(s)\right] - 1$ vanishes as well. Because we assume that $\kappa^{-1} \ll R$, we can extend the upper integral limit from R to ∞, which allows us to introduce the integral

$$
\frac{1}{\lambda_D} \int_0^\infty ds\, (\cosh\left[\phi(s)\right] - 1) = 2\left(\cosh\left[\phi_0/2\right] - 1\right) \equiv P_2.
\tag{A.4}
$$

This expression can be used to determine the conductive current through the channel

$$
I_{EO,con} = 4\pi D \rho_0 R^2 \frac{e^2}{k_B T} E \left(\frac{1}{2} + \frac{\lambda_D}{R} P_2 \right).
\tag{A.5}
$$

To find the advective current $I_{EO,adv}$ induced by the potential difference over the channel, we use the fluid velocity of Eq. (2.52). The advective current is given by

$$
\begin{aligned}
I_{EO,adv} &= 2\pi \int_0^R dr\, r u_x(r)\, (\rho_+(r) - \rho_-(r))\, e \\
&\approx 2\pi E R e \rho_0\, \frac{\epsilon}{\eta} \int_0^R ds\, (\rho_+(s) - \rho_-(s))\, (\psi(s) - \psi_0),
\end{aligned}
\tag{A.6}
$$

where we have inserted Eq. (2.52) and again introduced coordinate $s = R - r$. Using conservation of charge given by

$$\sigma = -\int_0^R ds \ (\rho_+(s) - \rho_-(s)) = 2\rho_0 \int_0^R ds \ \sinh\left[\phi(r)\right], \tag{A.7}$$

we can solve this integral. We evaluate a part of Eq. (A.6), which results in

$$\frac{1}{2}e\int_0^R ds \ (\rho_+ - \rho_-)\,\psi = -\frac{1}{2}e\sigma\psi_0 - \frac{k_B T}{4\pi\lambda_B\lambda_D}P_2, \tag{A.8}$$

where we used P_2 from Eq. (A.4). The remainder of the integral can easily be evaluated to find

$$I_{EO,adv} = 2\pi R\rho_0 E\frac{\epsilon}{\eta}\left[-\frac{k_B T}{2\pi\lambda_B\lambda_D}P_2 + 0\right] = -R\rho_0 E\frac{\epsilon}{\eta}\frac{k_B T}{\lambda_B\lambda_D}P_2 = -4\pi R E\frac{e^2}{(4\pi\lambda_B)^2\lambda_D}. \tag{A.9}$$

The total linear electric current response resulting from an applied potential difference is therefore

$$I_{EO} = I_{EO,adv} + I_{EO,con}$$
$$= 2\rho_0 D\pi R^2 e^2 \left(-\partial_x\psi\right)\left(1 + \frac{2\lambda_D}{R}P_2\left(1 + \frac{1}{2\pi\lambda_B D\eta}\right)\right), \tag{A.10}$$

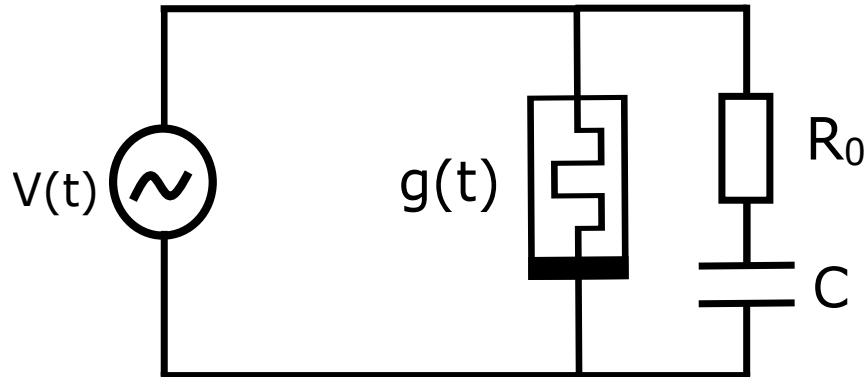where we have re-inserted the electric field $E = -\partial_x\psi$.

Figure 34: The circuit diagram of a memristor with memductance $g(t)$ with parasitic capacitance C under a periodic potential $V(t)$. The capacitor is in series with a resistor R_0.

B   Appendix: Capacitance Model

An equivalent circuit of a memristor with a capacitive element is given in Fig. 34. In this circuit, the capacitive element comes from a capacitor C and a resistor R_0 in series, attached parallel to the memristor with memductance $g(t)$. The derivation of the resulting current over the entire system follows the derivation as found in an article by Markin et al. [49], in which the same circuit is used. The potential difference of the AC-voltage source $V(t)$ is periodic with angular frequency $\omega = 2\pi f$. The current through the capacitor is given by

$$I_C(t) = C\frac{dV_C(t)}{dt}, \tag{B.1}$$

with C the capacitance and $V_C(t)$ the current over the capacitor. The resistor R_0 is an Ohmic resistor, so its current is given by

$$I_R = \frac{V_R}{R_0}, \tag{B.2}$$

with V_R the voltage over the resistor. From Fig. 34 we can deduce that the voltage over the memristor is the voltage of the source $V(t)$ and the voltage over the capacitor is $V_C(t) = V(t) - V_R$. The current through the capacitor is the same as the current through the resistor R_0, which means

$$\frac{V_R}{R_0} = C\frac{dV_C(t)}{dt}. \tag{B.3}$$

Combining these equations gives

$$C\frac{dV_C(t)}{dt} = \frac{V(t) - V_C(t)}{R_0}, \tag{B.4}$$

and when we introduce the RC-time parameter

$$\xi = R_0 C, \tag{B.5}$$

this equation becomes

$$\frac{dV_C(t)}{dt} + \frac{1}{\xi}V_C(t) = \frac{1}{\xi}V(t). \tag{B.6}$$

The solution of this differential equation is

$$V_C(t) = e^{-\frac{t}{\xi}} \left(\frac{1}{\xi} \int_0^t V(k) e^{\frac{k}{\xi}} dk + B \right), \tag{B.7}$$

with B a constant that can be determined using the boundary conditions. If we take the periodic potential difference to be

$$V(t) = V_0 \sin(\omega t), \tag{B.8}$$

we can further specify the solution. In the steady state solution, V_C must be constant, so $V_C(t) = V_C(t + T)$ for every time T. Taking $t = 0$ results in the following equation

$$e^{-\frac{0}{\xi}} \left(\frac{1}{\xi} \int_0^0 V(k) e^{\frac{k}{\xi}} dk + B \right) = e^{-\frac{T}{\xi}} \left(\frac{1}{\xi} \int_0^T V(k) e^{\frac{k}{\xi}} dk + B \right)$$

$$B = e^{-\frac{T}{\xi}} \left(\frac{1}{\xi} \int_0^T V(k) e^{\frac{k}{\xi}} dk + B \right), \tag{B.9}$$

which in turn gives

$$B = \frac{\frac{1}{\xi} \int_0^T V(k) e^{\frac{k}{\xi}} dk}{e^{\frac{T}{\xi}} - 1} = -\frac{\xi \omega V_0}{1 + (\xi \omega)^2}, \tag{B.10}$$

where we again inserted $V(k) = V_0 \sin(\omega k)$. We were able to solve this integral by integrating by parts twice. Now that we have this constant of integration, we can find the voltage over the capacitor

$$V_C(t) = e^{-\frac{t}{\xi}} \left(\frac{1}{\xi} \int_0^t V(k) e^{\frac{k}{\xi}} dk - \frac{\xi \omega V_0}{1 + (\xi \omega)^2} \right)$$

$$= V_0 \frac{\sin(\omega t) - \xi \omega \cos(\omega t)}{1 + (\xi \omega)^2}.$$

Taking its derivative gives us the current that runs through the capacitor

$$I_C(t) = C \frac{dV_C(t)}{dt} = C V_0 \omega \frac{\cos(\omega t) + \xi \omega \sin(\omega t)}{1 + (\xi \omega)^2}. \tag{B.11}$$

The total current through the device, composed of the memristor and the capacitor, is therefore given by

$$I(t) = I_M(t) + I_C(t) = V(t) g(t) + C V_0 \omega \frac{\cos(\omega t) + \xi \omega \sin(\omega t)}{1 + (\xi \omega)^2}, \tag{B.12}$$

where $g(t)$ is the memductance of the memristor. In the case that the RC-time is much smaller than the period of the potential, so if $\xi \omega \ll 1$, we find that the current reduces to

$$I(t) \approx V(t) G(t) + C V_0 \omega \cos(\omega t). \tag{B.13}$$

This is the current as described by the circuit in Fig. 4.
The RC-times of the systems considered in this thesis are generally a lot smaller than the frequencies at which we drive these systems and smaller than the characteristic timescale τ of these systems. To give an illustration, in Eq. (4.37) we found that the timescale τ is of the order of 10^{-6} s, whereas we found in Eq. (5.8) that the RC-time of these systems is of the order 10^{-8} s. We are justified in using the circuit as given in Fig. 4 in studying nanopore systems, as for these systems $\xi \omega \ll 1$.

C   Appendix: COMSOL Meshes

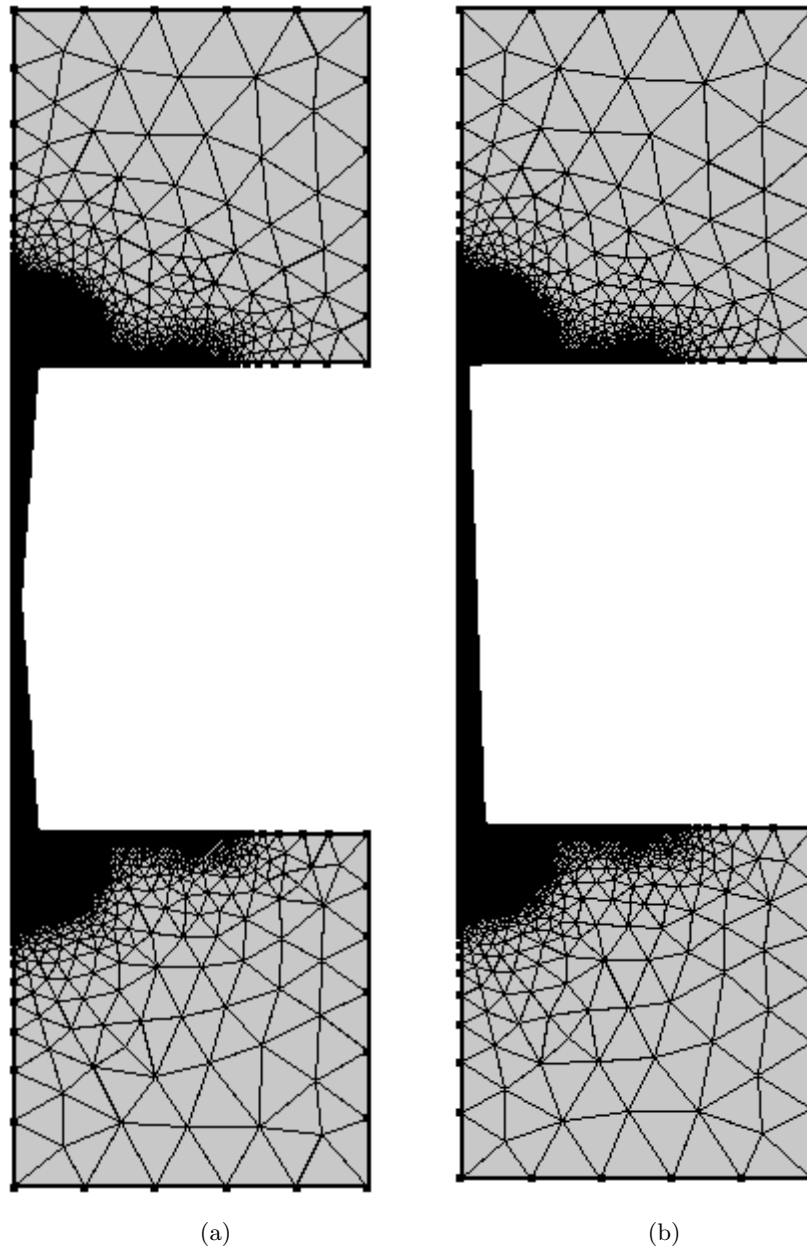<div align="center">(a)   (b)</div>

Figure 35: Mesh of finite-element calculation cells in COMSOL MULTIPHYSICS for nanopore geometries with (a) $\delta = 0.0$ and (b) $\delta = 0.99$.

D   Appendix: Extra Crossings Finite-Element Calculations

In Section 5 a set of state diagrams was shown indicating the memristor type for a range of dimensionless frequencies $\omega\tau$ and geometry ratios δ, for example in Fig. 28. The memristive behaviour results from finite-element calculations were indicated with indivudual dots. Some of these dots were crossed, to indicate that the number of crossings in these hysteresis loops was larger than the number of crossings associated with their memristive behaviour classification. In Fig. 36 the same state diagram is shown, but it indicates the number of crossings a hysteresis loop possesses for a set of parameters δ and $\omega\tau$, instead of its the hysteresis type.
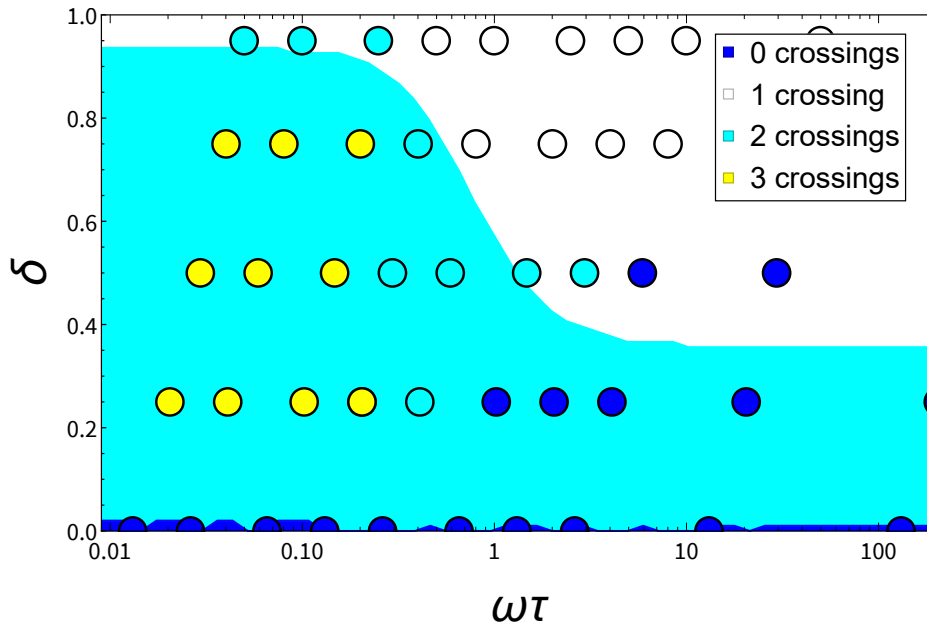

Figure 36: Diagram of the number of hysteresis loop crossings for various geometries, given by δ, and various dimensionless frequencies $\omega\tau$. Results from finite-element calculations, as indicated by the coloured dots, are compared to results from the analytic model, indicated by the hues in the background. The analytic model possesses no capacitive element, so $\frac{C}{G_0\tau} = 0$.

In Fig. 36 we observe that for low frequencies the total number of crossings is larger in the finite-element results than in the analytic results. The hysteresis loops from the FE-calculations possess an extra crossing that the analytic loops do not possess, for almost all geometries for dimensionless frequencies lower than approximately $\omega\tau = 0.3$. This includes hysteresis loops with three crossings, which the analytic model does not predict for any combination of parameters.
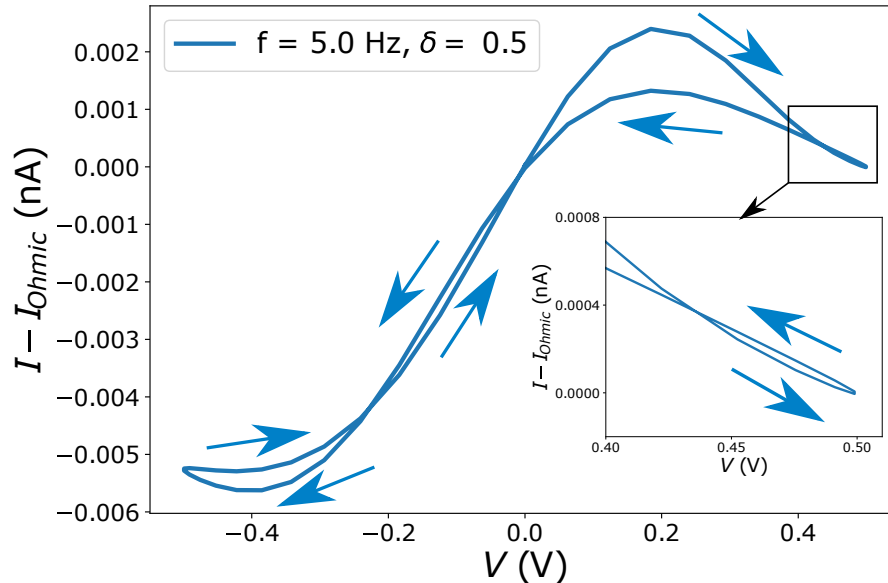
Figure 37: Current-voltage diagram with the hysteresis loop of a channel with $\delta = 0.5$ from finite-element calculations. A periodic voltage $V = V_0 \sin[2\pi f t]$ is applied over the channel, with $V_0 = 0.5$ V and $f = 5.0$ Hz. Attention is given to a crossing at large positive voltage, which is shown in the inset figure.

In Fig. 37 attention is given to this extra crossing, which occurs at large values of V and is not reproduced in the analytic model. It is however quite minor: the general behaviour of a type-c memristor, as plotted in Fig. 37, or of a type-I memristor remains intact.

It is not clear how this extra crossing originates, but since this extra crossing only appears for positive potential differences, it is probable that it is caused by some odd-powered voltage dependence in the conductivity of the channel. Because it only turns up at low frequencies, it is likely that this extra crossing is the result of a process that has a large timescale. This process is not described by the differential equation in Eq. (4.27), which only contains a single timescale τ, because we would have otherwise encountered hysteresis loops with three crossings in our analytic calculations. The model fails in taking into account the process that causes these extra crossings.

In most reporting in this thesis we ignore this extra crossing in determining memristive behaviour, as it seems to originate from some minor effect that is yet unknown. However, we acknowledge its presence by adding a cross through the finite-element data points that possess this extra crossing.